uOttawa

L'Université canadienne
Canada's university

FACULTÉ DES ÉTUDES SUPÉRIEURES ET POSTOCTORALES

uOttawa

L'Université canadienne
Canada's university

FACULTY OF GRADUATE AND POSDOCTORAL STUDIES

David Roy-Guay
AUTEUR DE LA THÈSE / AUTHOR OF THESIS

M.Sc. (Physics)
GRADE / DEGREE

Department of Physics
FACULTÉ, ÉCOLE, DÉPARTEMENT / FACULTY, SCHOOL, DEPARTMENT

Developing Quantum Dot Broadband Materials for Telecommunication and Other Applications

TITRE DE LA THÈSE / TITLE OF THESIS

Sylvain Raymond
DIRECTEUR (DIRECTRICE) DE LA THÈSE / THESIS SUPERVISOR

CO-DIRECTEUR (CO-DIRECTRICE) DE LA THÈSE / THESIS CO-SUPERVISOR

Xiaoyi Bao

Karin Hinzer

Tong Xu

Gary W. Slater
Le Doyen de la Faculté des études supérieures et postdoctorales / Dean of the Faculty of Graduate and Postdoctoral Studies

Developing quantum dot broadband materials for telecommunications and other applications

by

David Roy-Guay

Thesis submitted to the
Faculty of Graduate and Postdoctoral Studies
In partial fulfillment of the requirements
For the M.Sc. degree in
Physics

Department of Physics
Faculty of Science
University of Ottawa

Your file Votre référence
ISBN: 978-0-494-65963-2
Our file Notre référence
ISBN: 978-0-494-65963-2

Abstract

Recently, InAs/InP quantum dot lasers operating in the telecommunications wavelength range showed promising properties such as low threshold, high external efficiency, high bandwidth, multiwavelength emission and passive mode-locking. The photoluminescence of quantum dot layers is investigated, in the scope of improving InAs/InP quantum dot lasers performance operating in the telecommunications range. Stacking of layers with GaP underlayer reduces the full width at half maximum of the emission, improving the laser performances to a competitive alternative to quantum well lasers. Polarization photoluminescence of sample edge emission is investigated to aim for the development of a polarization insensitive semiconductor optical amplifier operating at 1.55 μm. Polarization properties are studied for a stack period between 5 and 30 nm and for single quantum dot layers rapid thermal annealed from 600 to 700°C. Decreasing the period lowers the degree of polarization of side emission from 80 to 40%, suggesting modification of polarization properties by coupling between the layers.

Acknowledgements

Premièrement j'aimerais remercier mes parents qui m'ont partagé leur émerveillement en science et d'en avoir fait ma réalité ;). Merci pour votre intérêt en ma recherche et vos encouragements tout au long de ma maîtrise!!

Thanks to Peter, Tony, Martin, Uncle Mike, Coffee Mate and all the people who joined us in the dungeon of CPFC to have fun over lunch!

Particular thanks to Serge Desgreniers and Hélène Lacasse for giving me precious teaching experiences!

Merci à la comptable pour avoir dormi sur ma présentation.

Thanks to Philip, Zhenghuo and Soufien for sharing your knowledge!

Et finalement, merci à Sylvain, pour tout le temps à m'expliquer les concepts fondamentaux, l'autonomie que tu m'as toujours laissée et surtout l'enthousiasme et l'intérêt constant que tu laissais paraître! Tu m'as certainement amené plus proche du grade de lieutenant!

Contents

List of Tables

List of Figures

List of Abbreviations

BA	Broad Area
CW	Constant Width
DOP	Degree of Polarization
DOS	Density of States
EL	Electroluminescence
FP	Fabry-Perot
GS	Ground State
HH	Heavy Hole
I_{th}	Threshold Current
IB	Inhomogeneous Broadening
J_{th}	Threshold Current Density
LH	Light Hole
LIV	Power Current Voltage
LN_2	Liquid Nitrogen
MLL	Mode Locked Laser
MWL	Multiwavelength Laser
OCT	Optical Coherence Tomography
PL	Photoluminescence
$Pol-PL$	Polarization Photoluminescence
QD	Quantum Dot

$QDash$	Quantum Dash
QW	Quantum Well
QWR	Quantum Wire
SA	Self-Assembled
SH	Semiconductor Heterostructure
SK	Stranski-Krastanow
SLD	Superluminescent Diode
T_0	Characteristic Temperature
VB	Valence Band
WL	Wetting Layer

Chapter 1

Introduction

1.1 Reduced dimensionality structures

Since the enhancement of semiconductor purity which lead to the development of the first transistor based on Germanium by Shockley at Bell Labs in 1949 [1], solid state physics grew to become the biggest physics domain. Semiconductors proved interesting as their bandgap is small compared to insulators, so that carriers are easily promoted from the valence band (VB) to a higher energy band, the conduction band (CB). By applying a voltage on these materials, one can switch on and off the carrier current, in a p-n junction, made by controlled doping of semiconductors. In 1952, the p-n junction was then processed to convert light into current in a solar cell [2] and to transport current through thin layers, with the development of tunneling diodes (1958) [3]. Current to light conversion devices in the infrared was achieved with the first solid state laser using a doped GaAs junction in 1962 [4]. Further gap width and alignment engineering was achieved in semiconductor heterostructures (SH), which used different semiconductors in a single device to widen the spectrum of energies available for device operation. Surprisingly, light emitting diodes (LEDs), which are currently revolutionizing lighting, were invented way before in 1907 by H.J. Round with silicon carbide [5]. Later, intensive research was done to reduce the size of semiconductor devices and their power consumption. As dimensions of these devices shrank, new properties arose, quantum effects, which can be used in order to enhance device performances, for instance in quantum well lasers in 1975 [6]. As a better understanding of dimensionality confinement effects on the electron wavefunction was achieved, interest in lower dimensionality devices such as quantum wires (QWR)

and quantum dots (QD) structures grew at the end of the 20th century and led to the decrease in threshold injection current of heterostructure laser devices. Here the QDs are used as tiny emitting devices for higher performance telecommunications lasers.

Band properties of semiconductors have been extensively studied theoretically to fuel these developments. Beginning with Bloch's theorem (1928) and Brillouin's zone description for a periodic structure, the tight binding model described the origin of energy bandgap in crystal semiconductors. For the first time, it was shown that periodicity in a bulk substance restrains allowed electrons momentum quantity, resulting into the quantization of electron's energy. Luttinger and Kohn [7] then developed $k \cdot p$ theory as a perturbative approach to solve Bloch's wavefunction for wavevector $k \simeq 0$, leading to the parabolic band approximation and the introduction of an effective mass for electrons and holes. It was also shown that the Bloch functions for the conduction band acts as a s-like atomic orbital (l=0) and the valence band as a p-like atomic orbital (l=1). This greatly simplified bandgap structure calculations, as electron's interactions are grouped into a single parameter. In 1980, quantum mechanical spin property was included by Kane [8] into $k \cdot p$ calculations, which showed that the valence band is in fact separated by spin-orbit coupling in three bands, the heavy hole (HH), light hole (LH) and split-off band (SO).

Further control of carriers was achieved by their confinement in low dimensionality structures, from bulk to QWs, QWRs and QDs. Notice the redundancy in the use of the 'quantum' word: when a material's dimension is reduced to the order of de Broglie's wavelength, boundary conditions applied to the electron's wavefunction cause discretization of energy levels. Due to their 3D confinement (see section 2.1), QDs have atomic-like completely discrete energy levels instead of the continuum offered by bulk substances. QDs are often referred to as 'artificial atoms' because of that fundamental property [12]. The bottomline is that the properties of a single atom can be reproduced by the use of structures containing a few thousands semiconducting atoms, instead of the challenging isolation of a single atom. As growth techniques improved over the last two decades, QDs generated a lot of interest, offering great tunability by the variation of their size, strain and composition distribution. These nanostructures can now be grown in a multitude of ways, namely self assembled quantum dots (used in this thesis), dots in a wire [13], dots in a two dimensional gas (2DEG) [10] and more recently, colloidal QDs [11].

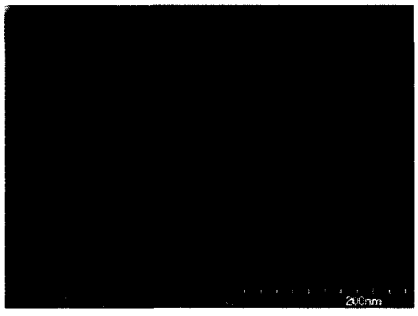

(a) InAs/InP self assembled QDs

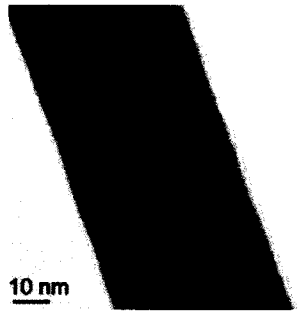

(b) InAs/InP dots in a nanowire [9]. Copyright 2008 by the American Physical Society

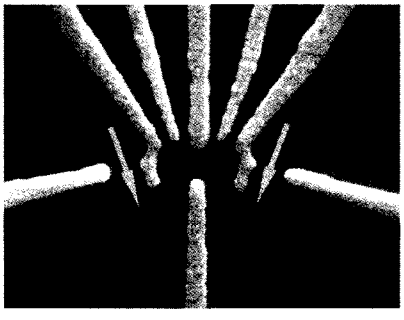

(c) Two dimensional gas (2DEG) forming a double dot structure [10]. Reproduced by permission of IOP Publishing

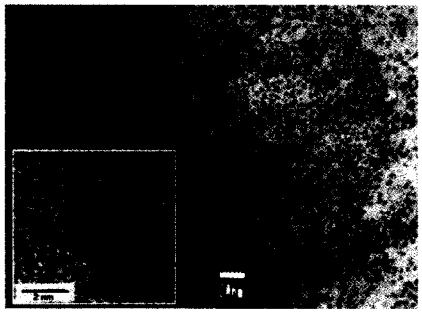

(d) Colloidal CdSe QD [11]. Reproduced by permission of The Royal Society of Chemistry

Figure 1.1: Different kinds of QD structures

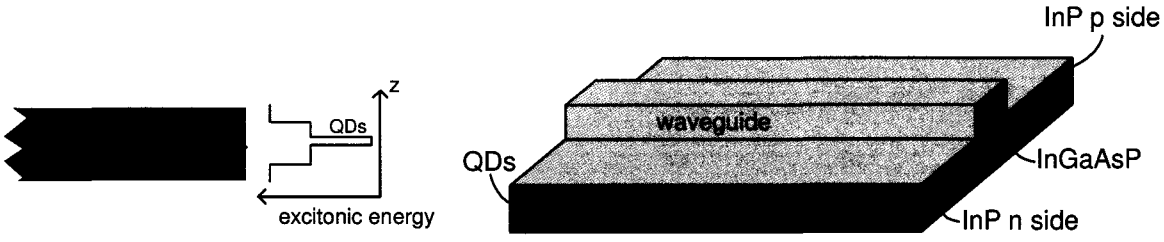

Figure 1.2: Fabry-Perot laser structure and band structure. Left: Band structure of emitting core. Right: Common Fabry-Perot laser with electrical injection from a p-n junction.

Fueled by the theoretical predictions of enhanced performances compared to other confined devices [14, 15], a large number of QD devices were developed. Lasers for telecommunications, optical coherence tomography (OCT), high efficiency solar cells, semiconductor amplifiers and quantum bits (qubits) for quantum computers are only a few examples of QD devices. In the last few years, organic colloidal QDs made of CdSe have gathered huge interest as they are easily grown in a solution and then spin coated on a substrate, providing a way to produce cheap solar cells without conventional nanofabrication. However, light conversion efficiency of such devices remains lower than 5% and the underlying performance limiting processes, such as surface states, remain under investigation [16, 17].

Lasing device

Semiconductor lasers are of great interest due to their compact nature and electrical pumping scheme. In order to get positive optical gain and thus lasing effect, light emitted in a semiconducting device has to be confined in a structure where population inversion can occur. This can be achieved in a Fabry-Perot (FP) cavity, where two vertical mirrors placed at the ends of a gain material provide longitudinal confinement. Light is confined in the transverse direction by the difference of index of refraction at the waveguiding core / p-n junction interface and lateral confinement by the ridge / air interface (see figure 1.2). Light production comes from the injection of electrons into the waveguiding core by the p-n junction. The electrons in the active region then lose energy by phonon emission, until they fall into the conduction band (CB) of the confined structure. Recombination of electrons with holes in the valence band (VB) then leads to photon emission. The

photon is then trapped in between two mirrors reflecting most of the light back into the cavity, stimulating coherent photon emission from other dots with the same energy levels, leading ultimately to the laser effect. Semiconducting Fabry-Perot lasing devices are very convenient, as they are low power and very compact. Traditional p-n junction laser emission is limited by the material intrinsic bandgap, but QDs, as shown below, offer a lot of advantages over bulk p-n junction lasers, including bandgap, or emission tunability.

Why QDs?

Most of today's telecommunications lasers are based on QW active layers, which lower threshold and improve efficiency of devices compared to bulk lasers. In such lasers, discretization of energy levels in a QD results in great advantages over other confined structures [18] :

- Lower lasing current density J_{th}, as population inversion is easier to achieve [14].
- Higher characteristic temperature T_0, translating into a lower laser temperature dependence operation, because the thermal energy k_BT is lower than the energy level separation, so electrons can't populate a higher energy level [15].
- In the case of QD ensembles, enhanced tunability of the emission wavelength and broader emission [19].
- Higher external efficiency η_d and lower internal losses α_i [20].
- Independent emitters : carrier dynamics in a QD don't affect the carriers of neighboring QDs, contrarily to QWs.

These 'theoretical' advantages are hindered by the inhomogeneous broadening (IB) of the physical QDs. Growth of such structures took more than a decade, but now growth of III-V self-assembled (SA) QDs is well controlled. Self-assembly of InAs islands, interesting because of its large lattice mismatch with GaAs and InP, can be achieved by the Stranski-Krastanow (SK) growth. This strain driven growth method (see section 2.2) leads to high QD densities ($> 10^{11}$ dots/cm^2) of roughly 30 nm diameter and 4 nm height lens shaped QDs. That lens shape structure at the nanometer scale provides zero dimensional (0D) confinement of electrons, but doesn't reproduce the properties of

an ideal QD formed by the superposition of three independent QWs. Due to the QD lens shape, confinement in the plane of the dot is weaker than in the growth direction ($\hat{z}$), so it can be approximated by an in-plane two dimensional harmonic oscillator and a quantum well in the vertical direction [21], as confirmed by magnetic photoluminescence (PL) measurements [22]. Depending on the substrate used for QD growth, emission can be tailored in various wavelength ranges, opening the door to a multitude of applications. For instance, InAs SA QDs on GaAs substrate emit around 1 μm and the 1.5 μm telecommunications range can be achieved with an InP substrate. However, the statistical growth nature of SA QDs leads to distribution in size, composition and strain. This phenomenon, the IB of the emission, results in a broad collective DOS, which has to be taken into account when discussing advantages of QDs over QW. Despite the broadening, actual devices with InAs QDs on GaAs have shown infinite T_0 [23] and very low threshold current ($< 17A/\text{cm}^2$) [24].

In order to better understand the electronic shell structure of QDs, isolation of a single quantum dot for spectroscopic studies was required, as the emission from an ensemble of dots hides the individual QD behavior [25]. Ultimately, the ability to grow a single QD intentionally was achieved on a pyramid and deposition of gates allowed electrical injection and control over the band alignment by applying electric fields [26, 27]. Magnetic PL studies were also carried on single SA QD to gain more insight on dot energy structure, revealing the effect of spin-orbit coupling for example[28].

InAs/InP QDs : the telecommunications goal

With the growing demand for bandwidth in telecommunications, high performance lasers with lower threshold current, better efficiency and higher bandwidth emitting in the C and L bands extending from 1530 nm to 1625 nm are needed. The C-band, or conventional band, corresponds to the minimum signal absorption band in erbium doped fibers used for long distance data transmission in telecommunications. Development of strain engineered InAs dots grown on GaAs achieved this goal, but PL signal remained weak due to non-radiative recombinations induced by a bigger number of defects [29]. SA InAs QDs grown on InP emitting in the 1.5 μm range were first successfully grown by Fafard et al. [30]. Growth conditions were only recently mastered, due to the lower lattice mismatch of InAs on InP substrate, which causes the growth of bigger, thinner, inhomo-

geneously broadened QDs. Furthermore, InP growth chambers are much less common than conventional GaAs molecular beam epitaxy (MBE) chambers. Finally, a number of telecommunications devices using QDs were grown, now including semiconductor optical amplifiers (SOAs) [31], multiwavelength lasers (MWL) [32], mode locked lasers (MLL) [33, 34], very low threshold QD lasers [35]. Future applications include entangled and single photon sources, the basic pieces required for quantum computation [36, 37].

Advanced applications

As mentioned before, IB can be problematic for low threshold current lasers as the gain is spread over a larger wavelength range. On the other hand, larger IB can be desirable for MWL and MLL. As a cleaved FP laser emits laser modes separated by $\Delta\lambda = \lambda^2/2nL \sim 0.25$ nm, a stack of QD layers with an emitting bandwidth up to tens of nanometers allows production of a lot of modes in the lasing peak, n being the index of refraction and L the length of the device. That way, emission of up to 90 laser channels from a single device in a 13 nm 3 dB bandwidth of emission in the L and C bands was made possible [38]. Such high number of channels is remarkable for wavelength domain multiplexing (WDM) and remote sensing, as an array of QW lasers can be replaced by a single QD laser diode. What is even more surprising is that achieving MLL with the same device is fairly straightforward. Adding a high reflectivity coating on a facet of the laser diode provides high enough photon density to correct the intrinsic linear dispersion present in the waveguide, resulting in uniform mode spacing. At that point, nonlinear processes such as four wave mixing and phase locking can occur. C and L band 400 fs pulses were demonstrated, which are the shortest pulses from a semiconductor MLL in these wavelength range [33, 32].

1.2 Thesis outline

Up until now, polarization control over the emission of a quantum dot layer has yet to be achieved. This step is necessary if one is to use QDs into SOAs and other polarization sensitive devices. Moreover, another problem in the laser devices is strain propagation in the stack of active layers, which causes a worsening of the IB, limiting the device gain and hence its performances. Both of these shortfalls will be addressed in this thesis by the spectroscopic study of QD stacks. In the next chapter, the theoretical framework of

the PL is presented to get an insight on the polarization properties of a stack of QDs. In chapter 3, play over the stack period and intermixing will be investigated as a way to achieve polarization independence. Insertion of a GaP strain compensating underlayer will also allow the reduction of IB in the PL, closing the performance gap between the QW and QD laser devices as shown in the second half of chapter 3. Note that even after the GaP addition, the QD ensemble spectral bandwidth is wide enough for MWL and MLL applications. Finally in chapter 4 we take advantage of the IB instead of fighting it to make superluminescent diodes (SLDs), for application in optical coherence tomography (OCT).

Chapter 2

Theory

In this chapter, we begin by deriving the density of states for QDs to show that energy levels are indeed quantized. In section 2.2 the physical realization of the 3D confinement is investigated by the presentation of various growth methods. The dimensions of the dot will reflect in the calculation of the band structure and energy levels (section 2.3). As the luminescence properties of QDs are investigated in this thesis, the optical selection rules are derived in section 2.4 and finally, following treatment by Bastard, the envelope function approximation is used to gain insight on the optical polarization properties of the QDs.

2.1 Quantum dot (QD) density of states

As mentioned before in chapter 1, QDs behave very much like atoms, as they have discrete energy levels. This is counterintuitive compared to most macroscopic quantities, like momentum and energy, which are continuous. Here we prove from Schrdinger's equation the discretization of energy levels in a confined structure.

The discretization of QD levels is a fundamental property resulting from the reduction of dimensionality. Mathematically, it is described by the density of states (DOS), the number of electron states available per unit energy. Let us consider a single electron in a bulk material. As we reduce material's dimensions to the order of Broglie's wavelength, confinement of the electron wavefunction into the low dimensional material imposes boundary conditions to Schrdinger's equation, leading ultimately to the discrete-

ness of energy levels for the 0D case. The wavefunction of an electron in a quantum dot has to satisfy Schrdinger's equation and the boundary condition :

$$-\frac{\hbar^2}{2m^*}\nabla^2\Psi + V\Psi = E\Psi \tag{2.1}$$

$$\Psi(x_i = 0) = \Psi(x_i = L_i) = 0 \tag{2.2}$$

where Ψ is the electron's wavefunction, $x_i = x, y, z$, V refers to the potential created by a 1D well and L_i is the width of the well. That way, the QD is viewed as the superposition of three independent infinite quantum wells in x, y, z. As done with traditional approaches to solve the problem of an infinite potential well, we pose the solution $\Psi_i = e^{ik_i x_i}$ with $k_i = 2\pi n_i/L$ to satisfy boundary condition. Inserting Ψ into 2.1 we find the following eigenenergies :

$$E = \frac{\hbar^2}{2m^*}(k_x^2 + k_y^2 + k_z^2) \tag{2.3}$$

or

$$E = \frac{4\pi^2\hbar^2}{2m^* \prod_i L_i^2}(n_x^2 + n_y^2 + n_z^2) \tag{2.4}$$

Equation 2.4 shows clearly that if L_i gets small (on the order of Broglie's wavelength) a change in index n_i implies a finite energy step, thereby creating discrete energy levels. These equations describe a perfect 0D box, but real quantum dots grown by self assembly are lens (or disk) shaped and have finite barriers. In section 2.3 we will show that QD's microscopic z direction acts like a quantum well and the x-y electron confinement plane (roughly 10 times z dimension) contributes as a 2D harmonic oscillator on energy.

In equation 2.3, since the wavevector k is no longer continuous, but quantified in 1, 2 or 3 directions, the DOS available for electrons in the k-space is different for bulk, QW, QWR and QD. DOS is then obtained by $\rho(E) = \frac{dN(E)}{dE}$, so the number of states N(E) for each structure needs to be computed. Number of states is derived from the ratio of the space occupied by all states on the space occupied by a single state. For more details, refer to Arakawa et al. [15] and Bimberg [39]. Allowed states and their associated k-space values for different dimensionalities are represented in figure 2.1. The allowed k vectors are contained within a k-sphere for a bulk substance, on planes for QW, on lines within the planes for QWR and represented by dots for a QD, so for the latter k values are completely discrete. This reduction of the allowed energy values for

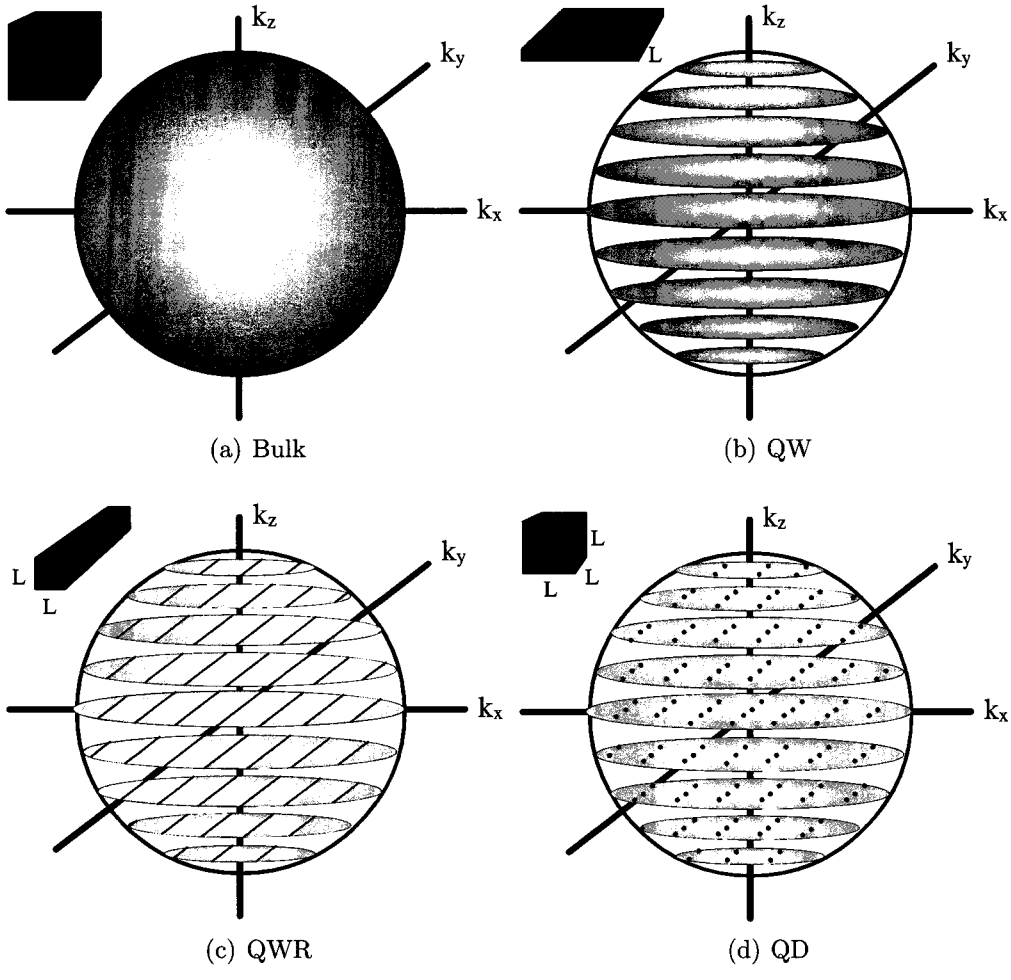

Figure 2.1: Allowed K space values for various dimensionalities

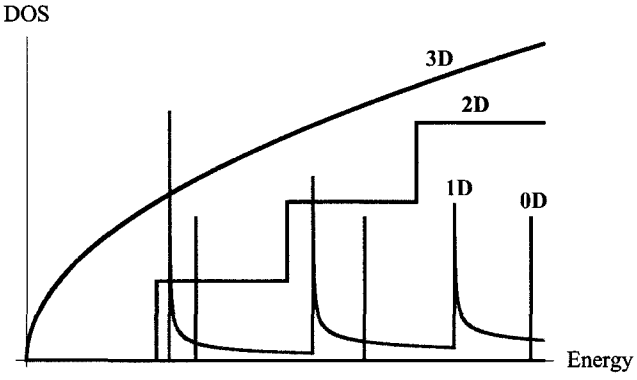

Figure 2.2: DOS dependence on dimensionality

wavevectors with dimensionality explains the discretization of energy levels.

	E	$\rho(E)$
3D	$\frac{\hbar^2}{2m^*}\left(k_x^2+k_y^2+k_z^2\right)$	$\frac{L^3 m^*}{\pi^2\hbar^3}(2m^*E)^{1/2}$
2D	$\frac{\hbar^2\pi^2 n_z^2}{2m^*L^2}+\frac{\hbar^2}{2m^*}(k_x^2+k_y^2)$	$\frac{L^2 m^*}{\pi\hbar^2}\sum_{nz}\Theta(E-E_{nz})$
1D	$\frac{\hbar^2\pi^2}{2m^*L^2}(n_z^2+n_y^2)+\frac{\hbar^2}{2m^*}(k_x^2)$	$\frac{L}{\pi}(\frac{2m^*}{\hbar^2})^{1/2}\sum_{nz,ny}(E-E_{nz,ny})^{-1/2}\Theta(E-E_{nz,ny})$
0D	$\frac{\hbar^2\pi^2}{2m^*L^2}(n_z^2+n_y^2+n_x^2)$	$2\delta(E-E_{nz,ny,nx})$

Table 2.1: Allowed energies and density of states $\rho(E)$ for 3D, 2D, 1D and 0D structures

Table 2.1 summarizes allowed energies and the DOS for all dimensionalities. Figure 2.2 is the graphical representation of table 2.1 and shows that DOS in function of energy for a bulk is parabolic, then changes to a step function for a QW, to a parabolic decrease for QWR and finally to a Dirac delta DOS for QDs. The Dirac delta DOS of QDs means that energy levels are quantized. The discreteness of energy levels is why QD lasers are expected to show better performances than traditional QW or bulk lasers, as mentioned in chapter 1.

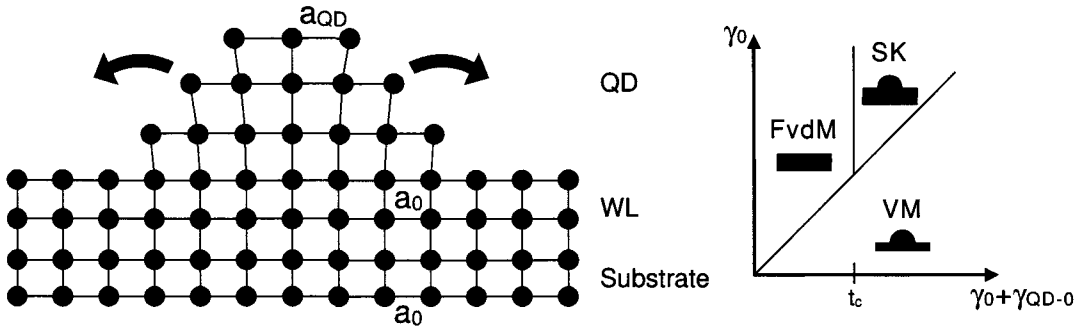

Figure 2.3: Left : Stranski Krastanow growth method. a_0 and a_{QD} stand for the lattice parameter of the substrate and QD substance respectively. QD forms due to strain energy relaxation caused by the lattice mismatch. Right : Self-assembly growth modes for substrate free energy in function of interfacial plus dot material free energy. At a critical wetting layer thickness t_c, the growth switches from FdvM to SK [40].

2.2 Growth of QDs

We demonstrated how discrete energy levels appear in 0D structures, but we now need to create such structures physically. A well known method is self-assembled (SA) growth of quantum dots, a strain driven process used for the growth of this thesis samples. By choosing a dot material and a substrate material with different lattice parameters (a_{QD}, a_0), a strain energy (μ) is associated to the materials lattice mismatch ($\epsilon = \frac{a_{QD}-a_0}{a_0}$). Materials also have their respective surface free energy (γ_{QD}, γ_0) and interfacial surface energy (γ_{QD0}) between the dot material and the substrate, which has to be considered in the QD growth kinetics. The principle is simple : QDs begin to self assemble to minimize the sum of these energies. The growth process can take multiple forms; if the substrate free energy is higher than the sum of the interfacial energy and dot material free energy ($\gamma_0 > \gamma_{QD0} + \gamma_{QD} + \mu$), a thin film will grow on the substrate in order to minimize total energy (Frank-van der Merwe (FvdM) growth). On the contrary, if it is lower than the sum, 3D islands form immediately on the substrate (Volmer-Weber (VW) growth). Lastly, growth can switch from thin film to island growth due to accumulated strain energy in the formed wetting layer, at a critical thin film thickness t_c. In the latter case, relief of the strain is favorable over gain of QD surface free energy γ_{QD}; such growth mode is referred to as Stranski-Krastanow (SK) (see figure 2.3) [40].

Selection of materials for growth is critical, as if the strain energy is too high, disloca-

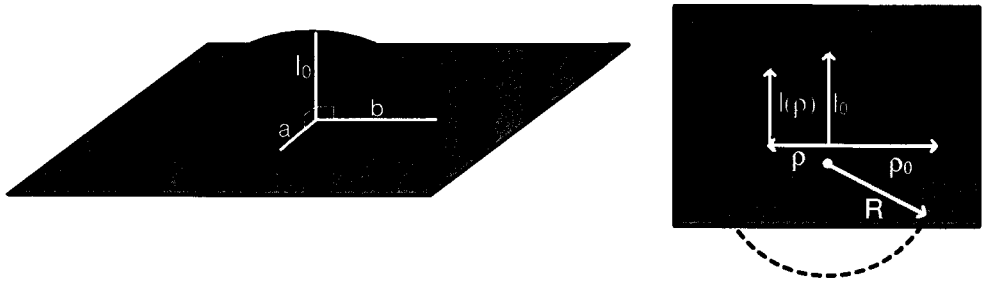

Figure 2.4: Left : Lens dot dimensions, a is the minor radius and b is the major radius of the dot. Right : View from side of dot, l_0 is the height of the dot, $l(\rho)$ is the height in function of the position on the base

tions and defects into the dot structure will form to lower strain energy and thus provide non-radiative centers, resulting in PL intensity quenching. Materials used in this work are InAs as the dot material and GaAs, InGaAsP or InP as barrier. The lattice mismatch is 7.2, 3.2 and 3.2% respectively, as the InGaAsP used is lattice matched to InP. According to the above considerations, InAs dots on GaAs will form faster and higher than on InP or InGaAsP, as their strain energy term is bigger. Furthermore, InAs/GaAs (InAs/InP) are fundamentally different as the exchange material is the group V material As (group III material In). These materials share the Zinc Blende crystal structure, but InAs/InP dots have a larger VB offset than InAs/GaAs dots, which results in a smaller confinement for electrons and stronger confinement for holes wavefunctions, as will be shown in section 2.3 [41]. Growth of SA QDs results in lens shaped structures with a diameter roughly 10 times the height, so the confinement potential in the z direction is stronger than into the x-y plane. We will see in the next section that this leads to a shift of energy levels compared to an *idealized* QD created by the superposition of quantum wells.

2.3 Energy levels in a lens shaped QD

Energy levels for an electron in an ideal 0D quantum box are given by the sum of three uncoupled quantum wells (see table 2.1). However, optical transitions in a real material involve a electron-hole pair, called exciton, so the effective mass Hamiltonian is :

$$H_0 = \frac{P_e^2}{2m_e^*} + \frac{P_h^2}{2m_h^*} + V(\vec{r}_e) + V(\vec{r}_h) - \frac{e^2}{\epsilon|\vec{r}_e - \vec{r}_h|} \tag{2.5}$$

where ϵ is the dielectric constant of the dot material, $V(\vec{r}_e)$ ($V(\vec{r}_h)$) is the QD potential shape effect for the electron (hole), P_e (P_h) is the momentum operator for the electron (hole). The last term of Eq. 2.5 is the Coulombic interactions between the electron and hole. In the case of strong confinement, that term is smaller than the potential term so that we can consider the hole and electron as independent particles whose wavefunctions are solution of Schrdinger's equation 2.1. Let us look at the effect of the confinement potential on the electronic levels. As mentioned before, QDs grown by SK method form lens shaped half domes of a few nanometers in height and 20-40 nm in diameter. This leads to a stronger confinement in the $\hat{z}$ direction compared to the x-y plane, leading us to the description of SA dots as quantum wells with additional lateral confinement. The form of the potential $V(\vec{r}_{e(h)})$ can thus be separated into the potential of a QW of thickness l_0, $V(z)$, and a radial potential, $V(\rho)$ (see figure 2.4). The adiabatic approximation [42] is used for the radial part, so that the lens shape is cut into n quantum wells along ρ. Using the hard wall approximation, the Taylor expansion of $V(\rho)$ and taking $A = l_0/\rho_0$ fairly small as is the case with QDs used, here Schrdinger's equation is then separable into a QW z part and two harmonic oscillators in the x-y plane, with eigenenergies [43] :

$$E_z = \frac{\hbar^2\pi^2}{2m^*l_0^2} \tag{2.6}$$

$$E_x + E_y = (n_x + n_y + 1)\hbar\omega = (n_x + n_y + 1)\frac{2}{\pi}\sqrt{\frac{2A^2}{1+A^2}}\frac{\hbar^2\pi^2}{2m^*l_0^2} \tag{2.7}$$

where $n_x, n_y = 0, 1, 2, ...$ After these approximations, we obtain a discrete energy spectrum, as with an ideal 0D structure. Quantum number n_z is omitted, as $A \approx 0.2$, $(n_x + n_y + 1)$ would need to be bigger than 22 in order to reach the second QW level in the z direction. Usually, because of fast carrier relaxation, the density of carriers injected for optical measurements only fills levels below $(n_x + n_y + 1) \simeq 4$. Furthermore, the QW barrier is actually finite, confining only approximately 5 energy levels, supporting the inclusion of only the first QW energy level. The approximation of lens dots by harmonic oscillators in x-y plane and QW in z direction has been confirmed by magneto-PL measurements [22] and is a very elegant approach, simplifying energy level calculations. In such experiments, the energy level structure in a magnetic field is represented by Fock-Darwin states, displaying characteristics such as Zeeman splitting and spin-orbit coupling [28]. Energy levels of a lens shaped QD are represented in figure 2.5. Note that the corresponding atomic shell notation s, p, d isn't exactly the same as

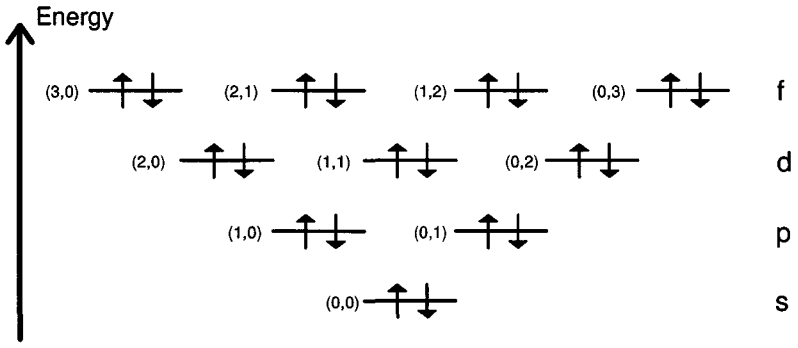

Figure 2.5: Conduction band energy levels of a lens shaped QD, (n_x, n_y) representing the quantum numbers for each of the harmonic oscillators

for atoms or a perfect quantum dot as for instance the p-shell can only accommodate 4 electrons instead of 6.

The previous development leads to the same kind of electronic structure for holes in the valence band, but inverted because of the holes negative effective mass. In fact, the valence band is a degenerate p-like shell and the conduction band, s-like because we are dealing with III-V materials, with 8 electrons in a unit cell forming hybridized sp^3 orbitals. This results into one bonding and antibonding level, separated by a gap, the higher energy completely empties the antibonding band (created in a bulk III-V crystal) forming the conduction band. As the lowest energy antibonding level is s-type, we shall refer to the conduction band as s-like with angular momentum $l = 0$. The bonding orbitals separate into a filled s orbital closer to the atom's nucleus and three degenerate p-like orbitals of angular momentum $l = 1$ [44] which constitute the valence band. Corresponding Bloch functions for the electrons are thus $|S\rangle$ (s orbital) and $|X\rangle\,|Y\rangle\,|Z\rangle$ (p orbitals). As valence electrons carry spin and an angular momentum, spin-orbit coupling has to be considered. Kane [8] was the first to introduce spin in $k \cdot p$ theory. The basis for valence hole states is now given by the total angular momentum operator $\vec{J} = \vec{l} + \vec{\sigma}$ and the projection of the angular momentum on the z direction (m_j), where σ is the spin of the electron. Basis vectors are summarized in table 2.2; bands with $m_j = 3/2$ are associated with heavy-holes (HH) as their effective mass derived from eigenenergies is higher than for $m_j = 1/2$, the light-holes (LH) [45]. At $k = 0$ in a bulk substance, taking the conduction band as the energy reference, the LH and HH bands are degenerate at energy $-\epsilon_0$, while the split off band is separate, at energy $-\epsilon_0 - \Delta$ energy. However, as SA QDs are strained structures, biaxial strain splits the heavy-holes and light-holes (by roughly 0.12 eV for InAs/InP lens QDs), sending the LH band closer to the split-off

band. This is why most of the time the single HH band approximation is taken for the valence band of QDs [46, 47]. In fact, the LH-HH mixing has been estimated to be lower than 10% by Saito et al. for a single InAs/GaAs QD [48]. The above calculations mean that we can apply the effective mass theory to calculate VB states in QDs with the assumption that we are dealing with HH.

$\|J, m_j\rangle$	ψ_{J,m_j}	$\epsilon_i(k=0)$	e-h band type
$\|1/2, 1/2\rangle$	$i\|S\uparrow\rangle$	0	core S electron
$\|3/2, 1/2\rangle$	$-\sqrt{\frac{2}{3}}\|Z\uparrow\rangle + \frac{1}{\sqrt{6}}\|(X+iY)\downarrow\rangle$	$-\epsilon_0$	light hole
$\|3/2, 3/2\rangle$	$\frac{1}{\sqrt{2}}\|(X+iY)\uparrow\rangle$	$-\epsilon_0$	heavy hole
$\|1/2, 1/2\rangle$	$\frac{1}{\sqrt{3}}\|Z\uparrow\rangle + \frac{1}{\sqrt{3}}\|(X+iY)\downarrow\rangle$	$-\epsilon_0 - \Delta$	split-off hole
$\|1/2, -1/2\rangle$	$i\|S\downarrow\rangle$	0	core S electron
$\|3/2, -1/2\rangle$	$-\sqrt{\frac{2}{3}}\|Z\downarrow\rangle - \frac{1}{\sqrt{6}}\|(X-iY)\uparrow\rangle$	$-\epsilon_0$	light hole
$\|3/2, -3/2\rangle$	$\frac{1}{\sqrt{2}}\|(X-iY)\downarrow\rangle$	$-\epsilon_0$	heavy hole
$\|1/2, -1/2\rangle$	$\frac{1}{\sqrt{3}}\|Z\uparrow\rangle - \frac{1}{\sqrt{3}}\|(X-iY)\uparrow\rangle$	$-\epsilon_0 - \Delta$	split-off hole

Table 2.2: Basis vectors, wavefunctions, energy gap relative to conduction band for Kane $k \cdot p$ basis with spin-orbit coupling [41].

After all these considerations, we are finally able to represent the band structure of a lens shaped SA QD. Figure 2.6 shows the band structure for a InAs/InP lens-shaped self-assembled quantum as calculated by 8x8 $k \cdot p$ theory, including strain effects. Band calculations were done on a 25 nm diameter by 3.5 nm height lens shaped QD by Gong et al. [41]. We clearly see that the biaxial strain splits HH and LH bands. The band structure of InAs/InP dots is quite different from InAs/GaAs, as the former bandgap alignment confines holes and the latter electrons more deeply. The physical shape of the QDs also modifies the band structure and shifts the energy levels. As the diameter (or height) of the QD gets higher, more states are confined in the QD and the effective

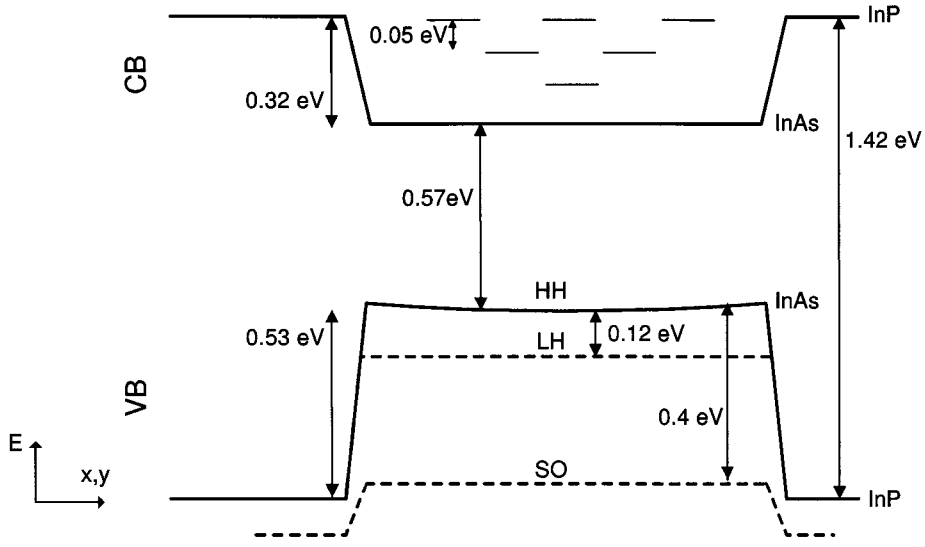

Figure 2.6: Conduction band of a 25 nm diameter by 3.5 nm height InAs/InP QD confines only 3 energy states. The valence band shows splitting between the LH and HH bands and the split-off band (SO) is barely confined in the QD [41]. Only the first hole states are represented for simplicity.

bandgap (or exciton energy) value drops. This effect implies that the emission energy of a QD can be tailored uniquely by changing the shape or dimensions of a QD.

2.4 Optical selection rules of QDs

We have derived the energy level structure of a QD, but optical transitions such as absorption and emission cannot necessarily occur between any conduction and valence band energy level. To derive the optical selection rules, we begin by treating the case of a photon absorption, which translates directly into emission processes. If an electron is subjected to the electromagnetic field of a photon, the excitation of the electron from the VB to the CB can occur [49]. The Hamiltonian for an electron (equation 2.5) has to include the effect of light, so it is modified to include the effect of a vector potential A_{em}. The single electron momentum p becomes $p + eA_{em}/c$:

$$H = H_0 + \frac{e}{2m_0 c}(p \cdot A_{em} + A_{em} \cdot p) \tag{2.8}$$

As A_{em} is a time dependent potential, the transition probability for an interband

transition, from an initial state $|i\rangle$ of the VB to a final state $|f\rangle$ of the CB is given following Fermi's golden rule. The transition rate between these two states is given by

$$P = \frac{2\pi}{\hbar} |\langle f| V |i\rangle|^2 \delta(E_f - E_i - \hbar\omega) \tag{2.9}$$

Under the electric dipole approximation,

$$V = \frac{ieF}{2m_0\omega} \vec{\epsilon} \cdot \vec{p} \tag{2.10}$$

where m_0 is the electron free mass, F is the amplitude of the oscillating electric field, $\vec{\epsilon}$ is the electric field polarization and $\vec{p}$ is electron's momentum. The delta function in equation 2.9 tells us that the difference in energy between the two energy levels involved must be equal to the energy of the absorbed photon. Further selection rules will be imposed on the allowed energy states for interband transitions. Electrons can be described as a combination of atomic Bloch function μ and envelope type wavefunction as ϕ, so that [50]

$$\begin{aligned} \langle f| \vec{\epsilon} \cdot \vec{p} |i\rangle &= \vec{\epsilon} \cdot \langle \mu_f| \vec{p} |\mu_i\rangle \langle \phi_f| \phi_i\rangle \\ |i\rangle, |f\rangle &= |\Psi_i\rangle, |\Psi_f\rangle = |\mu_i\rangle |\phi_i\rangle, |\mu_f\rangle |\phi_f\rangle \end{aligned} \tag{2.11}$$

The Bloch "atomic" wavefunctions aren't dependent on structural properties of the sample, i.e. the shape of the confining potentials. However, the envelope functions, extending into the whole quantum dot, feel the effect of the dimensionality and shape of the potential. In $\hat{z}$, the overlap integral for the envelope wavefunctions confined into a lens-shaped QD with infinite barriers is given by :

$$\langle \phi_f| \phi_i\rangle = \int \phi_e \phi_h dz = \int \frac{2}{l} \text{Sin}\left(\frac{\pi n_z^e}{l} z\right) \text{Sin}\left(\frac{\pi n_z^h}{l} z\right) dz \tag{2.12}$$

where the sine functions the wavefunctions of an infinite QW. As the sine functions form an orthogonal basis of states for the square well potential, we see that $n_z^e = n_z^h$ is the only case for which the overlap integral is non-zero. In the x-y plane, the Hermite functions present in the harmonic oscillator wavefunction form an orthogonal basis, so the same kind of selection rules $n_x^e = n_x^h$ and $n_y^e = n_y^h$ are found for the envelope functions of the 2D harmonic oscillator in the x-y plane. As mentioned before, only one QW state

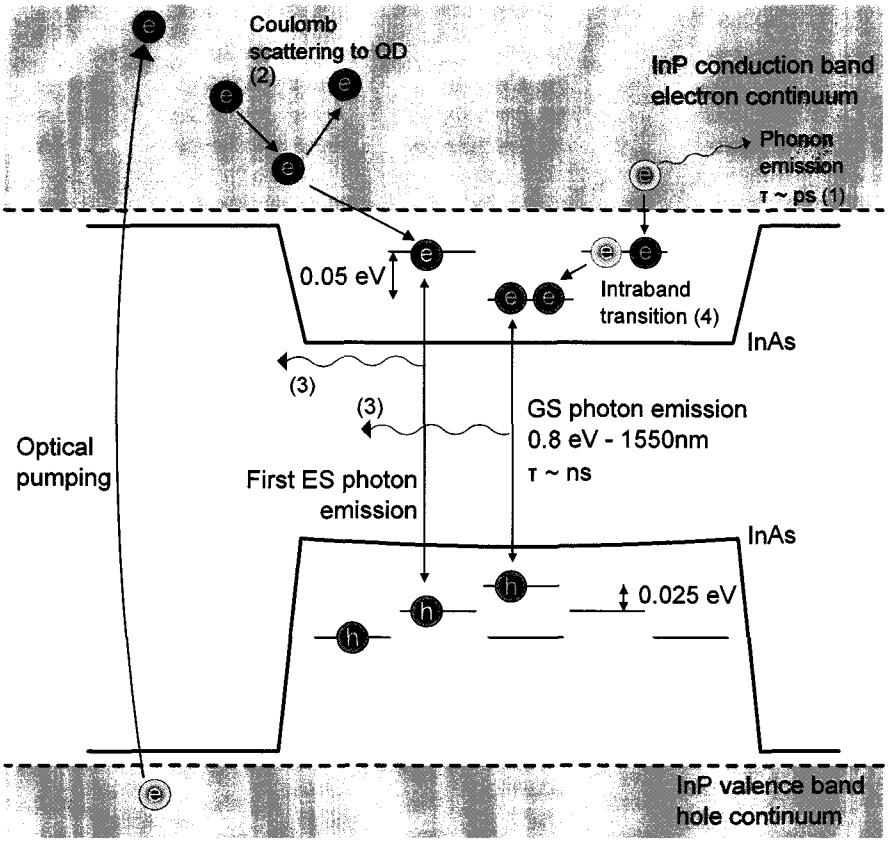

Figure 2.7: Different optical and non optical processes occurring in QD structure [45].

is confined in the quantum dot, so $n_z^e = n_z^h = 1$. Allowed optical transitions are thus represented vertically in a band diagram (see figure 2.7), so that only excitonic recombinations involving the electron and hole ground state (GS) and excited states (ES) are allowed for photon emission.

In the preceding development, we have assumed a resonant absorption, the energy of the photon is exactly the same as the energy levels energy gap i.e. $\hbar\omega = E_f - E_i$. Experimentally, electrons are injected optically non resonantly into the InP conduction band continuum of the barrier material (InP, InGaAsP or GaAs). Then these carriers lose their energy by non-radiative processes such as fast phonon emission (1) or Auger processes (2) (especially at high carrier density) [51], exiting the energy continuum to fall into a lower energy QD energy level. The interband Auger process, although less probable, can lead to quenching of QD PL, as the carriers are pushed outside of the dot

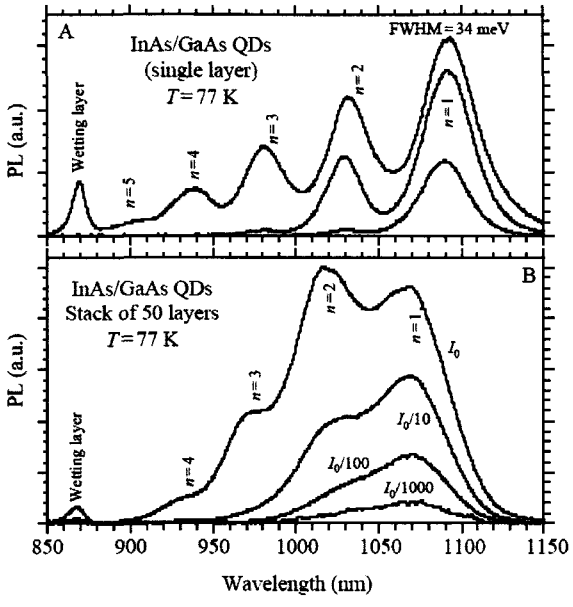

Figure 2.8: Evidence of state filling for an ensemble of QD as excitation power is increased. p, d, f shells appear at higher energies [53]. Reproduced by permission of Elsevier.

[52]. When the carriers occupy the QD levels, interband transitions (3) provide the PL photons and intraband (4) radiative transitions can also occur in the CB and VB. Combined with selection rules, we'll see in section 2.5 that total angular momentum J has to be ± 1 to have a bright (emitting) state, as the photons are bosons. Thus, an additional selection rules is imposed on spins : spin of electron and holes must be opposite, in order to have $J = \pm 1$. In PL, the only quantity that we are measuring is the emitted photon energy, so how do we know we are probing QDs?

Probably one of the easiest ways to ensure that QDs have been obtained is by observation of state-filling in the dots. When the number of carriers injected by PL exceeds the number of recombination of the GS, excited states are populated, showing up on the PL as gaussian shaped peaks of higher energies. Experimentally, this is done by increasing the power of the excitation laser. Note that if we probed a single QD, one would expect only a very narrow emission line in the PL for each shell because of the discrete DOS. However, as we usually probe ensemble of dots, the shell peaks are much wider because they include contribution of thousands of QDs. PL spectrum of a typical InAs/GaAs QD ensemble sample measured by Fafard et al. [53] (figure 2.8) shows that we are indeed probing QDs as by changing excitation power the s shell emission expands into a p (n=1), d (n=2), f (n=3) shell emission as one would expect from an artificial

atom. The intensity of each excited state is a factor of the number of the states available, the inter-sublevel relaxation time and the radiative recombination lifetime of the GS and ES [54, 55]. Thus, even if the number of states is higher for ES, it is common (see top of figure [53]) to see a higher GS or ES intensity, depending on the excitation power per QD layer. Here, a spectrum of SA InAs/GaAs QD ensemble is shown, contrarily to a InAs/InP QD ensemble, which has a bigger IB. In the case of InAs/InP QDs, the ES overlap, hiding the state filling effect. Compared to the GS emission, the ES emission has completely different optical polarization properties, so only the GS (s shell) polarization emission properties are investigated to gain insight on the edge polarization emission. With this in mind, we investigate the QD polarization properties of the GS emission in the next section, which will give us additional information on the QD morphology.

2.5 Optical polarization properties of QDs

The energy of the photon emitted gives us information on the structure of the QD, but the polarization of the light is also affected by the QD shape, depending on the hole state involved in the GS transition. To get insight on the polarization of emitted light from QDs, we need to go back to equation 2.12 and evaluate the atomic wavefunction part, $\langle \mu_f | \vec{p} | \mu_i \rangle$. At the center of the Γ_8 zone, Bastard [56] showed that the HH transitions strength is three times the LH transition for degenerate HH LH bands (see figure 2.9). Using the atomic Bloch wavefunctions as presented in table 2.2, it is possible to express the dipole matrix elements without making any potential assumption (so no dimensionality assumption) [50] :

$$\sum_{m_s} \left| \langle \Psi^c_{m_s} | \, \epsilon \cdot \mathbf{p} \, | \Psi^v \rangle \right|^2 = \left(\frac{m_0 P}{\hbar} \right)^2 \begin{cases} \frac{4}{3} J^2_{1/2} & \text{in } \hat{z} \\ \left(\frac{1}{3} J^2_{1/2} + J^2_{3/2} - \frac{2}{\sqrt{3}} (J_{3/2} J_{1/2}) cos(2\phi) \right) & \text{in xoy} \end{cases} \tag{2.13}$$

Where $J_{m_j} = \langle \phi_e(\mathbf{r}) | \, \phi_{m_j}(\mathbf{r}) \rangle$ are the overlap integrals of the QD valence and conduction bands envelope wavefunctions, θ is the angle relative to $+\hat{z}$ and ϕ is the angle relative to $+\hat{x}$ in the xoy plane, the amplitude in $\hat{z}$ (xoy) being for angle $\theta = 0$ ($\theta = \pi/2$). In equation 2.12, only the overlap functions J_{m_j} are dependent on dimensionality, as the envelope wavefunctions extend outside the dots. The coefficients preceding the J_{m_j} in equation 2.13 are related to the "atomic" part of the wavefunction (Bloch part), independent of

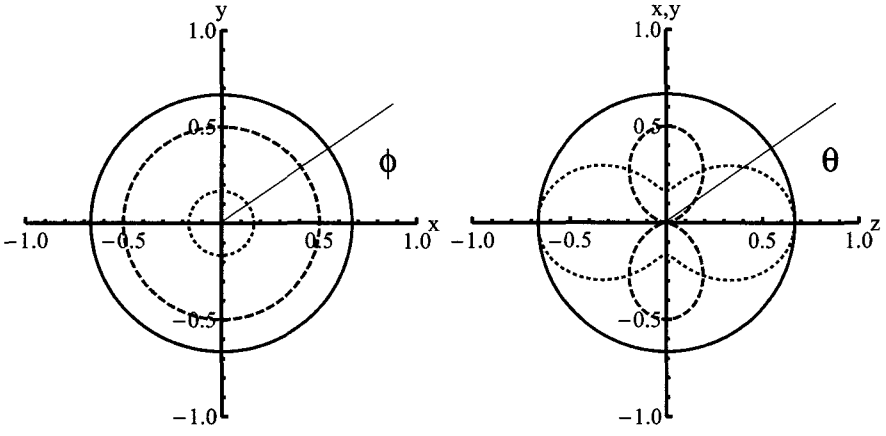

Figure 2.9: Electric dipole intensity in a bulk material. Blue curve represents HH contribution, green LH and red the total dipole intensity.

dimensionality. Note that the last term in xoy dependent on $\mathrm{Cos}(2\phi)$ is only needed in the case of coupled HH and LH bands. Considering both LH and HH bands for a 3D bulk substance, the intensity of the electric dipole strength is constant looking from the top or the side of the sample, as one would expect because of the isotropic shape of the material. However, the LH contribution to the total intensity changes if we collect the emission from the side or the top of the dots (see figure 2.9). Hence, differentiation of the hole type contribution by edge and top measurements of emitted light is not possible as the total detected intensity is constant.

As only the envelope functions can feel the effect of potentials, their choice is critical in the description of QDs. A QD lens can be approximated by two harmonic oscillators in x-y plane and a QW in the z direction, with wavefunctions :

$$\begin{aligned}
\phi_e(x,y) &= \frac{\beta_e}{\sqrt{\pi 2^{n_x+n_y}(n_x)!(n_y)!}} e^{-\beta_e^2(x^2+y^2)/2} H_{n_x}[x\beta_e] H_{n_y}[y\beta_e] \\
\phi_{m_j}(x,y) &= \frac{\beta_{m_j}}{\sqrt{\pi 2^{n_x+n_y}(n_x)!(n_y)!}} e^{-\beta_{m_j}^2(x^2+y^2)/2} H_{n_x}[x\beta_{m_j}] H_{n_y}[y\beta_{m_j}] \\
\Gamma(z) &= \sqrt{\frac{2}{a}}\mathrm{Cos}[\frac{\pi z}{a}] \\
\phi_{e(m_j)}(x,y,z) &= \Gamma(z)\phi_{e(m_j)}(x,y)
\end{aligned} \tag{2.14}$$

where $\phi_{e(m_j)}(x,y,z)$ is the whole electron (hole, m_j representing HH ($m_j = 3/2$) or LH ($m_j = 1/2$) wavefunction), $\beta_{e(m_j)} = \sqrt{\frac{m_{e(m_j)}\omega_{e(m_j)}}{\hbar}}$, $\omega_{e(m_j)}$ is the harmonic oscillator energy, H_{n_x} and H_{n_y} are the Hermite polynomials, n_x, n_y are the harmonic oscillator quantum numbers in the x and y directions, a is the well depth and $m_{e(m_j)}$ is the effective mass of the electrons, HH or LH. The first two expression are the harmonic oscillators in the plane and $\Gamma(z)$ is the QW wavefunction. If we consider only the GS emission, $n_x = n_y = 0$ and the last expressions reduces to

$$\phi_e(x,y) = \frac{\beta_e}{\sqrt{\pi}} e^{-\beta_e^2(x^2+y^2)/2} \tag{2.15}$$

$$\phi_{m_j}(x,y) = \frac{\beta_{m_j}}{\sqrt{\pi}} e^{-\beta_{m_j}^2(x^2+y^2)/2} \tag{2.16}$$

Calculating the overlap functions for HH and LH, we get

$$\begin{aligned} J_{m_j} &= \int_{-a/2}^{a/2}\int_{-\infty}^{\infty}\int_{-\infty}^{\infty} \phi_e(x,y)\phi_{m_j}(x,y)\Gamma^2\, dx\, dy\, dz \\ &= \int_{-a/2}^{a/2}\int_{-\infty}^{\infty}\int_{-\infty}^{\infty} \frac{\beta_e}{\sqrt{\pi}} e^{-\beta_e^2(x^2+y^2)/2} \frac{\beta_{m_j}}{\sqrt{\pi}} e^{-\beta_{m_j}^2(x^2+y^2)/2}\Gamma^2\, dx\, dy\, dz \\ &= 2\frac{\beta_e\beta_{m_j}}{\beta_e^2+\beta_{m_j}^2} \end{aligned} \tag{2.17}$$

Experimentally, the overlap coefficient for HH (LH) is associated with the intensity of the TE (TM) mode for the edge emission, because HH do not contribute to the TM (z direction) mode. This can be seen in equation 2.13, as $J_{1/2}$ appears in the $\hat{z}$ direction, contrarily to $J_{3/2}$. To characterize the polarization anisotropy of the emission, we introduce the degree of polarization (DOP), defined as

$$DOP = \frac{I_{TE} - I_{TM}}{I_{TE} + I_{TM}} \tag{2.18}$$

A negative DOP means that the LH contribution is bigger than the HH. However, due to the piezoelectric effects and strain into QDs [48] the HH and LH bands are non-degenerate so that LH contribute for roughly 5% of the GS wavefunction behavior of holes. Nevertheless, their contribution is important, as if only HH were considered, the dipole intensity would only be TE polarized for dot edge emission, which isn't the case as polarization PL results will show in section 3.2.

We now have derived the general expressions to find the DOP for top and edge emission. In the following, the effect of the LH behavior and of the in plane QD anisotropy is included to see how the polarization properties are affected. First, we take into consideration that we don't have degenerate LH HH bands, but a $I_{1/2} = 5\%$ LH wavefunction behavior. Accordingly, the wavefunction for the valence band is expressed as $\Psi^v = I_{1/2}\phi_{1/2}(x,y,z)\mu_{1/2} + I_{3/2}\phi_{3/2}(x,y,z)\mu_{3/2}$. Furthermore, we introduce the overlap elements calculated in equation 2.17 into the general expression for dipole matrix elements :

$$\sum_{m_s} |\langle \Psi^c_{m_s} | \epsilon \cdot \mathbf{p} | \Psi^v \rangle|^2 = \left(\frac{m_0 P}{\hbar}\right)^2 \left[\left(I^2_{3/2}J^2_{3/2} + \frac{1}{3}I^2_{1/2}J^2_{1/2} - \frac{2}{\sqrt{3}}I_{1/2}I_{3/2}(J_{3/2}J_{1/2})cos(2\phi)\right)\sin^2(\theta) + \frac{4}{3}I^2_{1/2}J^2_{1/2}\cos^2(\theta)\right] \tag{2.19}$$

where $I_{1/2} = 5\%$ ($I_{3/2} = 1 - I_{1/2} = 95\%$) is the percentage of the intensity associated with LH (HH).

For the top QD emission, contributions of LH and HH are both circular and any anisotropy in polarization can be linked to the LH HH coupling term. However, SA QDs are usually slightly elongated, modifying the harmonic wavefunctions and can cause polarization anisotropy as well. This is reflected in an anisotropy of the oscillator energy in the x-y plane, so that $\beta_e(x) = \alpha\beta_e(y)$ and $\beta_{m_j}(x) = \alpha^\Lambda\beta_{m_j}(y)$. Here the oscillating frequency is taken bigger in $\hat{x}$ because the dot is elongated along $\hat{y}$, with a shape anisotropy $\alpha = b/a$ (see figure 2.4). In order to get non-constant overlap coefficients, the shape anisotropy has to affect the wavefunction of the electrons and holes at a different rate [57]. This is included as an adjustable parameter $0 < \Lambda < 1$ in $\beta_{m_j}(x)$. Physically this parameter is justified by the stronger hole confinement in InAs/InP QDs, $\Lambda = 1$ being the limiting case where the anisotropy doesn't affect the DOP. In that case, the wavefunctions for holes and electrons would change proportionally, so the overlap integral would be constant.

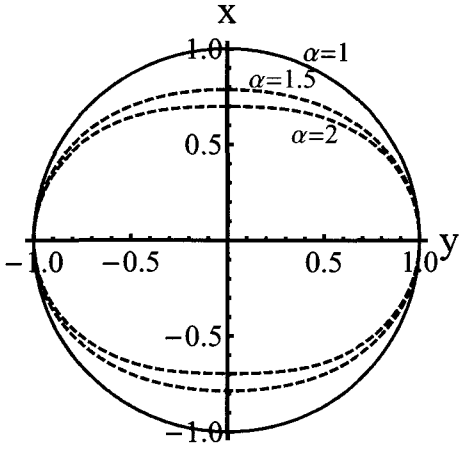

(a) Top dipole intensity for different anisotropies α and Λ=0.1

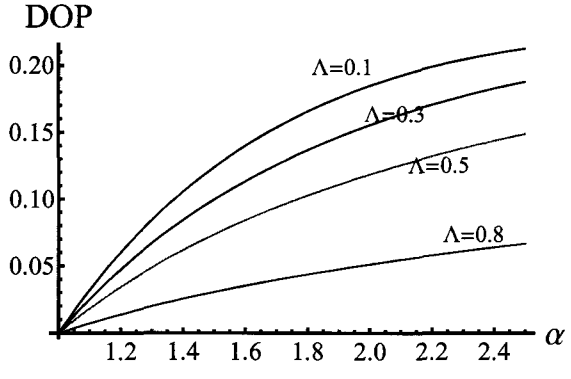

(b) Effect of the parameter Λ on the DOP

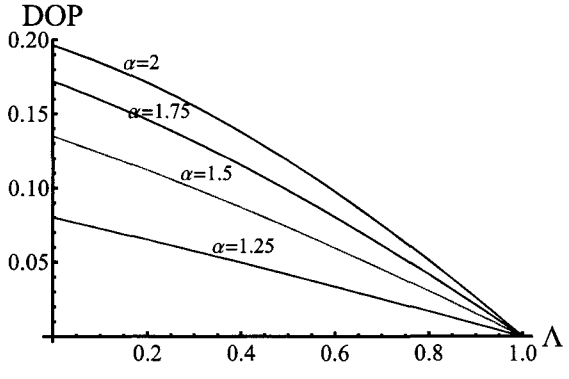

(c) Effect of the parameter α on the DOP

Figure 2.10: Top dipole intensity and effect of parameters α and Λ. In (a) the anisotropy of the dot modifies the degree of polarization, starting from an isotropic dot ($\alpha = 1$, DOP=0%) to an elogated dot with $\alpha = 2$ (DOP=18%)

X-Y plane

Let us investigate the effect of anisotropy on polarization, under the assumption that the LH HH coupling term proportional to $Cos(2\phi)$ is zero. If we pose different overlap values in the x and y directions and go back a few steps in equation 2.19,

$$\sum_{m_s} \left|\langle \Psi^c_{m_s}| \epsilon \cdot \mathbf{p} |\Psi^v\rangle\right|^2 \propto \left[I^2_{3/2}J_{3/2}(x,y)^2 + \frac{1}{3}I^2_{1/2}J_{1/2}(x,y)^2\right] \tag{2.20}$$

$$J_{m_j}(\hat{x}) = \int_{-\infty}^{\infty} \phi_e(x)\phi_{m_j}(x)\,dx = \sqrt{\frac{2\alpha^{\Lambda+1}\beta_{ey}\beta_{m_jy}}{\alpha^2\beta^2_{ey} + \alpha^{2\Lambda}\beta^2_{m_jy}}} \tag{2.21}$$

$$J_{m_j}(\hat{y}) = \int_{-\infty}^{\infty} \phi_e(y)\phi_{m_j}(y)\,dy = \sqrt{\frac{2\beta_{ey}\beta_{m_jy}}{\beta^2_{ey} + \beta^2_{m_jy}}} \tag{2.22}$$

$$J_{m_j}(x,y)^2 = J_{m_j}(\hat{x})^2 Cos(\phi)^2 + J_{m_j}(\hat{y})^2 Sin(\phi)^2 \tag{2.23}$$

then dot anisotropy is taken into account for top emission. As both LH and HH have circular contributions, the change in LH percentage of the wavefunction doesn't change the DOP, so with a zero LH-HH mixing term any polarization anisotropy is solely caused by dot shape anisotropy. By calculating the J_{m_j} values and inserting them into equation 2.19, we obtain the polar plot represented in figure 2.10 (a) for the top emission. As can be seen in figure 2.10 (a) an increasing anisotropy parameter α increases the DOP, up to 18% for $\alpha = 2, \Lambda = 0.1$. In (b), the effect of the parameter Λ on the DOP is shown. For a smaller Λ, holes are less affected by the anisotropy of the dot than electrons, thereby increasing the DOP. Finally, in figure 2.10 (c) the increase of anisotropy parameter α increases the DOP as expected from the enhanced dipole strength along the elongated direction. Note that the limiting case would be for $\Lambda = 1$ or $\alpha = 1$, with a zero DOP value (isotropic polarization).

X-Z and Y-Z planes

For the edge DOP, the treatment of the DOP is completely different, as the HH (LH) provides TE (TE and TM) mode. This means that if the TM signal collected is non-zero, there must be a contribution of the LH. Here the in plane anisotropy has a more subtle effect, making only an amplitude difference between the x and y axis, as can be seen by comparing $J_{m_j}(\hat{x})$ (eq. 2.21) and $J_{m_j}(\hat{y})$ (eq. 2.22). We can conclude that most of the effect on the DOP will be related to the LH behavior of the wavefunction. Reexpressing

equation 2.19 for the planes X-Z and Y-Z respectively,

$$\sum_{m_s} \left|\langle \Psi^c_{m_s} | \epsilon \cdot \mathbf{p} | \Psi^v \rangle\right|^2 \propto \left[I^2_{3/2} J_{3/2}(x,z)^2 + I^2_{1/2} J_{1/2}(x,z)^2 - \frac{2}{3} I_{1/2} I_{3/2} J_{3/2}(\hat{x}) J_{1/2}(\hat{x})\right]$$

$$\sum_{m_s} \left|\langle \Psi^c_{m_s} | \epsilon \cdot \mathbf{p} | \Psi^v \rangle\right|^2 \propto \left[I^2_{3/2} J_{3/2}(y,z)^2 + I^2_{1/2} J_{1/2}(y,z)^2 - \frac{2}{3} I_{1/2} I_{3/2} J_{3/2}(\hat{y}) J_{1/2}(\hat{y})\right]$$

with the overlap integrals

$$J_{3/2}(x,z)^2 = J_{3/2}(\hat{x})^2 Sin(\theta)^2 \tag{2.24}$$

$$J_{3/2}(y,z)^2 = J_{3/2}(\hat{y})^2 Sin(\theta)^2 \tag{2.25}$$

$$J_{1/2}(x,z)^2 = \frac{4}{3} Cos(\theta)^2 + \frac{1}{3} J_{1/2}(\hat{x})^2 Sin(\theta)^2 \tag{2.26}$$

$$J_{1/2}(y,z)^2 = \frac{4}{3} Cos(\theta)^2 + \frac{1}{3} J_{1/2}(\hat{y})^2 Sin(\theta)^2 \tag{2.27}$$

Figure 2.11 summarizes the effect on DOP of anisotropy parameters α, Λ and of the LH proportion. As expected from an exclusively HH contribution to the emission, the emission from the edge of the dots is highly TE polarized, resulting in a high DOP. A 20% LH proportion was chosen to amplify the TM contribution, but is a realistic value as shown in $8k \cdot p$ ab-initio calculations done by Saito et al. [48], which showed that closely stacked InAs/GaAs dots can achieve higher than 20% LH behavior due to reduced biaxial strain in the QDs. As can be seen in figure 2.11, the LH proportion is the most important factor on the DOP for edge measurements, compared to the effect of Λ (figure 2.11 (c)) and α (figure 2.11 (d)). It is important to stress that this QD polarization properties model is a basic description under the envelope approximation, for a single QD. It does not take into account strain [58], piezoelectric effects [59], ES transitions [57], non-infinite QW barrier in $\hat{z}$, electron hole exchange interaction [57] and QD coupling in a stack due to low dot period [48].

The numerical parameters used for the polar plots are $m_e = 0.022\ m_0$; $m_{HH} = 0.34\ m_0$; $m_{LH} = 0.026\ m_0$; ω_e=0.06 eV ; ω_{m_j}=0.03 eV. These polar plots will help us in section 3.2 to get qualitative insight on the effect of stacking period on the LH behavior of the dot, which in turn can give insight on the additional strain or coupling between the dots. LH are often completely neglected when treating the optical properties of QDs, but experimental polarization polar plots show that the LH contribution is especially im-

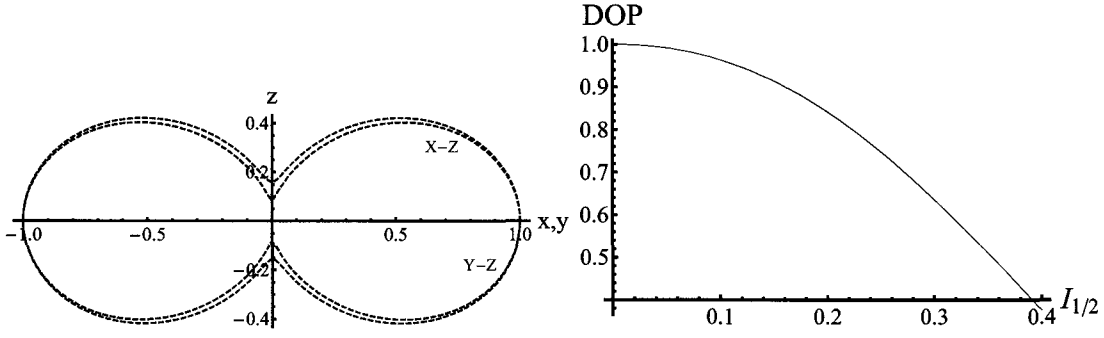

(a) Edge dipole intensity in the X-Z and Y-Z plane (b) Effect of the LH proportion on the DOP

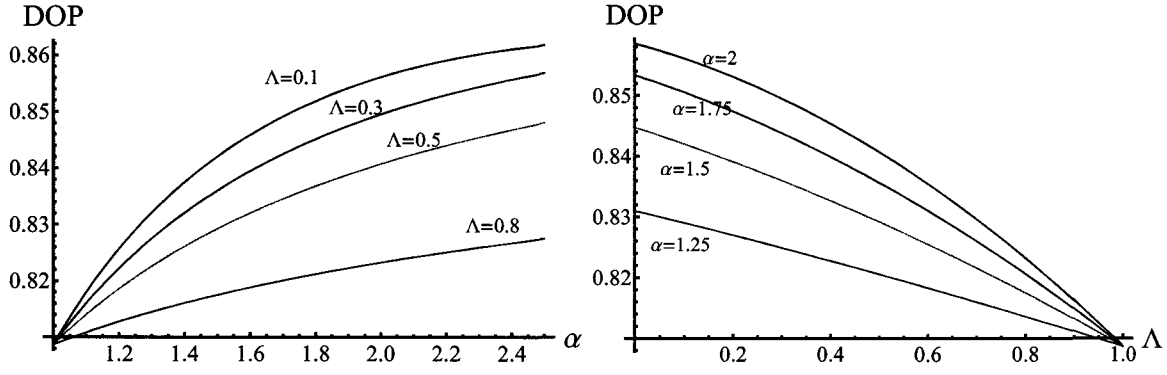

(c) Effect of Λ on the DOP, $I_{1/2} = 20\%$ (d) Effect of α on the DOP, $I_{1/2} = 20\%$

Figure 2.11: Edge dipole intensity and effect of parameters α and Λ. In (a) the 20% LH contribution contributes to the TM mode in X-Z (Y-Z) plane, resulting in a 83% (72.5%) DOP. Panel (b) shows that in the case of a big LH contribution to the wavefunction, the DOP drops significantly. For (c) and (d), curves follow a trend similar to calculations from the top of the anisotropic dots. The difference is that the DOP is much higher for an isotropic dot ($\alpha = 1$) due to the major HH contribution on the polarization properties.

portant in edge polarization measurements. Note that the model introduced here doesn't directly take into account the coupling between the QDs in a stack due to the envelope approximation. The dot coupling is mediated by the reduction of biaxial strain, which can only be included in an atomistic model such as $8k \cdot p$ ab-initio calculations done by Saito et al. [48]. However, the model gives us insight on the LH behavior of single QDs, allowing us to quantify the coupling in a stack.

Now we know what to expect experimentally for the PL and Pol-PL experiments done on QDs, the subject of the next chapter, beginning with the PL of stacks and the effect of the insertion of a GaP strain compensating layer. Then, we modify the dot period of the stack to investigate the effect on the polarization properties, for the long term goal of developing a polarization independent QD SOA.

Chapter 3

InAs/InP quantum dot devices in the 1550 nm range

In the previous chapter, the polarization properties for quantum dot edge emission were investigated for the long term goal of developing polarization independent QD SOAs for fiber optic telecommunications systems. In this chapter, we follow up experimental work where the QD properties will be investigated by polarization PL (Pol-PL) in section 3.1 (3.2). We will use polarization properties concepts developed in our theory section 2.5 to modify the QD stack in order to control the polarization. This control is a long term objective of our project, which will eventually be included in our devices, such as SOAs. However, on the short term, our goal is to develop high performance QD lasers operating in the telecommunications bands to replace the existing QW lasers for MWL and MLL applications. Characterization of the laser performances will be presented in section 3.3. But first, in section 3.1 we present standard PL results obtained from our QD samples. This is intended as an introduction to the different building blocks we will need in sections 3.2 and 3.3. The description of the PL setup and experiment will be useful to introduce the Pol-PL setup, and the PL results on QD stacks, QDs with GaP underlayer and annealed QDs will be useful to guide our studies in sections 3.2 and 3.3.

3.1 Photoluminescence of QDs

Photoluminescence is used to optically probe the excitonic states of the QDs, giving information on the bandgap and energy states of the QD material. Carriers are injected

non resonantly into the continuum of states of the substrate, contrarily to a laser structure where carriers are injected electrically through the p-n junction. The latter, contrarily to PL, gives information on the whole laser structure. In a way, PL is the bridge between the materials and the devices, informing us on the bandgap, bandwidth of emission and purity of materials, so that material engineering can be optimized before any kind of nanofabrication is done, a time consuming and costly step.

3.1.1 Photoluminescence setup

Any PL setup is made of three main components : 1- the excitation sources such as lasers, which inject the carriers in the sample, 2- the detectors, which analyze the light coming out of the sample and (optionally) 3- a sample cooling system, such as a cryostat, which allows measurement of low emission samples. Different excitation sources and detectors used in the PL setup are represented in figure 3.1.

The excitation sources were the second harmonic wave of a YVO_4 green laser @ 532 nm and the Ti-Saph laser tunable from 700 nm to 1000 nm. The main laser used was the YVO_4 for its high power output, providing a non resonant QD excitation (dots emitting around 1.55 μm). As mentioned in section 2.4, the laser power was usually varied between 1 mW and 100 mW to see state filling of the QDs, giving us an insight on the IB of the samples. To vary the power, the laser beam goes through a filter wheel before going through a converging lens focusing the beam on the sample. The light emitted by the sample is isotropically emitted back towards the lens, which collimates the sample emission for analysis by the detectors. This configuration, confocal excitation, has the disadvantage of requiring a 50/50 beam splitter (BS), which dumps half the sample signal before being feeded to the detectors. However, confocal PL is very convenient for alignment purposes, allowing maximal signal recovery, as the detection axis is the same as the excitation axis. On some occasions, when the sample capping layers are thick or the QD layers are deeper in the structure, a longer wavelength laser is needed, as the exciting intensity in function of depth is $I(z) \propto e^{-\alpha z}$, where z is the growth direction of the sample and α is the sample attenuation coefficient [60]. In such cases, a Ti-Saph laser pumped by the YVO_4 laser is used instead, providing an excitation range from 700 nm - 1000 nm. By adding a mirror at point 1 of figure 3.1, the Ti-Saph follows the same path as the YVO_4 laser to excite the sample.

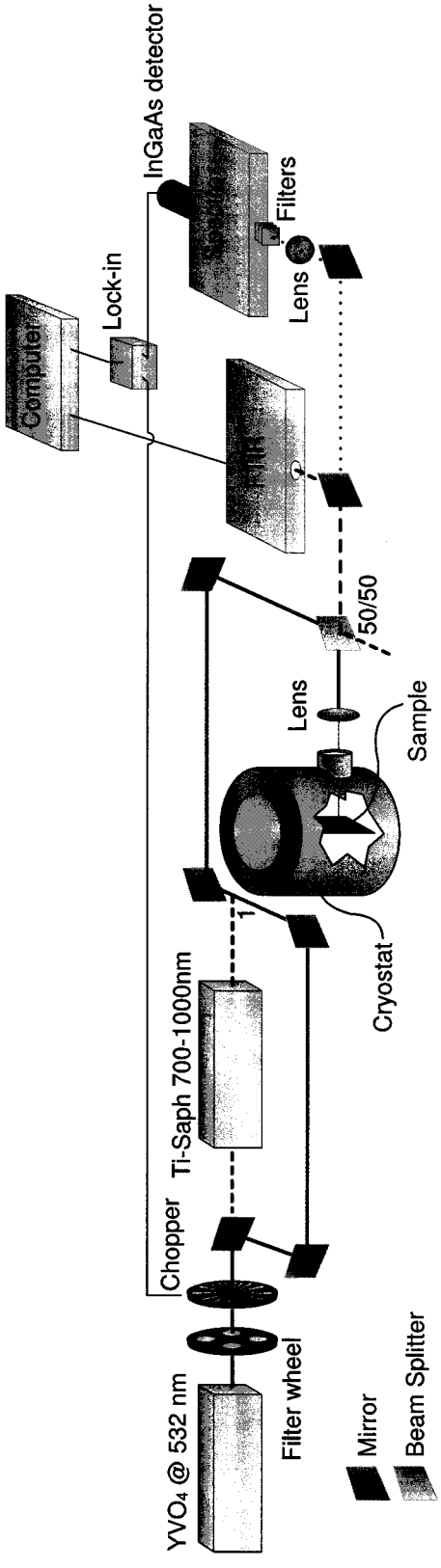

Figure 3.1: Experimental setup for low-temperature PL

At the beginning of this master's, only a double grating step-scan spectrometer with an InGaAs detector was available for detection from 800 nm to 1800 nm, used mainly for chapter 4 the measurements. The sample signal is sent through a lens and a laser line filter @ 1064 nm to filter the first harmonic wave of the YVO_4, which can saturate the detector. As only the signal emitted by the sample is of interest, a long wavepass @ 800 nm is also introduced in front of the spectrometer to suppress the ambient visible and the reflected laser light present in the beam path. Later, a Bruker V80 Fourier Transform Infrared spectrometer (FTIR) with a CaF2 beamsplitter connected to an extended InGaAs detector (700-2200 nm) was bought. The FTIR is a very convenient detector as the detection range is larger, the resolution is higher and the spectrum acquisition is very quick, so most of the PL and the Pol-PL measurements used the FTIR. Details on the instruments used can be found in appendix A.

In some cases, sample signal is buried into a broad background or attenuated by the thermal effects, justifying the need for low temperature PL. These measurements were carried at liquid nitrogen or liquid helium temperatures by switching the cryostat and are insightful to determine the 'real' bandwidth of the emission, which for an ideal QD should be limited by the detector resolution. Low temperature measurements will be mostly useful for the bandwidth characterization of the core layers of SLDs, as will be presented in chapter 4. On the other hand, Pol-PL measurements on the telecommunications laser devices were carried at room temperature (RT), which is their normal operating regime.

3.1.2 Photoluminescence of QDs layers

Sample growth

Samples were grown at NRC in a Riber 32P chemical beam epitaxy (CBE) chamber by Philipp Poole. For the intended laser use of the QDs, QD densities have to be high and the inhomogeneous size distribution of the QDs has to be as small as possible to maximize the gain per wavelength. Typical state of the art growth procedure is described in reference [61] : an InP buffer layer is grown on an InP [001] semi-insulating substrate, followed by a 50 nm layer of lattice matched InGaAsP emitting at 1.15 μm (refered as 1.15Q), acting as the waveguiding core of the sample, because the index of refraction difference provides confinement in $\hat{z}$. In the case of strain compensated stacks, dots are grown on the binary GaP 0.28 nm thick underlayer, followed by a 25 s InAs

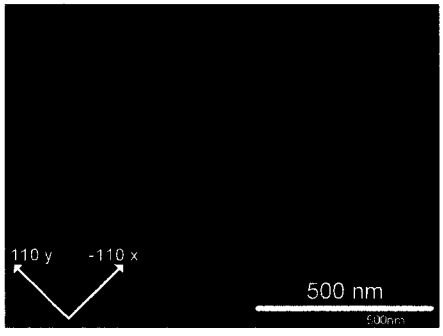

(a) Surface view

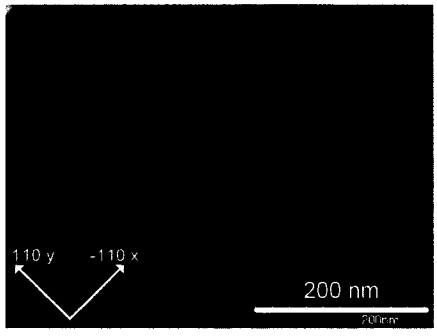

(b) Closeup of surface view

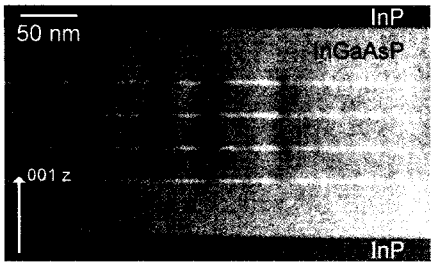

(c) Edge view

Figure 3.2: Surface (a) and closeup (b) SEM pictures of the top QD layer in a four layer stack with 30 nm period. Edge view (c) TEM shows alignment of QDs in the vertical direction.

Figure 3.3: Schematical representation of sample in figure 3.2 (c). Total core thickness is $\approx$ 310 nm.

flow interruption to allow diffusion of Indium for dot formation, which grow following the Stranski-Krastanow method introduced in section 2.2. Dots are then double capped with InGaAsP [62, 63], producing flat shaped dots with a narrow height distribution. This capping procedure begins with the deposition of a thin 1.15Q first cap layer which will define the dot height. Then the growth is interrupted for 30 s with a flux of As/P that effectively trims the exposed top of the QD. When the QD height is equal to the first cap thickness, the second 1.15Q capping is grown, defining the dot period of the stack. This summarizes the growth of a single layer of QDs by self-assembly.

Multilayered samples repeat the double cap dot growth sequence and are then capped with 50 nm of 1.15Q and 90 nm of InP. The whole process is done at (520°C) and results in a structure roughly 300 nm (see figure 3.3) thick. Often a copy of the QD layers is grown on top of the whole structure to allow surface SEM or AFM imaging of the dots. As the last layer of these dots isn't capped, the images obtained don't represent a perfect copy of the actual dots buried underneath, but still gives a good insight on QD density. Figure 3.2 shows typical QDs obtained; density is $\sim 5\ 10^{10}$ dots/cm^2 and mean dimensions are 30 nm diameter by 5 nm height. The plan view SEM (figure 3.2 (a) and (b)) shows that dots are intrinsically elongated along [$\bar{1}$10] with a shape anisotropy ratio around 1.5. Elongation also shows in the polarization PL data, as will be presented in section 3.2.

First, we need to confirm by the PL that we are indeed probing QDs. The PL spectrum of figure 3.4 shows typical single self-assembled InAs/InP QD spectrum, as

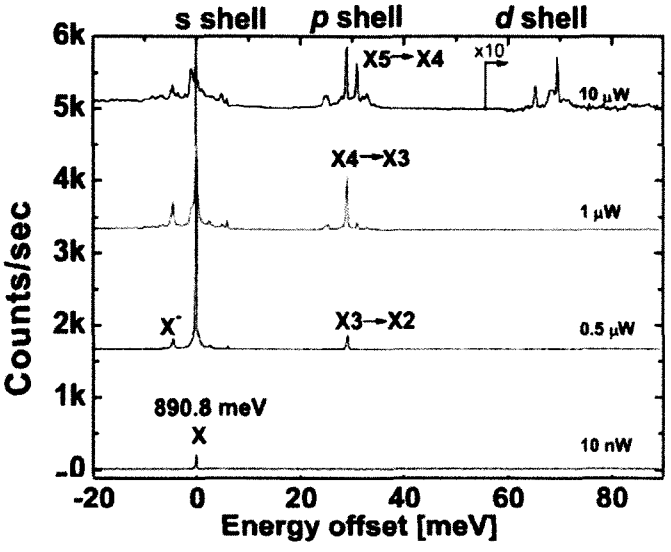

Figure 3.4: Evidence of state filling for a single InAs/InP QD as excitation power is increased. p, d, f shells appear at higher energies [64]. Reproduced by permission of Wiley-VCH Verlag GmbH & Co. KGaA.

by changing excitation power the s shell expands to include a p and d shell emission, like expected from an artificial atom [64]. PL lines are resolution limited, as expected from the discrete nature of the DOS. However, as we deal with ensembles of dots with dot height, aspect ratio, composition and strain distributions, energy levels of each QD are different due to IB and the collective emission results into a gaussian emission for each of the QD energy levels. Here the single QD PL isn't representative of the QD ensembles probed in this thesis. The single dot spectrum is shown because the GS and ES emission from an ensemble of QDs overlaps in the spectrum, making the discrete shells of individual dots hard to see. As mentioned in the theory, it is desirable to grow the narrowest size distribution of dots to keep the advantages of 0D systems.

Effect of rapid thermal annealing

Rapid thermal annealing (RTA) can be performed on the samples to modify the IB, by correcting dislocations, defects, varying the compositional and shape profile of the dots. When the thermal energy provided by the RTA is higher than the activation energy of the defect diffusion, this baking of the samples results in a change of the energy level separation, shifts the emission of the dots and can also reduce the IB of the dots [65, 66, 67]. Previously, cross sectional TEM of annealed samples processed by Carolyne Dion [68] showed (see figure 3.5 (b)) that the shape is modified by the RTA, changing the QD side aspect ratio (note that the dot shown isn't the same for the two temperatures). Therefore, the RTA affects the wavefunction shape, hopefully modifying the polarization

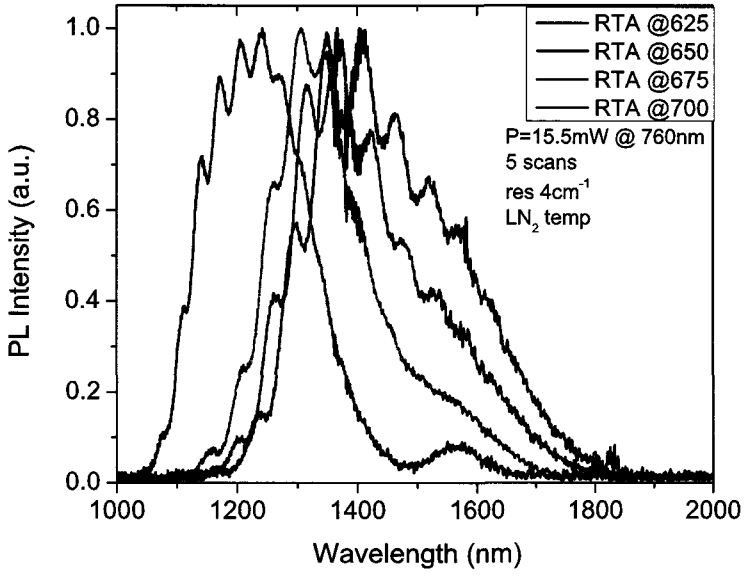

(a) PL of intermixed samples at liquid nitrogen temperature

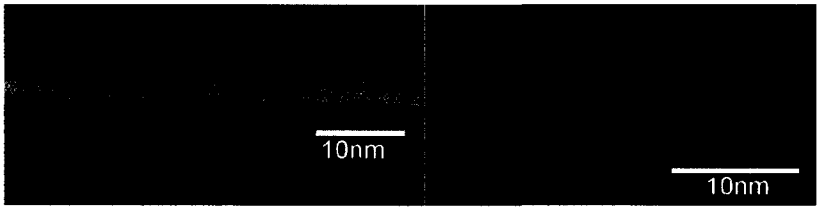

(b) Effect of annealing on dot shape

Figure 3.5: Effect of intermixing on (a) PL; as RTA temperature is increased peaks move to higher energies (b) QD geometry; TEM of as-grown dot (left) and after annealing (right)

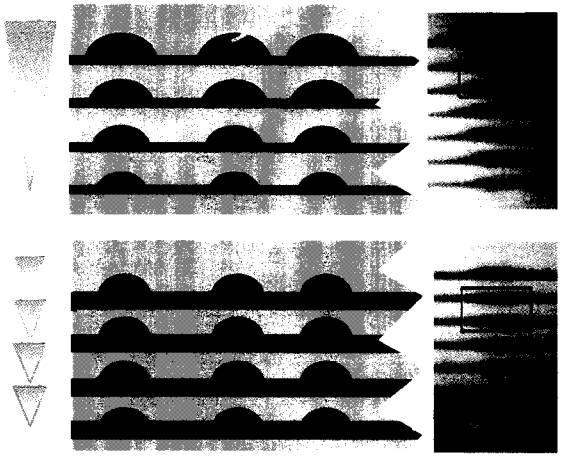

Figure 3.6: Representation of strain accumulation in a QD stack. Top : the strain accumulates from layer to layer, leading to growth of bigger dots. Bottom : the underlayer of GaP (green) compensates the compressive strain so that dot dimensions formed are similar. TEM pictures from [71] show the enlargement of quantum dots in a stack and the effect of the indium flush technique on enlargement of QDs. Reproduced by permission of Elsevier.

properties and could thus provide an easy processing technique to tune the polarization. RTAs were performed on single layers of InAs/InP QDs with grown-in defects in the InP capping layer which was intentionally grown at a temperature lower than the optimal growth temperature to produce a high concentration of native defects [68]. RTA on that high number of defects enhances the diffusion processes during RTA and increases the intermixing. For the RTA experiment, an A.G. Associates Heatpulse 410 RTA oven was used to anneal a series of four samples at different temperatures ranging from 625 to 700°C. Each sample went through five anneal cycles of 60s for a total anneal time of 300s. Then, PL measurements were taken at the end of each cycle to probe the interdiffusion dynamics. Figure 3.5 shows the effect of the RTA procedure on the PL after the 300s anneal time. The multi-peaked nature of the PL corresponds to the superposition of the GS emission from different sub-sets of QDs of same thickness, which are referred as QD families [69]. As the annealing temperature is increased, the PL blueshift accentuates due to interdiffusion of group-V atoms As and P across the QD/barrier interface, releasing the strain in the structure and forming alloys of InAsP in the dots [68, 70]. The change of composition results in the increase of the bandgap as compared with the natural bandgap of InAs, corresponding to a blueshift of the emission. In section 3.2.3 the effect of QD structural, strain and composition changes on the polarization PL will be monitored.

Photoluminescence of stack

Lasing effect can be achieved by the use of a single layer of dots [72], but usually requires high dot density to get enough gain for laser emission. As we seek QD lasers with

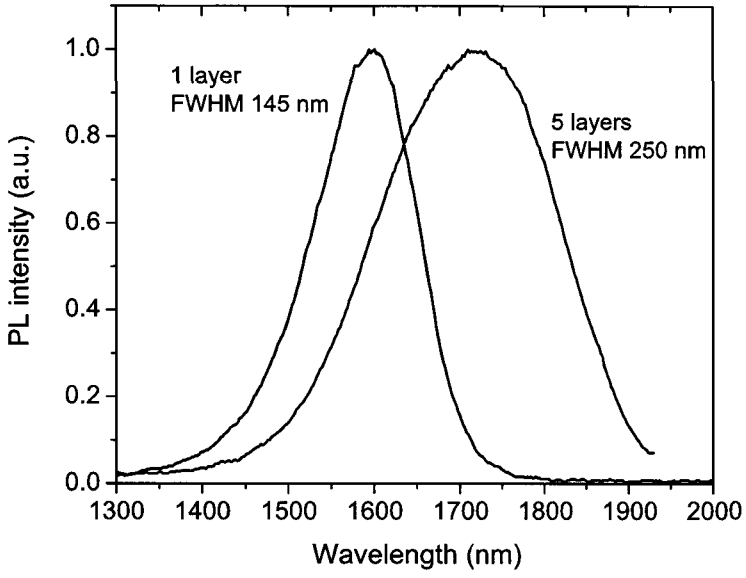

Figure 3.7: Effect of the number of layers on PL width

performances comparable to QWs, stacked structures are used to get very high gain. The self-assembly growth of QDs results in a random seeding of QD growth on a single layer, but an interesting phenomena happens as the layers are stacked on top of each other. The strain field surrounding the dots produced by the lattice mismatch between the dot and the capping quaternary propagates through the layers, leading to vertical alignment of the dots throughout the sample layers. The global accumulation of strain into the stack can, above a certain dot thickness, leads to the creation of dislocations and point defects, which lower dot strain energy [70, 73]. Most importantly, the strain propagation provides preferential seeding sites for QDs and results in a faster shift from wetting layer (FvdM) to QD (SK) growth mode so formed QDs tend to grow bigger with a lower density on each successive layer [70, 74]. Because of this, the cross-sectional TEM picture of figure 3.2 (c) shows the truncated lens shaped dots aligned in the vertical direction and the TEM picture in figure 3.6 shows that dots are indeed getting bigger as layers are added. PL-wise, strain propagation through the layers translates into a larger IB and larger PL FWHM, counteracting the higher gain provided by the higher number of dots contributing to emission [71]. This effect is confirmed by the PL represented in figure 3.7. FWHM of the stacked layers is almost doubled and emission is redshifted in the structure containing five layers. Widening of the emission translates into a drop of peak gain and therefore loss of performance in the laser structure. In order to solve

this problem, a binary underlayer was inserted under each layer to reduce the strain propagation along the vertical direction.

3.1.3 Insertion of GaP underlayer

Acting as a tensile strain layer, the binary compound GaP used as an underlayer has been shown to compensate the accumulated compressive strain in a stack and provides a smooth surface for dot formation due to suppression of As/P exchange processes [74, 75, 76, 77, 70]. This results in the suppression of size expansion of dots throughout the layers as can be seen in the TEM pictures taken by Wasilewski et al. [71] (see figure 3.6). This causes the blueshifting of the PL as the QDs grown in the stack are smaller. At room temperature, figure 3.8 shows that the insertion of GaP in the QD stack structure reduced the FWHM from 250 (5 layers without GaP) to 160 nm (8 layers with GaP underlayer), a value much closer to the FWHM of a single layer, 145 nm. This drop is even bigger in the case of measurements taken at 6K, confirming that inhomogeneous size broadening is suppressed. Furthermore, emission of the sample with the strain compensating layer is blueshifted due to reduction of the As/P exchange, which can lead to formation of alloys [78, 79]. It has also been suggested that group V and III interdiffusion reduces the strain (hence the lattice parameter) in the QDs, blueshifting the luminescence [70]. Moreover, the insertion of the GaP tensile underlayer reduces the overall compressive strain, blueshifting the emission of the QD stack. Thus, with the suppression of IB, the introduction of GaP allows the growth of a high gain stacked structure for laser devices. In the next section, we will see that the QD stacking period modification could be used to achieve polarization independent devices.

3.2 Polarization-photoluminescence of QDs

Polarization independent devices are of critical importance in fiber-based telecommunications to avoid signal distortion during amplification of signal. Using strain bandgap engineering of QWs operating in the 1.3 μm and 1.5 μm range, it was shown that the heavy-hole (HH) and light-hole (LH) characters of QW hole states can be balanced to reach polarization independent devices, such as QW SOAs [80, 81]. However, as self-assembled QDs are based on strain driven growth, the same kind of strain bandgap engineering cannot directly be applied to QDs. For instance, tensile strain is used in

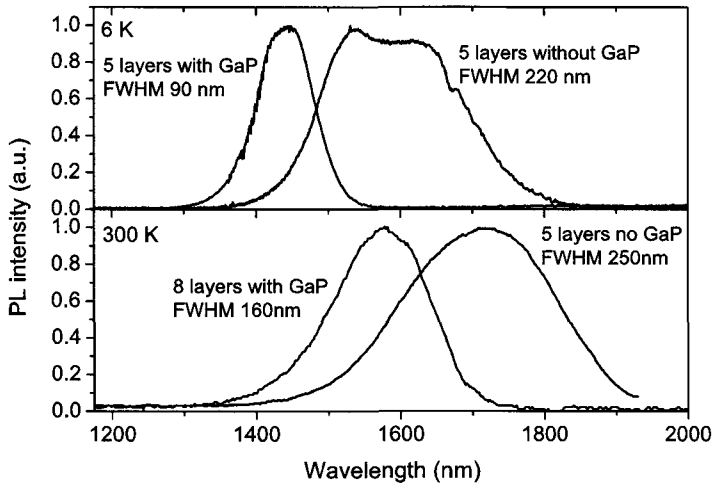

Figure 3.8: Effect of GaP insertion on the PL of a QD stack. FWHM is divided by 2.5 by insertion of GaP for PL at 6K and the same effect can be seen at room temperature.

QW amplifiers [82] to reach polarization independence, a technique which would be difficult to transfer to the growth of QDs in a stacked structure. This is the main reason demonstration of polarization insensitive QD devices, such as lasers, VCSELS and SOAs is still a challenge. Furthermore, as laser ridge devices provide edge emission, truncated dot lenses have a flattened shape with a very high degree of anisotropy (4 nm of thickness by 30 nm of diameter) [62], resulting in an intrinsically high DOP. A few alternative methods have been suggested to obtain polarization insensitive InAs/InP QD devices, such as vertical cavity surface emitting lasers (VCSELs) [83, 84], composition modulated capping layers [85] and tuning of the number of QD layers in the stacks, allowing vertical coupling of the dots so that the electron wavefunction can achieve a more symmetrical shape [86, 87]. $8k \cdot p$ calculations [48, 59] for pyramidal shaped InAs/GaAs have already predicted that a low dot period can modify the polarization properties of the QDs, as the reduction of biaxial strain brings the LH closer to the HH band and can increase the LH contribution from 5% for a single dot to 20-30%.

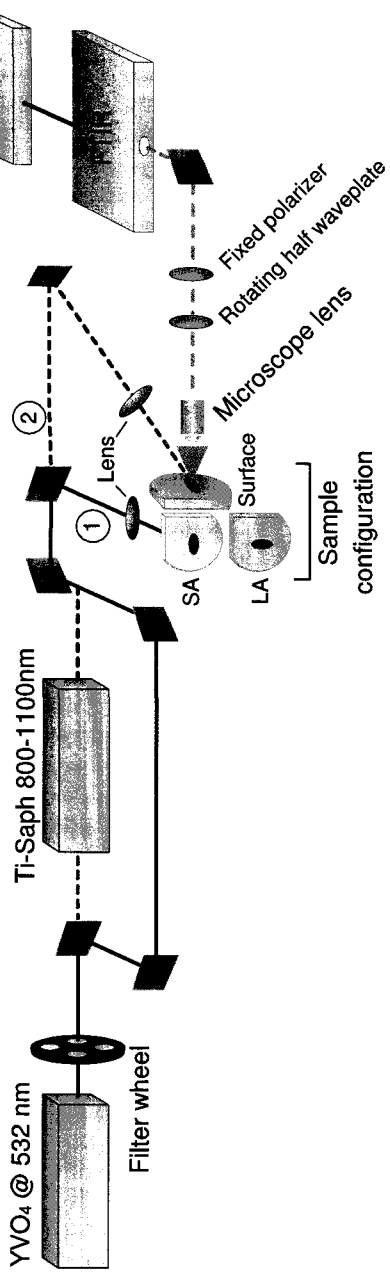

Figure 3.9: Experimental setup for Pol-PL measurements

3.2.1 Polarization-photoluminescence setup

To account for QD anisotropy as revealed by the TEM surface pictures (figure 3.2), planar and edge detection geometries were used. This provided information on the effect of dot anisotropy and interdot coupling on the QD wavefunction shape. Planar propagation measurements are classified into two categories : photons emitted perpendicular to the short axis (SA) or to the long axis (LA) of the QDs (see inset of figure 3.10). The other conventional case is surface propagation where photons are emitted normal to the sample surface. All the measurements for the Pol-PL study were carried at room temperature as the samples are intended for future ridge lasers. Figure 3.9 shows how all the different geometries are achieved in the experimental setup. First, path 1 is used for SA edge emission study with the sample configuration represented on the left. LA configuration is achieved by rotating the sample. For surface emission study, the excitation path is changed to path 2 and sample was rotated according to the right hand side of the sample configuration shown in (see figure 3.9). The emitted light was collected and collimated using a microscope objective and a standard plano-convex lens for planar and surface propagation respectively. The captured light was analyzed with a half-waveplate in front of a fixed polarizer and the transmitted signal was fed to the input port of a Bruker V80 FTIR spectrometer with a CaF2 beamsplitter and an extended InGaAs detector.

Contrarily to the PL setup, this setup uses a different exciting and collecting lens so signal collection is much more difficult. To solve this problem, an He-Ne laser was inserted into the detection axis of the FTIR by adjusting the He-Ne laser path through a set of pinholes and sent up stream to the sample surface so that the detection axis could be reproduced. That spot could then be aligned with the excitation spot for optimal signal collection. The 20X microscope lens with a numerical aperture of N.A.=0.4 used for detection had to be carefully placed, as two sample regions emitted light from the edge of the sample. One very bright emission spot located near the surface of the sample is associated with direct emission from the dots and the other weaker spot lies deeper in the sample. As the latter region shows no polarization dependence, it is linked with signal coming from total internal reflection in the sample, during which polarization information is lost. The microscope lens position was then placed to get the maximal signal from the upper emission spot. Moreover, this setup configuration is used as insertion of a beam splitter into the detection axis of the FTIR is avoided, which would modify the collected

polarization. For both top and edge Pol-PL measurements, the top excitation was chosen to inject carriers into the biggest number of dots possible. To get information on the polarization of emitted photons, a half-waveplate is rotated in front of a fixed polarizer, which eliminates detector's dependence on polarization. Excitation is kept low such that only ground state emission is collected. Ground state peak maximal intensity is then recorded for half-waveplate angle between 0 and 180 degrees to make polar plots. Then the DOP, as defined in the theory section 2.5

$$DOP = \frac{I_{max} - I_{min}}{I_{max} + I_{min}} \tag{3.1}$$

was extracted from the polar plots.

3.2.2 Effect of stack period

Samples

All samples used for stacking period study consist of a stack of four InAs QD layers as described in section 3.1.2, but without a p-n junction and any kind of nanofabrication. Each QD layer includes a GaP underlayer (1 monolayer) and a double capping technique was used. For the study of edge polarization, a series of four samples were grown with dot periodicity of 30 nm, 17 nm, 9.1 nm and 5.1 nm. PL and Pol-PL were then conducted on the samples to measure the effect of periodicity on the polarization.

Results

First the standard PL was investigated for the different geometries. Figure 3.10 shows the GS spectrum of the multilayer samples as obtained without polarization analysis for (a) edge emission and (b) surface emission. Note again that carriers are injected non-resonantly in the QDs, as the excitation energy is higher than the QD emission energy. Due to numerous relaxation events taking place between the carrier excitation and the emission, the polarization information related to the excitation source is lost. Therefore, the results presented are independent of the $Nd : YVO_4$ vertical polarization state. Only the edge emission spectra for SA emission is shown in (a) as the emission spectra for the LA and SA geometry are the same once normalized. All samples show peak emission around 1550 nm with some variations within growth reproducibility. The main difference between the samples is the wider linewidth for the 5.1 nm period sample. This can be

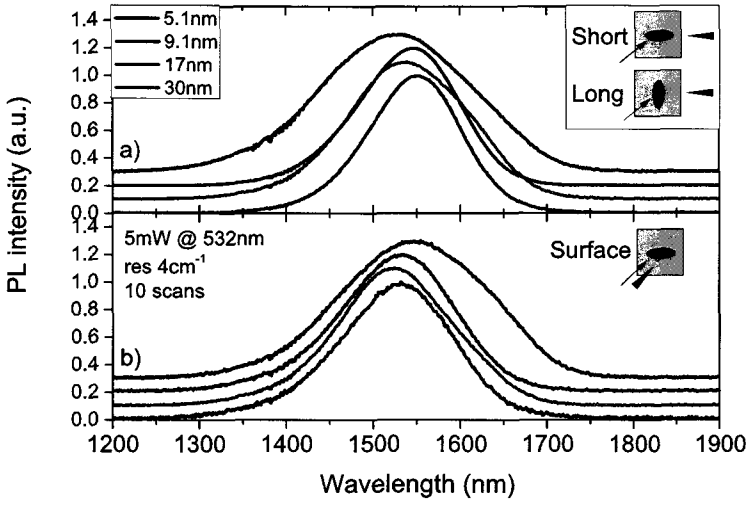

Figure 3.10: Short axis (SA) edge emission (a) and surface emission (b) spectra for different stacking periods. LA emission is the same as SA. Inset : Excitation and detection configuration, arrows representing impinging laser and red cones the emitted light. A low excitation power is used so that emission is kept in the GS.

explained either by the QDs progressive enlargement from one layer to the next due to strain propagation and by coupling between the electronic states of adjacent QD layers. This ambiguity supports the need for polarization measurements, sensitive to coupling, QD shape and strain distribution.

The result for the Pol-PL study with varying stack period is shown in figure 3.11. In (a), the SA geometry is shown, where 0 degrees (90 degrees) designate light polarization along the short axis (growth axis) of the QDs. As the layers are brought closer, SA DOP decreases from 80% to 40%. Neglecting changes in LH-HH mixing, the DOP is representative of the wavefunction symmetry, where elongation of the wavefunction in one direction will result in a bigger dipole strength so that photons are preferably polarized in the elongation direction. This assumption can be justified by the $8k \cdot p$ calculations on InAs/GaAs QDs, which have already proven that the LH-HH wavefunction proportion changes mostly for dot periods below 5 nm, so for the 30 nm to 5 nm period range the HH-LH splitting remains high [48]. For the samples under study, even in the SA geometry the aspect ratio (QD width/thickness) is very high (~25 nm/~4 nm), hence the almost perfect TE polarization of the uncoupled layers (single layer and 30 nm period). A significant decrease in the DOP is obtained mainly for the 5.1 nm period sample, suggesting that electronic coupling causes the wavefunction to become more symmetric. Furthermore, the theoretical model introduced in section 2.5 suggests that the decrease of SA DOP is related to an enhanced LH behavior for smaller interdot periods. One might expect the same argument to apply for the LA measurement geometry, however

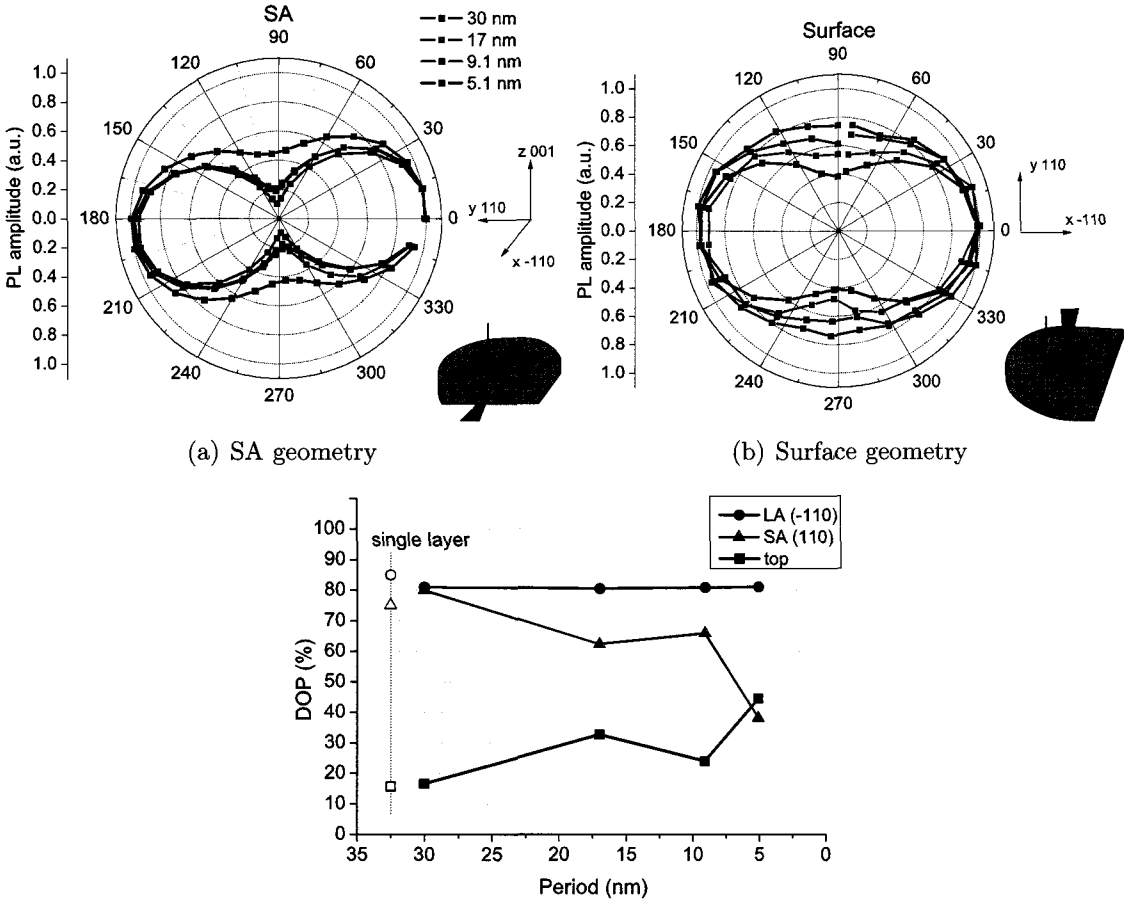

(a) SA geometry

(b) Surface geometry

(c) Summary of the change in DOP

Figure 3.11: Polarization PL polar plots of the GS emission for different measurement geometries. (c) Summary of the change in DOP as a function of interlayer separation.

no change in DOP was observed in that case (figure 3.11(c)). This discards the hypothesis of an increased LH behavior, as the LA and SA geometries would be affected in the same way. Insight on that unexpected behavior is revealed by the polarization dependence of the surface emission, shown in figure 3.11(b). Results show that QDs are anisotropic, elongated along [$\bar{1}$10] with an aspect ratio of ~1.5 [88] and that layer period reduction results in an increase of surface DOP, from 15% to 40%. This is also corroborated by our basic theoretical model, which predicts that most of the in-plane polarization anisotropy is caused by elongation of the QD. Intrinsic elongation of SA QDs is a well known phenomena and was observed on the SEM pictures (figure 3.2) [69]. As was discussed in the polarization PL section 2.5, increase in surface DOP suggests an effective QD in-plane wavefunction elongation as interlayer distance reduces, from aspect ratio ~1.5 to ~2 [88]. Therefore, in the LA geometry, the decrease in wavefunction aspect ratio due to vertical coupling as the stacking period is reduced is counteracted by an effective elongation of the QDs, thus resulting in an unchanged LA DOP. DOP results for LA, SA and surface geometry are summarized in figure 3.11 (c), where open symbols representing single layer measurements are shown for comparison.

The above results highlight the importance of obtaining cylindrically symmetric QDs, as the shape anisotropy is detrimental to both planar and surface propagating devices. For surface propagating devices, such as VCSELs, it is obvious that symmetrical QDs (parameter $\alpha = 1$) would remove the polarization dependence. For planar devices, the difficulties are highlighted if one considers the example of a ridge QD laser. Best coupling to the ridge modes is achieved by aligning the ridge perpendicular to the elongation of the QDs (LA geometry), in our case in the [110] direction. However, to achieve polarization insensitivity in ridge QD lasers or SOAs, one would have to use the SA geometry. This was shown to lead to a loss in the TE mode oscillator strength and therefore loss in device performance [89].

To solve the QD asymmetry, we remark that formation of terraces on miscut substrates of GaAs have already proven higher dot density growth and smaller dot size distribution due to the suppression of adatom diffusion between dots separated by the terraces [90, 91]. We apply this strategy to our QDs grown on InP, where a replica of the four QD layer sample with a stacking period of 17 nm was grown on a 2 degree miscut substrate. Comparison of the polarization dependence of the surface emission for both

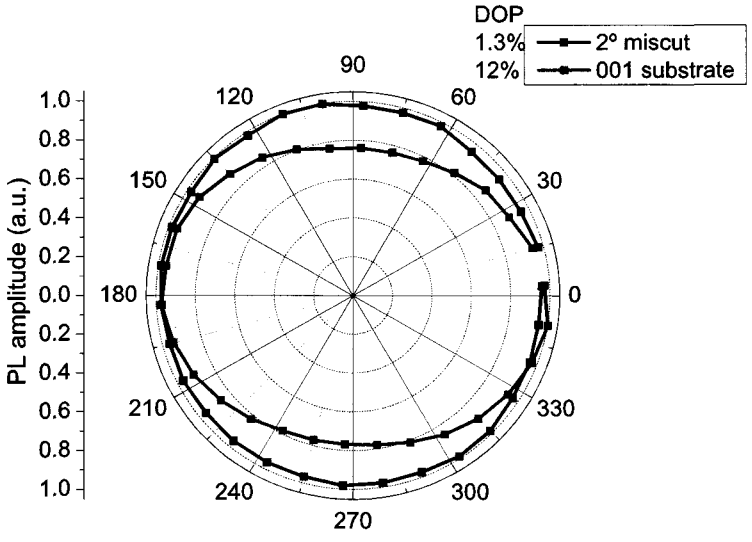

Figure 3.12: Change in top DOP from 12% to 1% with the use of a 2 degree miscut substrate for QD stack growth.

samples is shown in figure 3.12. An almost isotropic polarization emission is achieved, as the DOP was reduced from 10% for the (001) substrate to almost 0% for the miscut substrate, indicating that terraces eliminate the natural elongation of QDs along [$\bar{1}$10]. According to the simple model introduced in section 2.5, the dots formed are isotropic with anisotropy ratio $\alpha = 1$ and the neglected mixing term in the theory is pretty small, as the DOP is very close to 0%. The suppression of the in-plane elongation, which was detrimental to the control of the polarization properties in the planar geometry, could result in a change of DOP for the LA geometry as well. The use of a miscut substrate could then allow close stacking of layers in a ridge laser without any performance degradation. Moreover, in-plane isotropic QDs are very desirable for VCSELs, but these suffer from lower gain pass compared to side emitting QD lasers.

Although complete isotropic polarization for planar propagation devices isn't achieved, further reducing the stacking period, increasing the number of layers or intermixing of the stacked structure should lead to further improvements. By careful control of these techniques, one could achieve polarization insensitivity for both planar and surface propagating QD devices emitting in the telecommunication wavelength range.

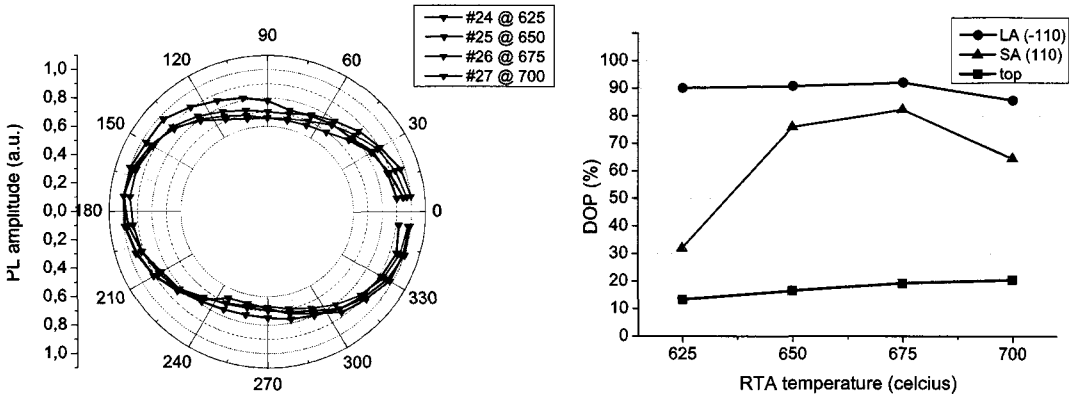

(a) Polarization dependence for surface geometry (b) Summary of DOP change for surface, SA and LA

Figure 3.13: Annealing temperature effect on (a) surface polarization (b) all detection configurations for a single QD layer.

3.2.3 Effect of rapid thermal annealing on polarization

Interdiffusion was already used to fine tune achieve the LH HH band merging (degenerate LH HH bands) in tensile strained QWs [92]. For non-tensile strained QWs, the interdiffusion of group V species has been shown to induce tensile strain in InGaAs/InP [93] multilayered QW lasers for the 1.55 μm range, thus providing an easy way to achieve polarization independence. Thus, relief of strain in QDs could result in a lower splitting between the LH and HH bands, thereby reducing the polarization dependence of the device. With this in mind, we studied the polarization properties of annealed single layer QD samples introduced in section 3.1.2. Surface DOP taken as a function of RTA temperature as shown in figure 3.13 (a) grows from 13 to 20%, which could be related to a slight dot elongation. Edge Pol-PL was also carried by collecting the intensities for the TE (TM) modes to quantify the effect of annealing temperature on the DOP. Collected edge signal was very weak due to experiment configuration and low gain provided by the single QD layer samples. Furthermore, PL intensity decreased with increasing annealing temperature due to increasing number of non-radiative recombinations. Figure 3.13 (b) summarizes the results for all the detection geometries. For LA geometry, RTA temperature has very little effect on DOP, but SA DOP follows a steep increase from 30 to 80% roughly. This result is quite unexpected, as a single layer of QDs has a DOP around 80%, as presented for single layer measurements in figure 3.11 (c). Because of

this discrepancy, underlying processes for the increase in surface DOP aren't understood and inconclusive, in major part because a very low signal collected at room temperature. However, use of annealing on stacks of quantum dots instead of single layers could lead to enhanced signal and would probably modify further the results. It has been demonstrated that high temperature annealing on a threefold stack of InP dots in GaInP [94] resulted in merging of dots in the vertical direction. This would result in lower edge shape anisotropy ratio and therefore lower DOP of stacks.

We have proposed a few alternatives to strain engineering of QDs, namely the use of a high number of closely stacked layers and intermixing in a stacked structure to achieve polarization independence of QD SOAs. In the next chapter, we investigate the improvement of telecommunication lasers performances caused by the insertion of the GaP strain compensating underlayer.

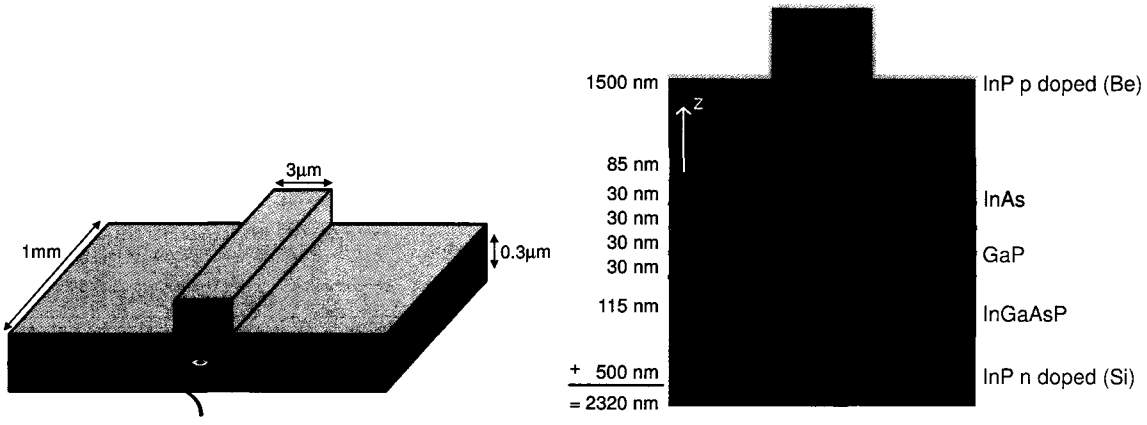

(a) Ridge mode in the laser structure

(b) Laser structure dimensions

Figure 3.14: (a) Elongated TE shape of the laser mode and confinement of the laser mode as it feels the interface between air and ridge. (b) Core dimensions the four layered stack with period 30 nm. Total core thickness is $\approx$ 310 nm and laser structure is $\approx$ 2.3 μm (not to scale).

3.3 Laser performances

In section 3.1.3 stacks of QDs were optimized to provide very high gain for a laser structure. In this section, we use the advantages of QDs as stated in chapter 1 to make a 1.55 μm QD telecommunications laser superior to its QW equivalent laser, showing reduced threshold current, higher efficiency and larger bandwidth. Thus, this section provides an analysis of the QD lasers performances by introducing quantities derived in the book by Coldren and Corzine [95] and summarized in the application notes of Newport [96]. The most important milestone in QD laser development presented here is the insertion of a GaP underlayer, which was shown in section 3.1.3 to greatly reduce the FWHM of the PL stack. As shown below, the insertion of the binary layer results into a higher gain structure, translating into a significantly lower threshold current and enhanced efficiency. This section closes the gap between the core QD stack properties as revealed by PL and the actual improvement of the laser devices.

3.3.1 Laser structure for semiconductor lasers

The PL presented in section 3.1.2 originates from spontaneous emission, photons emitted randomly in space and time without phase coherence. On the other hand, in a laser photons preserve phase coherence because they originate from stimulated emission. A

laser is made of two main components : a gain medium (a QD stack in this case) and a resonant cavity. The gain medium must be able to sustain steady-state, meaning that the number of injected carriers must be equal to or exceed the number of emitted photons ($\frac{dN}{dt} \geq 0$) to provide continuous operation of the laser. The resonant cavity confines some of the emitted photons (as the as-cleaved cavity mirrors are 30% reflective) so they can stimulate emission of other photons, preserving their phase coherence and resulting into the amplification of light in an avalanche like process.

In section 3.1, carriers were injected into the QDs optically for PL. This way of pumping carriers isn't very handy as it requires roomy lasers when compared to most electronic components. To create very compact lasers, carriers are injected in semiconductor lasers by the p-n junction, made by doping the InP capping layers of the previously introduced structure. By applying a bias voltage on the junction, the number of carriers injected into the dots can be changed, effectively tuning the number of excitonic recombinations contributing to emission. The resulting signal from the laser is called electroluminescence (EL) in contrast to photoluminescence. The edge representation of the structure formed is presented in figure 3.14 (b). The resonant cavity confines the photons in the plane and growth direction of the dots : in the plane, the interface between the InGaAsP waveguiding core and the air acts as effective mirrors with a $\approx$30% reflectivity. In the vertical direction, light guiding is achieved by the interface between InGaAsP and InP. A higher reflectivity coating (R$\simeq$ 90%) can be applied on the facets of the laser to achieve bigger light confinement, lowering the threshold current, but all the results presented here are as-cleaved samples for fabrication simplicity. The planar confinement provided by the laser facets and waveguiding core creates a broad area laser sustaining multiple laser modes, but for most of the applications single mode operation is needed for low laser beam dispersion. To achieve single mode operation, additional confinement in the lateral direction is provided by a waveguide etched on the top of the structure. The ridge created confines light, as the tail of the waveguiding mode feels the difference of index of refraction between the ridge and air, reflecting the mode back in the cavity.

Figure 3.15 shows the actual ridge laser devices from (a) top and (b) side. The electrical contacts are formed by Ti/Pt/Au layers of 25 nm / 55 nm / 1000 nm respectively in order to allow electrical injection from the p side of the structure. The thin vertical lines in (a) are the ridges of each laser and are linked to contact pads for easy electrode

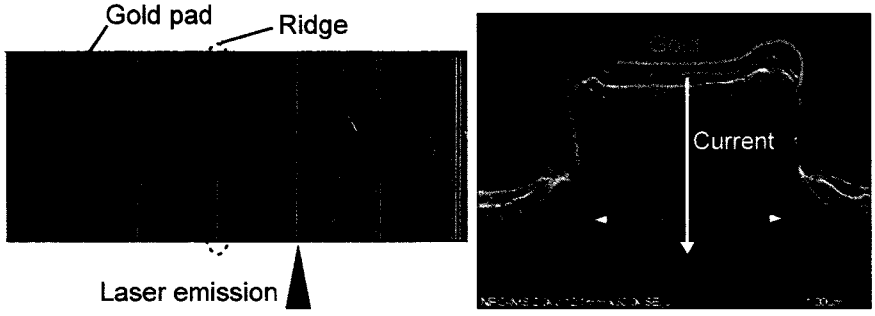

(a) View of actual devices from top. Ridge is 1mm x 3μm.

(b) SEM of waveguiding ridge

Figure 3.15: Top and side view of a QD ridge laser

contact. Current injected into the device comes only from the top of the ridge, the other surfaces being covered with a thin layer of oxide, hence QDs contributing to lasing are directly under the ridge (neglecting current spreading). The size of the opening in the oxide, changing from one device to the other can, to some extent, change the density of carriers injected and impact the threshold current of the laser device.

Early in the development of QD lasers, gain saturation was a great concern due to the limited DOS provided by QDs as compared to QW, which have a continuum of states available. The problem is that if the gain provided by the completely filled QDs is lower than the losses of the laser, lasing is impossible ! The QD gain is expressed as

$$G_{QD} = G^{sat}\frac{J_{QD} - J_0}{J_0} \tag{3.2}$$

where the saturated gain G^{sat} can be expressed in function of the IB, $G^{sat} = \text{const}\ n_{QD}/\Delta$, Δ being the energy width of the density of states (also a measure of the size distribution) and n_{QD} is the density of QD [97]. G^{sat} can be pictured as a maximum boundary on the QD gain, G_{QD}. J_0, the transparency current, is a measure of the quality of the semiconductor material used and represents the threshold current density for an infinitely long device without mirrors losses.

In a completely filled GS QD ensemble, each QD is constantly filled by two electrons in the GS, so that $J_{QD} = 2J_0$. In that case, $G^{QD} = G^{sat}$ and the gain is saturated. If G^{sat} is lower than the losses of the laser, then lasing cannot occur. One can see that in order

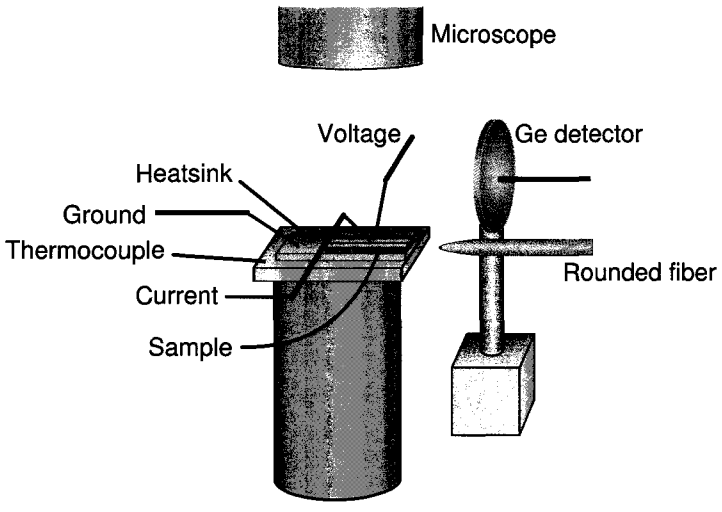

Figure 3.16: Setup for LIV and spectral measurements

to avoid gain saturation, the density of QDs n_{QD} (DOS energy width) has to be as big (small) as possible. Use of stacks in laser structures is an easy way to achieve high QD densities, but the QDs must have minimal broadening, as discussed in section 3.1.2. The insertion of GaP allowed us to achieve high dot densities while keeping the broadening to a lower value so that gain saturation is of little concern in results presented below. Even with the underlayer, residual strain propagating through the stack causes the IB to grow with the number of QD layers in the stacks. In our case, 4 layers provided optimal laser performance.

3.3.2 Lasers setup

An important figure of merit of a laser is its threshold current (I_{th}), the current at which the lasing is achieved. Most semiconductor lasers are based on layer stacks of have different ridge lengths/widths, so the threshold current density $J_{th} = \frac{I_{th}}{N\,A}$ is presented here to ease the device comparison, where N is the number of layers and A the area of the ridge. Threshold current is measured by taking Power vs Current or Voltage (LIV) curves on a typical diode testing setup as represented in figure 3.16. The ridge laser is placed on a submount to allow efficient heat transfer between the laser device and the Peltier cooler, placed underneath the sample to keep its temperature at 20°C. Three probes are needed : one for current injection, one for the voltage reading and one for the ground. Electrical injection is usually done with constant current (CW), but can also

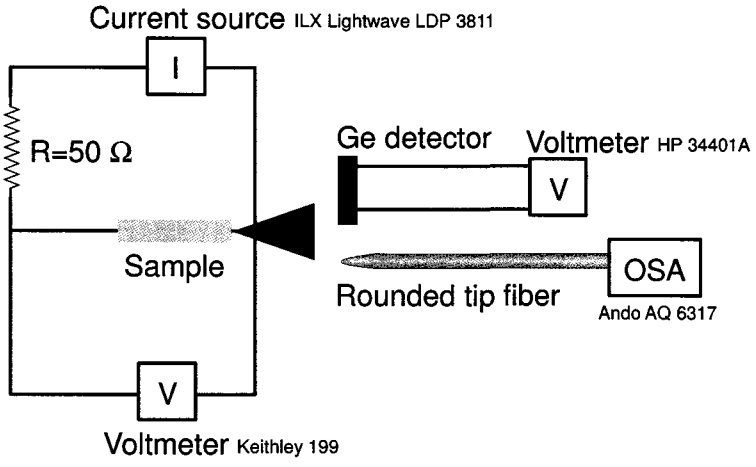

Figure 3.17: Electrical circuit for laser measurements

be done with pulsed current injection. For pulsed measurements, impedance matching between the sample and the current probe is required, so a 50 Ω resistance matching the current source impedance is introduced between the current and ground probe (see figure 3.17). To measure the power emitted, a Germanium detector hooked to a voltmeter is placed on the cleaved side to collect emitted laser light. For the spectral measurements, a rounded tip fiber was coupled to the ridge and the signal was analyzed by an OSA.

3.3.3 Ridge lasers

Initial QD laser

To compare adequately our QD laser with commercial QW lasers used in telecomm, a five staked InGaAsP QW (06-069) reference laser was grown at NRC in 2006 for reference. The performances of the QW laser are $J_{th} = 200A/cm^2$ and an external efficiency of $\eta_d = 28\%$ for a 3 μm wide x 1 mm long device. For the QD laser (06-070), the structure was exactly the same as 06-069 with its QWs replaced by QDs, without a GaP strain compensating underlayer (see appendix A.3). Figure 3.18 shows that the QD performances obtained are inferior, mainly due to QD inhomogeneous broadening in the stacked structure, as discussed in section 3.1.2. To solve this problem, a GaP underlayer was inserted, doping tuned and core widened to allow better confinement. This dramatically increased the performances of the QD laser structure (see figure 3.18), so that most recent QD lasers presented here have better efficiencies and threshold cur-

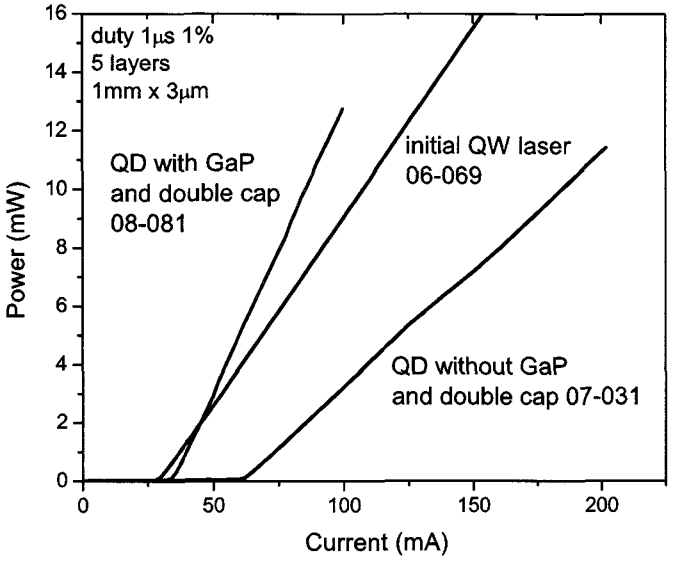

Figure 3.18: LI curves for the initial QW, QD and best QD laser

rent densities than the QW reference laser, making them extremely good candidates for telecommunication applications. Note that subsequent results will be for laser structures with GaP underlayer unless stated otherwise. A summary of laser structures used in this thesis is presented in appendix A. Shortly, the main structures are : 07-031, a five InAs/InGaAsP QD layer stack emitting at 1630 nm, 08-022 same structure as 07-031 with a GaP underlayer and double cap technique emitting at 1600 nm, 08-081 is a repeat of 08-022 with a double cap adjusted for emission at 1550 nm and 08-148 is a threefold stack with a larger waveguiding core at 1520 nm.

Power characteristics

Figure 3.19 shows the LIV curves obtained for a 3 layer stack of QDs. Note that this sample is chosen for its performance reproducibility and to show that by increasing the waveguiding core thickness and optimizing the p-n junction doping, performances similar to the 5 layer stack can be obtained. In a typical laser LI curve, power emitted is negligible before I_{th} as it comes mainly from spontaneous emission and post threshold the diode behavior is associated with stimulated emission. I_{th} is found by taking the linear fit x-intercept of the lasing part of the curve. Alternatively, it can be computed by the maximum of the curve's second derivative [95]. The slope of the linear fit also provides an important quantity, the external efficiency (η_d) of the laser. In an ideal laser,

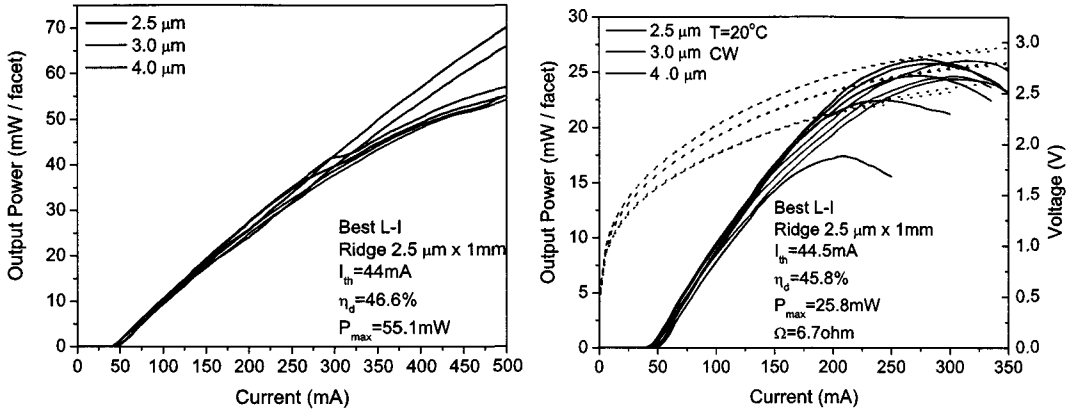

Figure 3.19: Typical LIV curves in duty cycle ($1\mu s$ 1%) (left) and CW (right) (sample 08-148). The dotted lines represent the voltage against the current.

the injection of one electron would result in the emission of one photon, yielding a 100% external efficiency. Accordingly, the slope of the LI curve can be expressed in function of the number of injected carriers and their energy [96] :

$$\frac{\Delta P}{\Delta I} = \frac{h\nu}{q} = \frac{hc}{\lambda q} \tag{3.3}$$

where q is the charge of the electrons injected and λ is the wavelength of the emitted photons. The left part of equation 3.3 is measured experimentally, representing the power of emitted photons in function of the current. Over the same time scale, the right part corresponds to the "theoretical limit", where one electron of charge q leads to the emission of one photon of energy hc/λ. The external efficiency can then be expressed as the ratio of the actual output over the "theoretical limit" as the external efficiency :

$$\eta_d = \frac{\frac{\Delta P}{\Delta I}}{\frac{hc}{\lambda q}} = \text{slope of LI curve} \cdot \frac{\lambda q}{hc} \tag{3.4}$$

C-band photons being emitted at 1.55 μm, the external efficiency is obtained by multiplying the slope of the LI curve (in A/W) by $\frac{\lambda q}{hc} \approx 2.5$.

Applying these basic concepts to the laser device, we measure in figure 3.19 (a) I_{th}=44 mA ($J_{th} = 590 A/cm^2$), 46.6% efficiency in duty cycle and 55 mW @ 500 mA maximum power emitted by a single facet for the 1 mm x 2.5 μm device. Efficiency is much higher

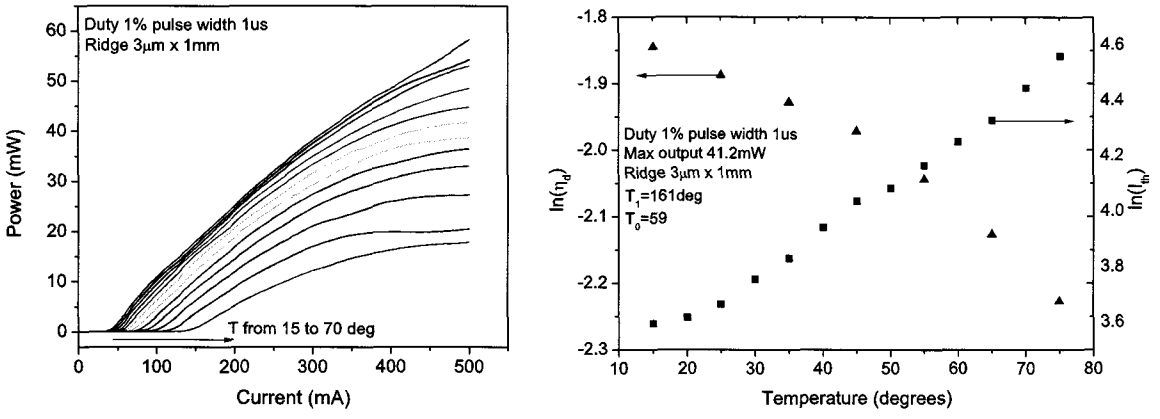

(a) Increase of threshold injection current and decrease of external efficiency caused by temperature

(b) Natural log of external efficiency (threshold current) in function of temperature of device to extract T_1 (T_0)

Figure 3.20: Temperature characteristics of QD lasers (08-148)

than the QW equivalent (46.6% vs 28%), but the threshold current is 50% higher. The high I_{th} value has been addressed in the other devices by including five layers instead of three, so higher density of states are available for emission. Still the inferior threshold current is surprising considering the theoretical predictions of section 1.1. This can be explained by the infinite QW theoretical assumption and the finite area covered by QDs in a device as compared to QW lasers. Figure 3.19 also shows that measurements done over various ridge widths achieve good reproducibility between laser bars of same dimensions. Performances in CW are quite comparable to duty cycle measurements, except for the maximum power output, which is limited to 28 mW by the 'rollover' of the LI curve related to the thermal effects. Heating of the device can be lessened by reducing the contacts resistivity through appropriate p-n junction doping. This brings us to the effects of temperature on device performance.

Temperature characteristics

Temperature affects the material properties of QDs in various ways : the bandgap energy reduces (peak wavelength increases) due to the lattice dilatation of the structure [98] and phonon interactions lead to parasitic recombinations outside of the dots as free carriers are created in the waveguiding layer of InGaAsP or in the wetting layer of the dots [99] or captured by traps [100]. Furthermore, enhanced phonon-carrier interactions increase the probability of excitation into higher energy levels or even into the waveguiding substance

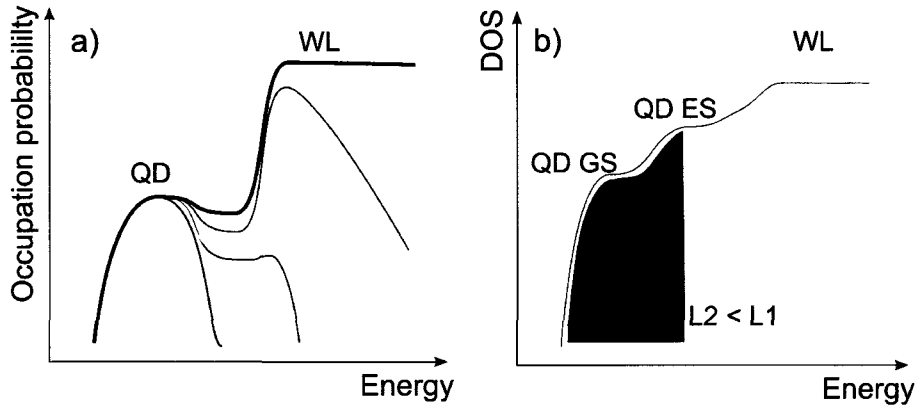

Figure 3.21: (a) Effect of temperature on DOS, blue (red) curve is the lowest (highest) temperature (b) DOS as a function of energy for an inhomogeneous distribution of dots

(see figure 3.21 (a)). This loss of carriers results in an increase of J_{th}, which is quantified by the characteristic temperature T_0. Hence, T_0 is a measure of the independence of the threshold current over the temperature, given by

$$J_{th} = J_0 e^{T/T_0} \tag{3.5}$$

$$\Rightarrow T_0 = \frac{\Delta T}{\Delta ln(J_{th})} \tag{3.6}$$

So T_0 is given by the inverse slope of $ln(J_{th})$ in function of temperature. On the other hand, temperature limits the power emitted, lowering the external efficiency. Analogous to T_0, T_1 is the dependence of the efficiency on the temperature as

$$\eta_d = \eta_{d0} e^{-T/T_1} \tag{3.7}$$

$$\Rightarrow T_1 = -\frac{\Delta T}{\Delta ln(\eta_d)} \tag{3.8}$$

Although due to the discrete DOS, the theoretical performance of QD lasers is supposed to be independent of the temperature, in the case $\Delta E \gg k_b T$, where ΔE is the shell energy spacing and $k_b T$ is the thermal energy, figure 3.20 (a) shows that higher temperatures shift the LI curves to higher currents and the rollover limits the total power output. From these measurements, the extracted temperature T_0 is 59°C (figure 3.20 (b)), which is in the range of usual characteristic temperatures for QD lasers at RT [101] and T_1 is 160°C. The discrepancy between the measured T_0 and the very high T_0 pre-

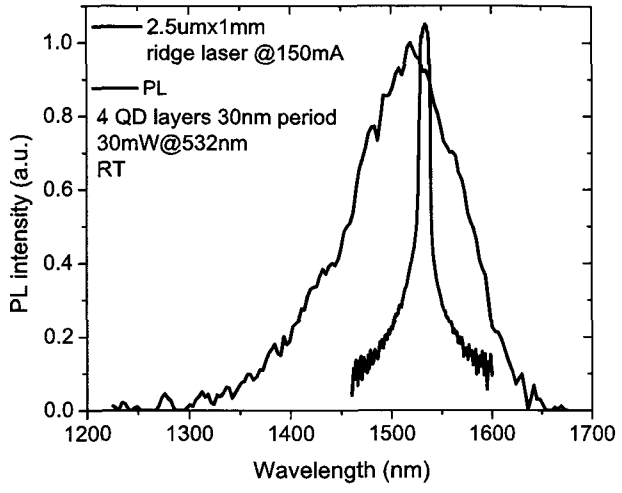

Figure 3.22: Electroluminescence of a 2.5 μm x 1 mm laser diode (08-022, in pink) compared to the edge GS PL from a four layer stack (07-094, in black). The laser emits in the GS.

dicted by theory is caused by the fact that $\Delta E \approx k_b T$ (50 meV vs 30 meV). The quest for an infinite T_0 lead to the use of other structures, namely dot in a well (DWELL), tunneling injection and quantum dashes, as will be investigated in section 3.3.4. As is expected from the discrete DOS of QDs, the FWHM does not increase with temperature, contrarily to QWs. However, the PL intensity and thus lasing power is dropped because of carrier redistribution outside of the QDs, as can be seen by PL temperature dependent measurements. In the next section, we switch from PL to electroluminescence (EL) to analyze the spectral properties of the QD laser and verify that the laser is lasing in its GS @ 1550 nm.

Spectral characteristics

As the lasers studied in this thesis are intended for the L and C bands of telecommunications, spectral analysis of the EL is essential. In order to get maximal performance, the laser diode must operate in the QD GS, as population inversion in ES is much harder to achieve. The latter statement holds if the gain provided by the GS is higher than the laser losses. Figure 3.22 confirms that the laser is lasing in the QD GS indeed. The double capping technique allows the control of the QD height very precisely, so that the QD GS emitting wavelength can be tuned. As the QD confinement in the vertical direction is much bigger than in plane, tuning of the QD height is the best way to change the QD

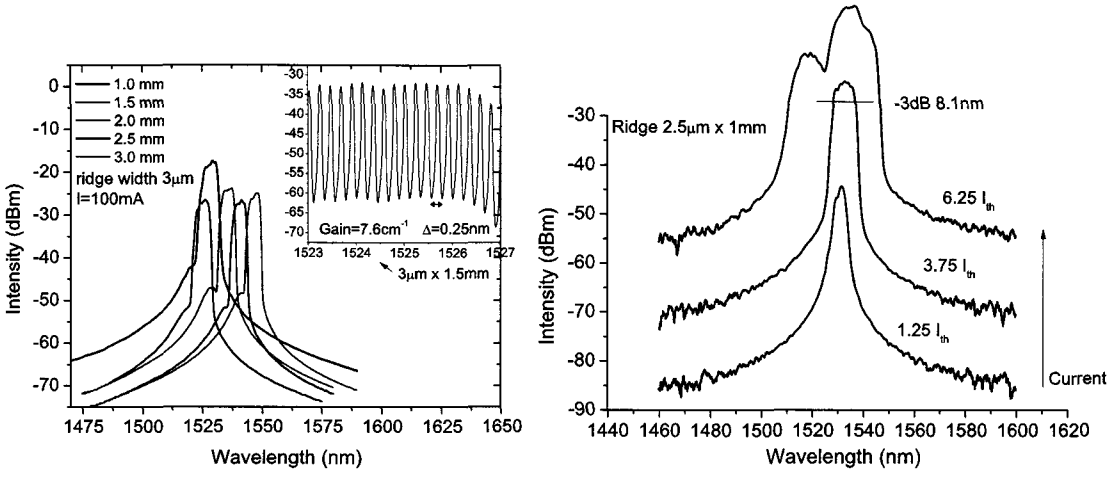

Figure 3.23: (a) Redshifting of emission with device length (08-081) and (inset) Fabry-Perot oscillations. (b) Broadening of emission with increasing injection current (08-022).

energy levels. This is shown by the dependence in $1/l_0^2$ of the 'vertical QW' energy levels in equation 2.7. In addition to growth techniques such as double capping, the length of the laser devices can be tuned to achieve emission in the telecommunications ranges. The emission can be redshifted by using a longer laser diode length, which causes a decrease in facet losses, so that the gain needed to achieve lasing is lower [102]. As shown in figure 3.21 (a), the DOS (and therefore the gain) is smaller at lower emission energies (longer wavelength) and lasing threshold is achieved at longer wavelength for longer devices.

In the optic of developing multi-wavelength lasers (MWL) applications, the number of channels emitting over a certain wavelength range has to be as high as possible. Two avenues can be considered : provide a higher bandwidth, or reduce Fabry-Perot intermode separation. The latter can be changed by increasing the laser diode length, as the spacing between the emitted Fabry-Perot modes is $\Delta\lambda = \frac{\lambda^2}{2nL} \sim 0.25\ nm$, where $\Delta\lambda$ is the intermode separation, L is the length of the device and n is the refractive index. By increasing the length, the mode spacing is reduced so the number of modes included in the emission peak increases. The other way to provide high bandwidth for MWL uses a very undesirable property of QD ensembles, inhomogeneous size broadening, often synonym of performance loss in the last sections. Figure 3.23 (b) shows that by increasing the injection current higher than I_{th}, the EL bandwidth widens because of

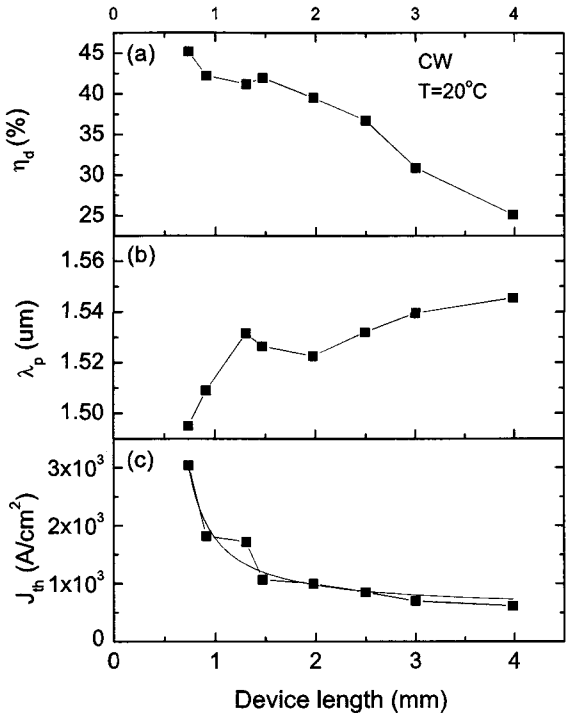

Figure 3.24: Laser characteristics in function of length of device (08-081)

increasing number of QD families with a gain higher than laser losses. This creates a dip at 1530 nm, separating the different families at higher current. By pumping the QD laser even harder, the FWHM can be increased further. These techniques have already lead to emission of over 90 channels in the C and L bands from a single device [38].

Effect of device length on performance

In a longer laser diode, the photons confined travel more distance before exiting the laser, so a lower number of photons are extracted from the device per unit time, resulting in a lower efficiency and lower threshold current density (higher threshold current). Due to lower photon device extraction in long cavities, the external efficiency drops. The relationship between η_d and the cavity length (L) is given by [96] :

$$\frac{1}{\eta_d} = \frac{1}{\eta_i}\left(1 + \frac{\alpha_i}{ln(1/R)}L\right) \tag{3.9}$$

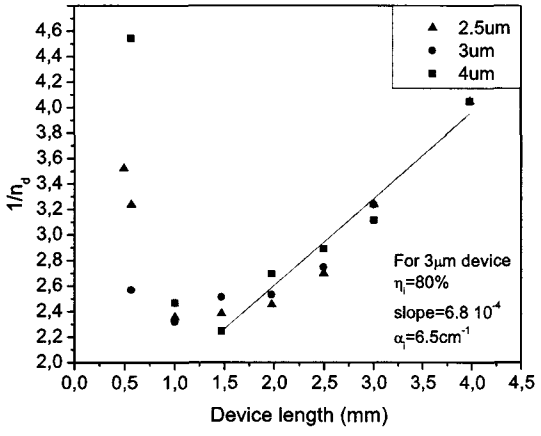

Figure 3.25: Inverse of external efficiency in function of device length to find the internal efficiency and losses of the laser (08-081).

where η_i is the internal efficiency, α_i are the internal losses and R is the reflectivity of the facets. The slope of $\frac{1}{\eta_d}$ vs L therefore gives information on the internal losses and the intercept gives the inverse value of η_i. In figure 3.24, increasing the device length results into a drop of the efficiency because of the lower photons extraction from the device per unit time. Parameters introduced in equation 3.9 will be quantified below for our device.

Other characteristics

More interestingly, cleaving several lasers at different cavity lengths and measuring $1/\eta_d$ as a function of L, one can obtain a measurement of the internal efficiency η_i and internal losses α_i as shown by equation 3.9. That study was done with the five stack laser material (08-081), which is currently among our best devices. Results are presented in figure 3.25. The data for the 0.5 mm device was neglected because of increased thermal effects which affect the slope of the LI curve, leading to a 'wrong value' of the external efficiency. For the 3 μm wide device, the internal efficiency η_i is 80% and internal losses are $\alpha_i = 6.5\ cm^{-1}$ as deducted from equation 3.9. This value is in the range of internal losses values for QW 1.55 μm lasers [103, 104, 105].

Laser polarization

The polarization properties of a stack of quantum dots was investigated in chapter 3.2 without actual insertion in a ridge structure. As the waveguiding region of the laser

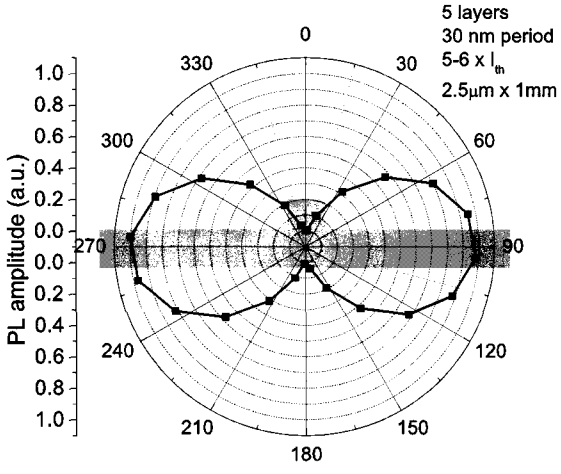

Figure 3.26: Polar plot of the polarization amplitude of a single mode ridge laser. Emission is TE polarized, aligned in the plane of the ridge laser structure drawn in gray (08-081).

structure is elongated in the plane direction, roughly 10 times wider than in the vertical direction (3 μm vs 0.4 μm) as shown in figure 3.14, the optical field from a ridge device is strongly elongated in the plane (see figure 3.26). Moreover, as most of the emission from the QDs comes from the conduction band to HH transition (considering only the ground state), the emission is strongly TE polarized, as was demonstrated in section 2.5. However, polarization independence is most important for SOAs as opposed to lasers, because the random laser polarization impinging on a SOA has to be amplified the same way to avoid signal distortion.

3.3.4 Other laser structures

Following previous measurements, a few attempts to modify the laser designs were made to improve its performances. This section is included to stress that the insertion of GaP underlayer wasn't our first attempt at improving the laser performances (I_{th}, η_d, T_0) and to show which QD laser structures were tested. First, a tunneling injection laser [106, 107] was fabricated in the hope to increase T_0. The structure is made by growing a QW, which has a higher DOS, next to the QDs to act as a carrier reservoir. Then, the QW GS is tailored to achieve tunneling resonance with the QD GS. That way, most of the injected electrons are forced to tunnel in the QDs, thereby reducing the number of recombinations occurring in the optical confinement layer. Other groups

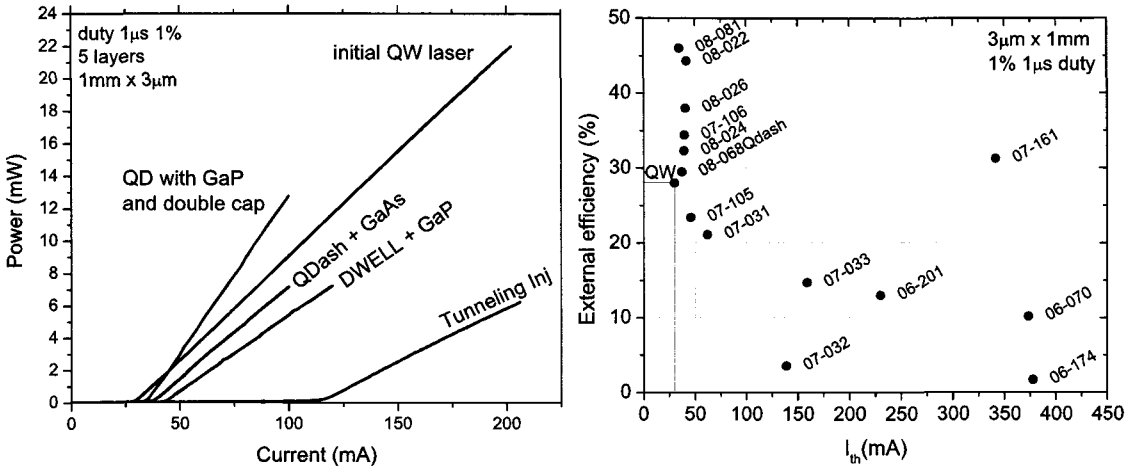

Figure 3.27: (a) Other laser structures LI curves (b) Summary of the efficiency in function of threshold current in duty cycle of QD lasers grown since 2006

have increased T_0 to 363K [108] for a InGaAs/GaAs tunneling injection laser. In our case, the threshold current and efficiency performances of our GaP underlayer sample were decreased by this technique, probably because the GS wasn't exactly lined up, so this approach was discarded. Originally used to shift the emission of InAs/GaAs QDs to 1.3 μm [109], the dot in a well (DWELL) growth technique was used to ensure fast carrier relaxation to the dots [110]. By embedding the dots in a QW, the carriers are brought closer to the dots and the high QW DOS provides a carrier reservoir for the dots. This configuration is supposed to help the constant carrier filling of the dots, but in our case the performances didn't improve. Furthermore, the DWELL technique is quite tricky as the QW changes the QD strain and growth dynamics, thereby affecting QD density and redshifting emission. Lastly, QDs were grown as dashes (high anisotropy dots $\alpha \approx 10$) [111] to provide higher carrier density of states and better laser ridge coupling, by orienting the LA of the dashes perpendicular to the ridge. The threshold current increased by 10%, but the external efficiency dropped to the QW value (28%), so finally we sticked to the 4-5 stack of QD layers with GaP underlayer.

3.3.5 Performance summary

All theses trial and errors are represented in figure 3.27 (b), showing the external efficiency in function of the threshold current for most of the produced devices since 2006, as measured in duty cycle. The first sample numbers represent the year of the sample

growth and as we get near 2009, lasers shift to the top left corner, to high η_d and low I_{th}. The latest devices have an efficiency close to 50% and a threshold current near 35 mA ($J_{th} = 230A/cm^2$), clearly an upgrade from the quantum well laser structure originally used and a very good candidate for telecommunications applications.

Chapter 4

InAs/GaAs quantum dot superluminescent diodes

In the last chapters the discrete DOS and the wide emission provided by the IB of the QDs allowed the development of high performance QD lasers for telecommunications to replace existing QW devices. The IB is undesirable for lasers as it lowers its peak gain, but in this chapter the IB is exploited in a beneficial way to provide high bandwidth incoherent light emission. The device creating such emission is called superluminescent diode (SLD) as it amplifies the *spontaneous* emission, in contrast to a laser, which amplifies the *stimulated* emission. Lack of lasing is a desirable property in this section, as the intended applications are for medical optical coherence tomography (OCT), notably skin cancer detection. The low coherence of a SLD allows non-invasive imagery of biological tissues, contrarily to X-rays [112], making the QD SLDs very attractive as OCT sources.

4.1 Optical Coherence Tomography

At its simplest form, OCT is based on a Michelson interferometer (see figure 4.1). The source signal is split into a reference signal and a probing signal. The probing signal is backreflected in the sample due to the difference of index of refraction. In the case of cancer detection, the difference of index of refraction between the tumors and the healthy tissues provide the contrast of the OCT image. Then, the reference and sample signals recombine on the way to the photodetector, where the interference can be modified by moving the reference mirror. The resulting interference patterns give information on the

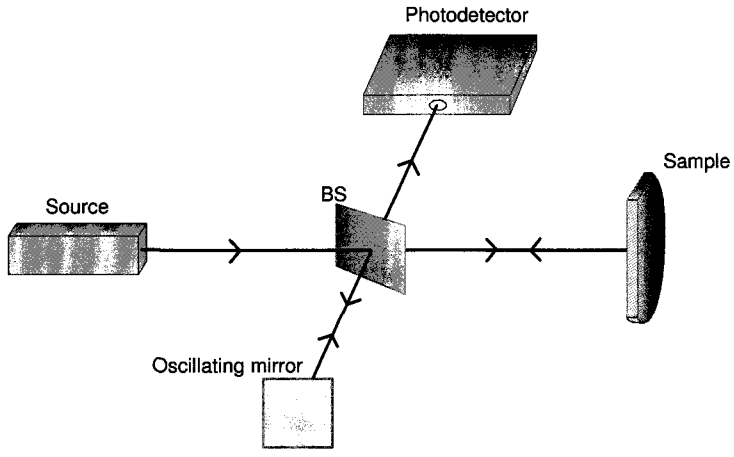

Figure 4.1: Michelson interferometer composed of an incoherent source, impinging on a beam splitter (BS), which divides the signal between the oscillating mirror (reference signal) and the sample. Both signals interfere when going to the photodetector, giving the intensity in function of the mirror displacement, which can be related to the depth of the sample.

sample's depth profile and the depth resolution of OCT is given by [113]

$$R \approx 0.44 \frac{\lambda_0^2}{\Delta\lambda} \tag{4.1}$$

where λ_0 is the center wavelength and $\Delta\lambda$ the FWHM of the source [114]. Thus, to get the best resolution possible, one must provide the highest bandwidth possible. Furthermore, due to water absorption and higher dispersion at long wavelengths, it was found [115] that a broad spectrum in the near-infrared around 1 μm is optimal for depth resolution. Considering these factors, GaAs/InAs QDs emitting around 1 μm are ideal candidates for high resolution OCT. These can achieve 80 nm bandwidth [116], but the output power as presented below remains pretty small (<5 mW) compared to Ti:Sapphire laser used for OCT with 20 mW output power and 176 nm FWHM [117]. Yet, a QD SLD is very compact and only requires electrical injection, contrarily to optically pumped pulsed Ti:Sapphire lasers.

The samples are four layers of InAs/GaAs QDs grown in a molecular beam epitaxy (MBE) V80 chamber by Haffouz Soufien. Height of the quantum dots on each layer was controlled by the Indium flush technique to achieve high FWHM. GaAs was used to cap

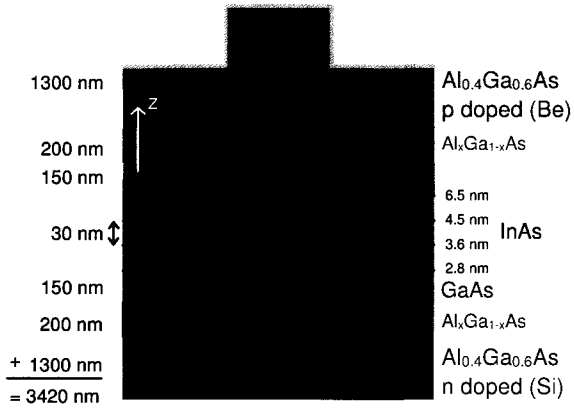

Figure 4.2: SLD structure, the $Al_xGa_{1-x}As$ is a graded barrier with x : $0 \rightarrow 0.4$. The height of QDs is controlled on purpose, from 2.8 nm to 6.5 nm.

the layers to get a 30 nm period and the layers were embedded in a waveguide of GaAs [116]. The p-n junction was formed by $Al_{0.4}Ga_{0.6}As$ barriers. More details on the sample structure are presented in figure 4.2. As mentioned in the beginning of section 3.1, we start with PL of the core QD layers to verify the bandwidth and the center wavelength of the future devices emission to save processing time.

4.2 Photoluminescence of QDs

Non-resonant PL characterization was conducted on the samples to get an insight on the emission bandwidth. Only the emission from the top of samples was collected and PL was carried at liquid nitrogen temperature to compensate for big signal attenuation due to a thick sample capping. On the left side of figure 4.3, PL of a single layer of dots shows state filling as power is increased, indicating good QD density and the possibility to achieve high FWHM by inclusion of the excited states in the emission as the device injection current is increased. However, the increase of FWHM would be limited by the limited number of states confined in the dots. On the right side, the emission bandwidth is increased from 30 nm to 125 nm in the four QD layers stack, due to modification of the QD height from layer to layer, from 2.8 nm to 6.5 nm as controlled by the GaAs first cap [116]. The constant FWHM with power increase leads to the association of the spectrum peaks with the GS transitions of each layer. Especially for SLDs, a flat profile for the emission is desired [115] and can be obtained by tuning the height of the QDs on

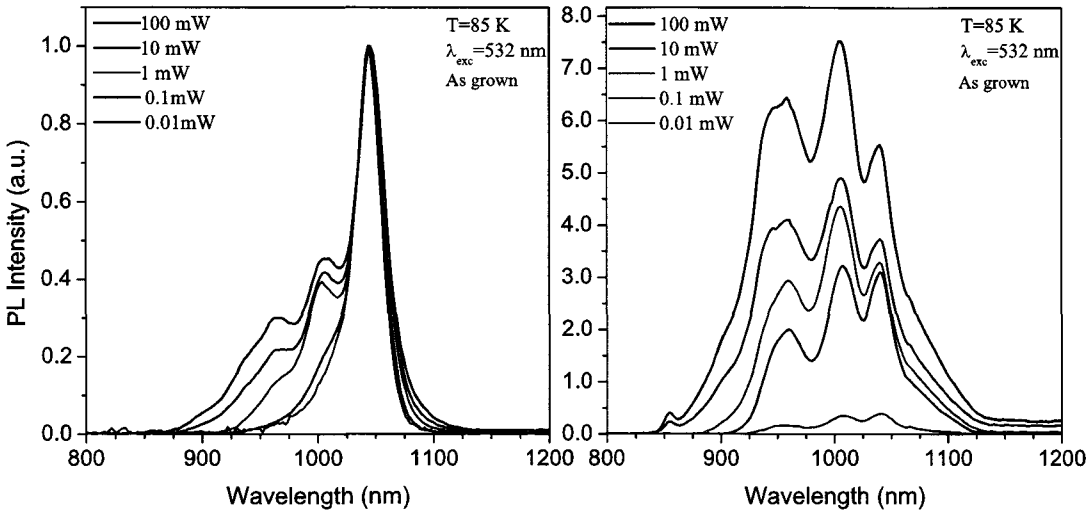

Figure 4.3: PL of InAs/GaAs QDs at liquid nitrogen temperature. Left : evidence of state filling in a single layer of QDs. Right : FWHM enhancement by the use of four QD layers

each layer in order to bring the gaussian peaks closer. The high bandwidth requirement now being achieved, so the emitting stack can be used in a SLD to measure the emitted power of the actual device.

4.3 Diode performance

Contrarily to previously introduced Fabry-Perot ridge lasers, an SLD must not provide coherent emission, so the reflectivity caused by the as-cleaved facets has to be suppressed, by the deposition of anti-reflectivity (AR) coatings. As for the telecommunications lasers, a ridge is etched on the p-side of the laser structure and to guarantee lack of lasing, the ridge was tilted with respect to device facets. Ridge tilting has already shown high power emission, without the use of AR coatings [118]. Top figure 4.4 shows the LIV curve in CW for a device with AR coatings and 8 degree tilt between the ridge and the facets. As no lasing occurs, the total emitted power is way lower than for a laser, 0.35 mW @ 500 mA. This power limitation in CW is mainly due to the thermal rollover, as revealed by the high voltage (2.5 V) and high resistivity of the sample. Furthermore, the setup being limited at 0.5 A, measurement of the maximal performance of the device is impossible.

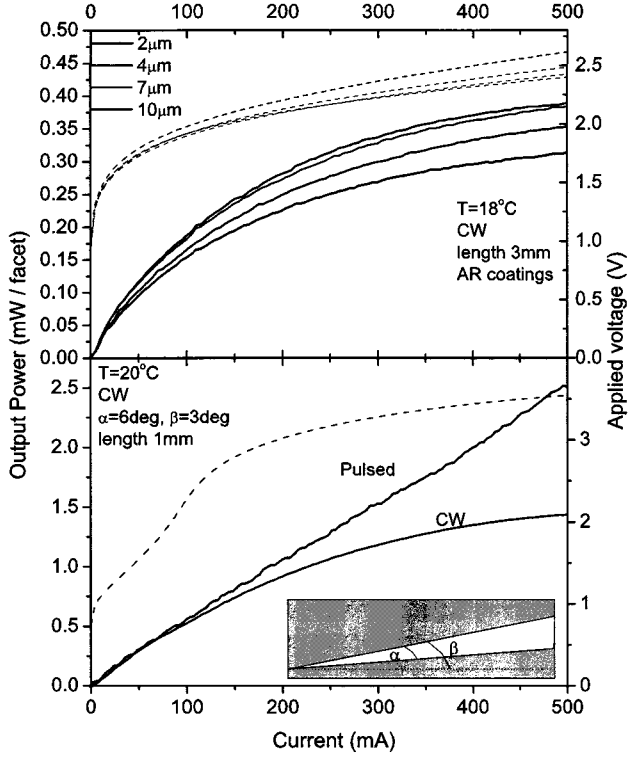

Figure 4.4: Top (Bottom) : LIV CW curve for the tilted ridge (tapered ridge). Dotted lines represent the voltage vs current for the CW measurements, duty cycle is $1\mu s$, 1%. Power emitted is enhanced by the use of a tapered ridge.

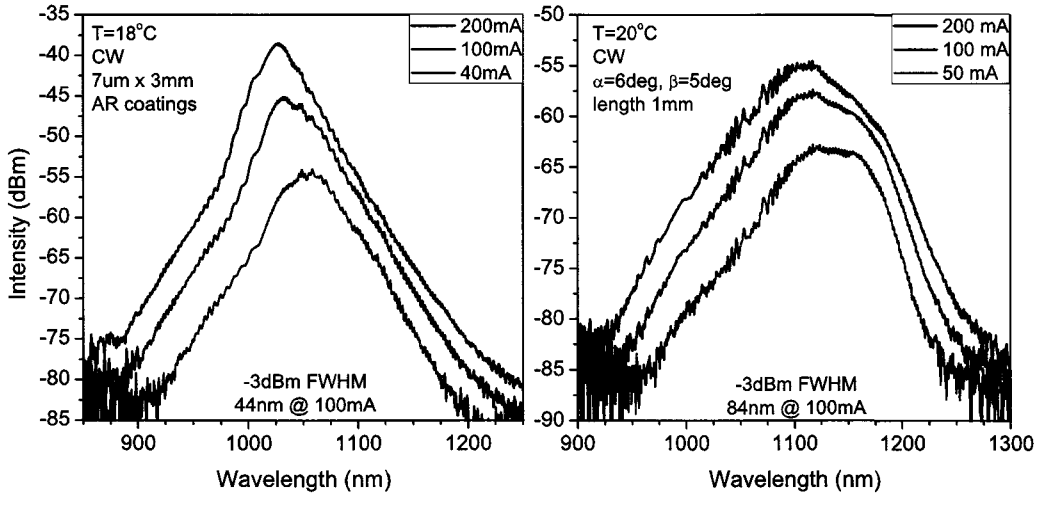

Figure 4.5: Left (Right) : EL spectrum for the tilted ridge (tapered ridge). The FWHM is increased to 84 nm with a tapered ridge.

One way to increase the output power while eliminating the AR coatings is the use of a tapered waveguide [119, 120]. By tilting the whole ridge by an angle α, the reflectivity at the facets drops and the ridge aperture angle β allows the excitation of more QDs, while reflecting the light propagating to one facet. This drastic change of ridge design resulted in fourfold increase of the output power to 1.4 mW @ 500 mA (see bottom figure 4.4). The operating voltage remains pretty high though and must be lowered by tuning the doping concentrations. To get a idea of the SLD performance without thermal effects, pulsed measurements were conducted. Results are very promising, as the emitted power reaches 2.5 mW and no sign of thermal rollover is present. Thus, we are on the way to developing a high power device, but most importantly, the center emitting wavelength must be at 1000 nm and bandwidth has to be as high as possible. Accordingly, EL characterization of the devices was carried (figure 4.5) and reveals that the bandwidth of the diode is increased from 44 nm to 84 nm @ 1100 nm by the use of a tapered ridge, as can be seen on figure 4.5. This bandwidth increase results in a lower coherence length and thus a higher depth resolution, as seen in equation 4.1.

Chapter 5

Conclusion

In this thesis, the QD advantages over other confined structures such as QWs, arising from the energy level quantization, such as higher efficiency, lower temperature dependence and higher emission bandwidth were applied to a wide range of applications. In the telecommunications, multi-wavelength lasers, mode locked lasers and SOAs are a few of the devices which performances can be improved by the use of QDs. In order to aim the development of these devices, the optical properties of InAs/InP/InGaAsP quantum dots were investigated to get insight on QD energy structure and morphology. Standard photoluminescence was conducted on QD stacks to optimize the performances of QD lasers. PL revealed that the FWHM of the emission is increased in a stack of QDs, an indication of increased inhomogeneous broadening of the dots, which reduces the peak gain of the laser. By inserting a tensile underlayer of GaP in the stack, the accumulated compressive strain in the structure was decreased, resulting in a smaller QD size distribution. This corrected the loss of peak gain by QD stacking and improved the density of dots contributing to emission. The resulting device has a 45% external efficiency, 35 mA threshold current and 50 mW maximum output power, making it a very good QW competitor. For semiconductor optical amplifiers, polarization resolved PL was needed for the long term goal of developing a polarization insensitive SOA. Normally, edge emission of QD stacks is deeply TE polarized because of the highly anisotropic cross section of QDs. As the play over the strain applied on QDs is limited because of the strain driven growth of self-assembled QDs, coupling between the QD layers was studied to amplify the TM mode contribution to achieve polarization independence. This was done by varying the dot period of a fourfold stack from 30 nm to 5 nm. It was found that

coupling between the layers combined with QD wavefunction elongation dropped the degree of polarization of the edge emission from 80% to 40% for the 5 nm period with the short axis of the dots facing emission. Pol-PL from the top of a stack of QDs grown on a miscut substrate revealed that circular dots can be grown. Combined with an increased number of closely stacked QD layers (over five), this suggests that a polarization insensitive SOA could be fabricated. As an alternative way of controlling polarization, polarization PL was done on single QDs layers thermal annealed from 625 °Cto 700 °C. However, the observed dot shape modification or composition change didn't translate into clear modification of the polarization properties. To provide a way of fine tuning the polarization properties of QD stacks, RTA on closely stacked QDs still needs to be investigated. Furthermore, the fundamental processes responsible for coupling between the dots and the modeling of the dot anisotropy, composition effect, strain on the edge polarization PL are needed for a deeper understanding of polarization properties of dots. Lastly, the inhomogeneous broadening caused by the QD stacking was used as a desirable characteristic for superluminescent diodes. These devices require high non-lasing bandwidth and high power output for optical coherence tomography in order to get high depth resolution. Standard PL was conducted on stacks of InAs/GaAs QDs where the QD height distribution throughout the layers was varied on purpose by the Indium flush technique. The PL measurements carried show bigger than 100 nm emission bandwidth and the inclusion of the stack in a tapered ridge device results in the increase from 44 nm bandwidth to 84 nm. Combined with high power output, the compact QD SLDs are a very promising alternative to conventional pulsed lasers used in medecine.

Appendix A

Additional information

A.1 PL instruments

Light sources	**Detectors**
YVO_4 @ 532 nm : • Spectra-Physics Millenia V • Maximum power : 5W He-Ne @ 632.8nm : • Melles-Griot • Maximum power : 0.01W Ti-Saph : • Spectra-Physics 3900S • Wavelength : 700-1120 nm • Maximum power : 0.5W	FTIR : • Bruker V80 • CaF2 beam splitter • Extended InGaAs detector – Operating temperature : RT – Range : 12800-4500 cm^{-1} (780-2200 nm) – Resolution : up to 0.07 cm^{-1} – Sensitivity : NEP $<$ 2 10^{-14} W $Hz^{-1/2}$ Spectrometer : • Digikröm 240 • Ge cooled photodiode • Range : 800-1800 nm • Double gratings 1200 or 600 grooves/mm

A.2 Growth sheet

	Material	Ga	In	As	P	Time	Temperature
1	InP		60		20	10min	500
					20	2min	520
					20	1min	520
2	InGaAsP	28.5	51	12.5	26.3	4min30s	520
Dot layer							
3	GaP	28.5			26.3	6s	520
4	InAs		64	40		8s	520
				40		20s	520
						5s	520
5	InGaAsP	28.5	51	12.5	26.3	8s	520
				12.5	26.3	30s	520
6	InGaAsP	28.5	51	12.5	26.3	2min24s	520
End of dot layer							
7	InGaAsP	28.5	51	12.5	26.3	2min6s	520
8	InP		51		26.3	10min	520

Table A.1: Growth sheet for core QD stack

A.3 Telecommunications lasers structures

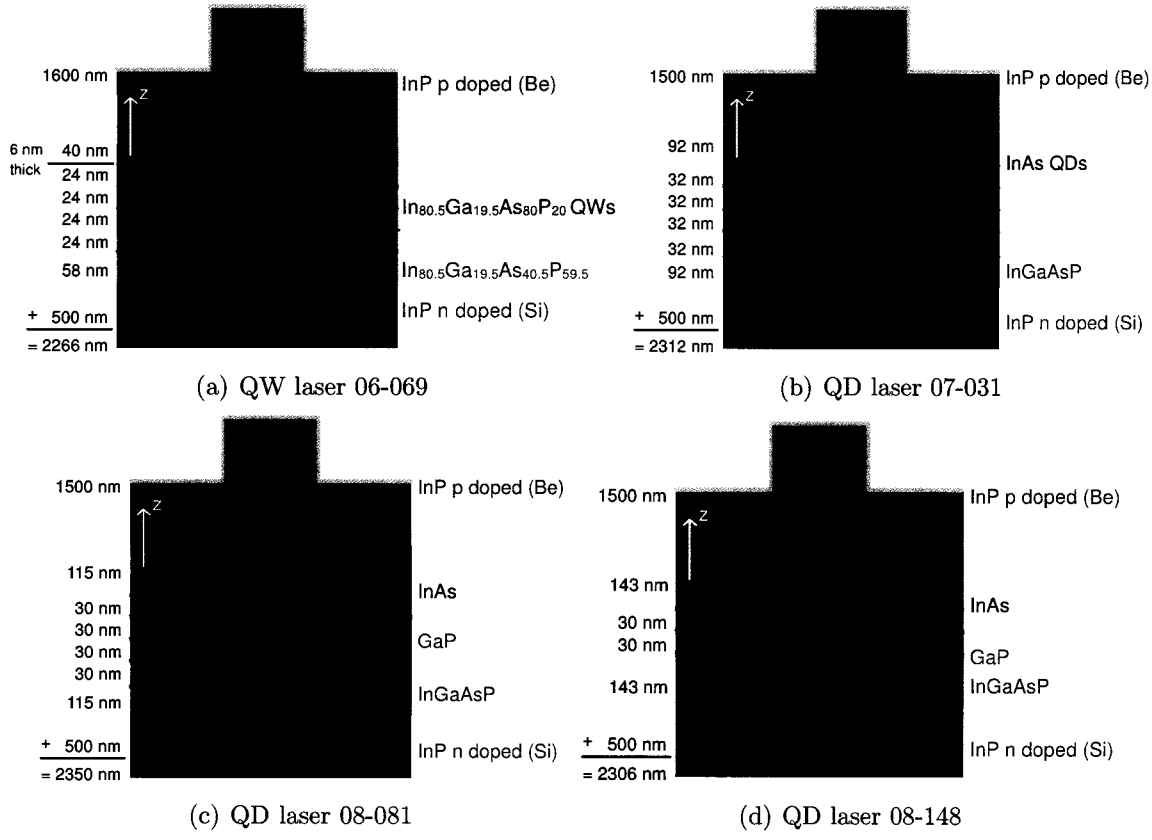

(a) QW laser 06-069

(b) QD laser 07-031

(c) QD laser 08-081

(d) QD laser 08-148

Figure A.1: Main telecommunications laser structures

Bibliography

[1] W. Shockley. The theory of p-n junction in semiconductors and p-n junction transistors. *Bell Syst. Tech. J.*, 28:435, 1949.

[2] D. M. Chapin, C. S. Fuller, and G. L. Pearson. A new silicon p-n junction photocell for converting solar radiation into electrical power. *J. Appl. Phys.*, 25(5):676–677, 1954.

[3] L. Esaki. New phenomenon in narrow germanium p-n junctions. *Phys. Rev.*, 109(2):603–604, 1958.

[4] R. N. Hall, G. E. Fenner, J. D. Kingsley, T. J. Soltys, and R. O. Carlson. Coherent light emission from GaAs junctions. *Phys. Rev. Lett.*, 9(9):366–368, 1962.

[5] H.J. Round. A note on carborundum. *Electron. World*, 19(309), 1907.

[6] J. P. van der Ziel, R. Dingle, R. C. Miller, W. Wiegmann, and Jr. W. A. Nordland. Laser oscillation from quantum states in very thin $GaAs/Al_{0.2}Ga_{0.8}As$ multilayer structures. *Appl. Phys. Lett.*, 26(8):463–465, 1975.

[7] J. M. Luttinger and W. Kohn. Motion of electrons and holes in perturbed periodic fields. *Phys. Rev.*, 97(4):869–883, 1955.

[8] E.O. Kane. Band structure of narrow gap semiconductors. *Narrow Gap Semiconductors Physics and Applications*, 133:939–941, 1980.

[9] Ania C. Bleszynski-Jayich, Linus E. Fröberg, Mikael T. Björk, H. J. Trodahl, Lars Samuelson, and R. M. Westervelt. Imaging a one-electron InAs quantum dot in an InAs/InP nanowire. *Phys. Rev. B*, 77(24):245327, 2008.

[10] V. Cerletti, W A Coish, O. Gywat, and D. Loss. Recipes for spin-based quantum computing. *Nanotechnology*, 16(4):R27–R49, 2005.

[11] M. Green and P. O'Brien. Recent advances in the preparation of semiconductors as isolated nanometric particles: New routes to quantum dots. *Chem. Commun.*, (22):2235–2241, 1999.

[12] M.A. Kastner. Artificial atoms. *Physics Today*, 46(1):24–31, 1993.

[13] Mårtensson T. and Borgström M. et al. Fabrication of individually seeded nanowire arrays by vapour-liquid-solid growth. *Nanotechnology*, 14(12):1255–1258, 2003.

[14] M. Asada, Y. Miyamoto, and Y. Suematsu. Gain and the threshold of three-dimensional quantum-box lasers. *IEEE J. Quantum Electron.*, 22(9):1915–1921, 1986.

[15] Y. Arakawa and H. Sakaki. Multidimensional quantum well laser and temperature dependence of its threshold current. *Appl. Phys. Lett.*, 40(11):939–941, 1982.

[16] K.M. Noone and D.S. Ginger. Doping for speed: Colloidal nanoparticles for thin-film optoelectronics. *ACS Nano*, 3(2):261–265, 2009.

[17] H.W. Hillhouse and M.C. Beard. Solar cells from colloidal nanocrystals: Fundamentals, materials, devices, and economics. *Curr. Opin. Colloid Interface Sci.*, 14(4):245–259, 2009.

[18] T.D. Steiner. *Semiconductor Nanostructures for Optoelectronic Applications.* Artech House Publishers, 2004.

[19] C. Nì. Allen, G. Ortner, C. Dion, P. J. Poole, P. Barrios, J. Lapointe, G. Pakulski, W. Render, S. Fafard, and S. Raymond. External-cavity quantum-dot laser tunable through 1.55 μm. *Appl. Phys. Lett.*, 88(11):113109, 2006.

[20] L. V. Asryan, S. Luryi, and R. A. Suris. Internal efficiency of semiconductor lasers with a quantum-confined active region. *IEEE J. Quantum. Electron.*, 39(3):404–418, 2003.

[21] S. Raymond, S. Studenikin, S-J Cheng, M. Pioro-Ladriere, M Ciorga, P J Poole, and M D Robertson. Families of islands in InAs/InP self-assembled quantum dots: a census obtained from magneto-photoluminescence. *Semicond. Sci. Technol.*, 18(4):385–389, 2003.

[22] S. Raymond, S. Studenikin, A. Sachrajda, Z. Wasilewski, S-J Cheng, W. Sheng, P. Hawrylak, A. Babinski, M. Potemski, G. Ortner, and M. Bayer. Excitonic energy shell structure of self-assembled InGaAs/GaAs quantum dots. *Phys. Rev. Lett.*, 92(18):187402, 2004.

[23] S. Fathpour, Z. Mi, P. Bhattacharya, A. R. Kovsh, S. S. Mikhrin, I. L. Krestnikov, A. V. Kozhukhov, and N. N. Ledentsov. The role of auger recombination in the temperature-dependent output characteristics ($t_0 = \infty$) of p-doped 1.3 μm quantum dot lasers. *Appl. Phys. Lett.*, 85(22):5164–5166, 2004.

[24] H.Y. Liu, D.T. Childs, T.J. Badcock, K.M. Groom, I.R. Sellers, M. Hopkinson, R.A. Hogg, D.J. Robbins, D.J. Mowbray, and M.S. Skolnick. High-performance three-layer $1.3\mu m$ InAs-GaAs quantum-dot lasers with very low continuous-wave room-temperature threshold currents. *IEEE Photonics Technol. Lett.*, 17(6):1139–1141, 2005.

[25] P. Hawrylak. Excitonic artificial atoms: Engineering optical properties of quantum dots. *Phys. Rev. B*, 60(8):5597–5608, 1999.

[26] D. Chithrani, R. L. Williams, J. Lefebvre, P. J. Poole, and G. C. Aers. Optical spectroscopy of single, site-selected, InAs/InP self-assembled quantum dots. *Appl. Phys. Lett.*, 84(6):978–980, 2004.

[27] M.E. Reimer, D. Dalacu, J. Lapointe, P. J. Poole, D. Kim, G. C. Aers, W. R. McKinnon, and R. L. Williams. Single electron charging in deterministically positioned InAs/InP quantum dots. *Appl. Phys. Lett.*, 94(1):011108, 2009.

[28] M. Vachon, S. Raymond, A. Babinski, J. Lapointe, Z. Wasilewski, and M. Potemski. Energy shell structure of a single InAs/GaAs quantum dot with a spin-orbit interaction. *Phys. Rev. B*, 79(16):165427, 2009.

[29] E. C. Le Ru, P. Howe, T. S. Jones, and R. Murray. Strain-engineered InAs/GaAs quantum dots for long-wavelength emission. *Phys. Rev. B*, 67(16):165303, 2003.

[30] S. Fafard, Z. Wasilewski, J. McCaffrey, S. Raymond, and S. Charbonneau. InAs self-assembled quantum dots on InP by molecular beam epitaxy. *Appl. Phys. Lett.*, 68(7):991–993, 1996.

[31] K. Kawaguchi, N. Yasuoka, M. Ekawa, H. Ebe, T. Akiyama, M. Sugawara, and Y. Arakawa. Optical properties of columnar InAs quantum dots on InP for semiconductor optical amplifiers. *Appl. Phys. Lett.*, 93(12):121908, 2008.

[32] Z.G. Lu, J.R. Liu, P.J. Poole, S. Raymond, P.J. Barrios, D. Poitras, G. Pakulski, P. Grant, and D. Roy-Guay. An l-band monolithic InAs/InP quantum dot mode-locked laser with femtosecond pulses. *Opt. Express*, 17(16):13609–13614, 2009.

[33] Z.G. Lu, J. R. Liu, S. Raymond, P. J. Poole, P. J. Barrios, and D. Poitras. 312-fs pulse generation from a passive c-band InAs/InP quantum dot mode-locked laser. *Opt. Express*, 16(14):10835–10840, 2008.

[34] L.W. Shi, Y.H. Chen, B. Xu, Z.C. Wang, Y.H. Jiao, and Z.G. Wang. Status and trends of short pulse generation using mode-locked lasers based on advanced quantum-dot active media. *J. Phys. D: Appl. Phys.*, 40(18):R307–R318, 2007.

[35] D. Zhou, R. Piron, M. Dontabactouny, O. Dehaese, F. Grillot, T. Batte, K. Tavernier, J. Even, and S. Loualiche. Low threshold current density of InAs quantum dash laser on InP (100) through optimizing double cap technique. *Appl. Phys. Lett.*, 94(8):081107, 2009.

[36] M. Korkusinski, M.E. Reimer, R.L. Williams, and P. Hawrylak. Engineering photon cascades from multiexciton complexes in a self-assembled quantum dot by a lateral electric field. *Phys. Rev. B*, 79(3):035309, 2009.

[37] M.E. Reimer, W.R. McKinnon, J. Lapointe, D. Dalacu, P.J. Poole, G.C. Aers, D. Kim, M. Korkusinski, P. Hawrylak, and R.L. Williams. Towards scalable gated quantum dots for quantum information applications. *Physica E*, 40(6):1790 – 1793, 2008. 13th International Conference on Modulated Semiconductor Structures.

[38] J. Liu, Z. Lu, S. Raymond, P.J. Poole, P.J. Barrios, G. Pakulski, D. Poitras, G. Xiao, and Z. Zhang. Uniform 90-channel multiwavelength InAs/InGaAsP quantum dot laser. *Electron. Lett.*, 43(8):458–459, 2007. cited By (since 1996) 5.

[39] D. Bimberg M. Grundmann and N. N. Ledentsov. *Quantum Dot Heterostructures.* John Wiley and Sons, Reading, Massachusetts, 1999.

[40] Z. M. Wang. *Self Assembled Quantum Dots.* Springer, 2007.

[41] M. Gong, K. Duan, C. Li, R. Magri, G.A. Narvaez, and L. He. Electronic structure of self-assembled InAs/InP quantum dots: Comparison with self-assembled InAs/GaAs quantum dots. *Phys. Rev. B*, 77(4):045326, 2008.

[42] A. Wojs, P. Hawrylak, S. Fafard, and L. Jacak. Electronic structure and magneto-optics of self-assembled quantum dots. *Phys. Rev. B*, 54(8):5604–5608, 1996.

[43] S. Raymond. *Zero-Dimensional Properties of Self-Assembled Islands.* PhD thesis, University of Ottawa, 1997.

[44] G. Bastard. *Wave Mechanics Applied to Semiconductor Heterostructures.* Editions de Physique, 1988. p. 32.

[45] P.K. Basu. *Theory of Optical Processes in Semiconductors.* Oxford University Press, 1997. p. 62.

[46] W. Sheng, S-J Cheng, and P. Hawrylak. Multiband theory of multi-exciton complexes in self-assembled quantum dots. *Phys. Rev. B*, 71(3):035316, 2005.

[47] O. Stier, M. Grundmann, and D. Bimberg. Electronic and optical properties of strained quantum dots modeled by 8-band $k \cdot p$ theory. *Phys. Rev. B*, 59(8):5688–5701, 1999.

[48] T. Saito, T. Nakaoka, T. Kakitsuka, Y. Yoshikuni, and Y. Arakawa. Strain distribution and electronic states in stacked InAs/GaAs quantum dots with dot spacing 0-6nm. *Physica E*, 26(1-4):217 – 221, 2005. International Conference on Quantum Dots.

[49] G. Bastard. *Wave Mechanics Applied to Semiconductor Heterostructures.* Editions de Physique, 1988.

[50] U. Bockelmann and G. Bastard. Interband absorption in quantum wires. i. zero-magnetic-field case. *Phys. Rev. B*, 45(4):1688–1699, 1992.

[51] P.K. Basu. *Theory of Optical Processes in Semiconductors.* Oxford University Press, 1997. p. 226.

[52] A. V. Uskov, J. McInerney, F. Adler, H. Schweizer, and M. H. Pilkuhn. Auger carrier capture kinetics in self-assembled quantum dot structures. *Appl. Phys. Lett.*, 72(1):58–60, 1998.

[53] S. Fafard, Z. R. Wasilewski, C. NÌ Allen, D. Picard, P. G. Piva, and J. P. McCaffrey. Self-assembled quantum dots: five years later. *Superlattices Microstruct.*, 25(1-2):87 – 96, 1999.

[54] S. Raymond, S. Fafard, P. J. Poole, A. Wojs, P. Hawrylak, C. Gould, S. Sachrajda, S. Charbonneau, D. Leonard, R. Leon, P. M. Petroff, and J. L. Merz. State-filling and magneto-photoluminescence of excited states in InGaAs/GaAs self-assembled quantum dots. *Superlattices and Microstructures*, 21(4):541 – 558, 1997.

[55] S. Raymond, S. Fafard, P. J. Poole, A. Wojs, P. Hawrylak, S. Charbonneau, D. Leonard, R. Leon, P. M. Petroff, and J. L. Merz. State filling and time-resolved photoluminescence of excited states in $In_xGa_{1-x}As$/GaAs self-assembled quantum dots. *Phys. Rev. B*, 54(16):11548–11554, 1996.

[56] G. Bastard. *Wave Mechanics Applied to Semiconductor Heterostructures.* Editions de Physique, 1988. p. 247.

[57] T. Takagahara. Theory of exciton doublet structures and polarization relaxation in single quantum dots. *Phys. Rev. B*, 62(24):16840–16855, 2000.

[58] W. Sheng. Polarization of intersubband transitions in self-assembled quantum dots. *Appl. Phys. Lett.*, 92(4):043113, 2008.

[59] T. Saito, H. Ebe, Y. Arakawa, T. Kakitsuka, and Mitsuru Sugawara. Optical polarization in columnar InAs/GaAs quantum dots: 8-band k · p calculations. *Phys. Rev. B*, 77(19):195318, 2008.

[60] E. Hecht. *Optics.* Addison Wesley, 2002.

[61] P.J. Poole, K. Kaminska, P. Barrios, Z. Lu, and J. Liu. Growth of InAs/InP-based quantum dots for 1.55 μm laser applications. *J. Cryst. Growth*, 311(6):1482–1486, 2009.

[62] P. J. Poole, R. L. Williams, J. Lefebvre, and S. Moisa. Using As/P exchange processes to modify InAs/InP quantum dots. *J. Cryst. Growth*, 257(1-2):89 – 96, 2003.

[63] C. Paranthoen, N. Bertru, O. Dehaese, A. Le Corre, S. Loualiche, B. Lambert, and G. Patriarche. Height dispersion control of InAs/GaAs quantum dots emitting at 1.55 μm. *Appl. Phys. Lett.*, 78(12):1751–1753, 2001.

[64] D. Kim, J. Lefebvre, J. Lapointe, M.E. Reimer, J. Mckee, P.J. Poole, and R.L Williams. Optical spectroscopy of single, planar, self-assembled InAs/InP quantum dots. volume 3, pages 3840–3843, 2006.

[65] S. Fafard and C. Nì. Allen. Intermixing in quantum-dot ensembles with sharp adjustable shells. *Appl. Phys. Lett.*, 75(16):2374–2376, 1999.

[66] S. Malik, C. Roberts, R. Murray, and M. Pate. Tuning self-assembled InAs quantum dots by rapid thermal annealing. *Appl. Phys. Lett.*, 71(14):1987–1989, 1997.

[67] T. M. Hsu, Y. S. Lan, W.-H. Chang, N. T. Yeh, and J.-I. Chyi. Tuning the energy levels of self-assembled InAs quantum dots by rapid thermal annealing. *Appl. Phys. Lett.*, 76(6):691–693, 2000.

[68] J. F. Girard, C. Dion, P. Desjardins, C. Nì Allen, P. J. Poole, and S. Raymond. Tuning of the electronic properties of self-assembled InAs/InP(001) quantum dots by rapid thermal annealing. *Appl. Phys. Lett.*, 84(17):3382–3384, 2004.

[69] P. J. Poole, J. McCaffrey, R. L. Williams, J. Lefebvre, and D. Chithrani. Chemical beam epitaxy growth of self-assembled InAs/InP quantum dots. *Papers from the 19th north american conference on molecular beam epitaxy*, 19(4):1467–1470, 2001.

[70] P. Lever, H. H. Tan, and C. Jagadish. InGaAs quantum dots grown with GaP strain compensation layers. *J. Appl. Phys.*, 95(10):5710–5714, 2004.

[71] Z. R. Wasilewski, S. Fafard, and J. P. McCaffrey. Size and shape engineering of vertically stacked self-assembled quantum dots. *J. Cryst. Growth*, 201-202:1131 – 1135, 1999.

[72] X. Huang, A. Stintz, C. P. Hains, G. T. Liu, s-J Cheng, and K. J. Malloy. Very low threshold current density room temperature continuous-wave lasing from a single-layer InAs quantum-dot laser. *IEEE Photonic. Tech. L.*, 12(3):227–229, 2000.

[73] J. H. Van Der Merwe. Crystal interfaces. part i. semi-infinite crystals. *J. Appl. Phys.*, 34(1):117–122, 1963.

[74] J. Tatebayashi, N. Nuntawong, P.S. Wong, Y-C Xin, L.F. Lester, and D L Huffaker. Strain compensation technique in self-assembled InAs/GaAs quantum dots for applications to photonic devices. *J. Phys. D: Appl. Phys.*, 42(7):073002, 2009.

[75] C. Nì Allen, P. Finnie, S. Raymond, Z. R. Wasilewski, and S. Fafard. Inhomogeneous broadening in quantum dots with ternary aluminum alloys. *Appl. Phys. Lett.*, 79(17):2701–2703, 2001.

[76] J. M. Ulloa, S. Anantathanasarn, P. J. van Veldhoven, P. M. Koenraad, and R. Nötzel. Influence of an ultrathin GaAs interlayer on the structural properties of InAs/InGaAsP/InP (001) quantum dots investigated by cross-sectional scanning tunneling microscopy. *Appl. Phys. Lett.*, 92(8):083103, 2008.

[77] A.E. Zhukov, A.R. Kovsh, S.S. Mikhrin, N.A. Maleev, V.M. Ustinov, D.A. Livshits, I.S. Tarasov, D.A. Bedarev, M.V. Maximov, A.F. Tsatsul'nikov, I.P. Soshnikov, P.S. Kop'ev, Zh.I. Alferov, N.N. Ledentsov, and D. Bimberg. 3.9 W CW power from sub-monolayer quantum dot diode laser. *Electron. Lett.*, 35(21):1845–1847, 1999.

[78] Q. Gong, R. Nötzel, P.J. Van Veldhoven, and J.H. Wolter. InAs/InP quantum dots emitting in the wavelength region by inserting ultrathin GaAs and GaP interlayers. *J. Cryst. Growth*, 278(1-4):67 – 71, 2005. 13th International Conference on Molecular Beam Epitaxy.

[79] S. Yoon, Y. Moon, T-W Lee, E. Yoon, and Y.D. Kim. Effects of As/P exchange reaction on the formation of InAs/InP quantum dots. *Appl. Phys. Lett.*, 74(14):2029–2031, 1999.

[80] A. Mathur and P.D. Dapkus. Polarization insensitive strained quantum well gain medium for lasers and optical amplifiers. *Appl. Phys. Lett.*, 61(24):2845–2847, 1992.

[81] F. Seiferth, F.G. Johnson, S.A. Merritt, S. Fox, R.D. Whaley, Y.J. Chen, M. Dagenais, and D.R. Stone. Polarization insensitive 1.55-μm optical amplifier with GaAs delta-strained $Ga_{0.47}In_{0.53}As$ quantum wells. *IEEE Photonics Technol. Lett.*, 9(10):1340–1342, 1997.

[82] M. Joma, H. Horikawa, C. Q. Xu, K. Yamada, Y. Katoh, and T. Kamijoh. Polarization insensitive semiconductor laser amplifiers with tensile strained InGaAsP/InGaAsP multiple quantum well structure. *Appl. Phys. Lett.*, 62(2):121–122, 1993.

[83] H. Saito, K. Nishi, I. Ogura, S. Sugou, and Yoshimasa Sugimoto. Room-temperature lasing operation of a quantum-dot vertical-cavity surface-emitting laser. *Appl. Phys. Lett.*, 69(21):3140–3142, 1996.

[84] J. M. Lamy, C. Paranthoen, C. Levallois, A. Nakkar, H. Folliot, J. P. Gauthier, O. Dehaese, A. Le Corre, and S. Loualiche. Polarization control of 1.6 μm vertical-cavity surface-emitting lasers using InAs quantum dashes on InP(001). *Appl. Phys. Lett.*, 95(1):011117, 2009.

[85] P. Jayavel, H. Tanaka, T. Kita, O. Wada, H. Ebe, M. Sugawara, J. Tatebayashi, Y. Arakawa, Y. Nakata, and T. Akiyama. Control of optical polarization anisotropy in edge emitting luminescence of InAs/GaAs self-assembled quantum dots. *Appl. Phys. Lett.*, 84(11):1820–1822, 2004.

[86] P. Yu, W. Langbein, K. Leosson, J. M. Hvam, N. N. Ledentsov, D. Bimberg, V. M. Ustinov, A. Yu. Egorov, A. E. Zhukov, A. F. Tsatsul'nikov, and Yu. G. Musikhin. Optical anisotropy in vertically coupled quantum dots. *Phys. Rev. B*, 60(24):16680–16685, 1999.

[87] S. Anantathanasarn, P. J. van Veldhoven, T. J. Eijkemans, T. de Vries, E. Smalbrugge, E. J. Geluk, E. A. J. M. Bente, Y. S. Oei, M. K. Smit, and R. Nötzel. Polarization control of gain of stacked InAs/InP (100) quantum dots at 1.55 μm: Interplay between ground and excited state transitions. *Appl. Phys. Lett.*, 92(12):123113, 2008.

[88] W. Sheng. Origins of optical anisotropy in artificial atoms. *Appl. Phys. Lett.*, 89(17):173129, 2006.

[89] Y. M. Manz, A. Christ, O. G. Schmidt, T. Riedl, and A. Hangleiter. Optical and structural anisotropy of InP/GaInP quantum dots for laser applications. *Appl. Phys. Lett.*, 83(5):887–889, 2003.

[90] V.P. Evtikhiev, V.E. Tokranov, A.K. Kryzhanovskii, A.M. Boiko, R.A. Suris, A.N. Titkov, A. Nakamura, and M. Ichida. Growth of InAs quantum dots on vicinal GaAs(001) surfaces misoriented in the [010]. *Semiconductors*, 32(7):765–769, 1998.

[91] V.P. Evtikhiev, A.M. Boiko, I.V. Kudryashov, A.K. Kryganovskii, R.A. Suris, A.N. Titkov, and V.E. Tokranov. Control of density, size and size uniformity of mbe-grown InAs quantum dots by means of substrate misorientation. *Semicond. Sci. Technol.*, 17(6):545–550, 2002.

[92] M. C. Y. Chan and E. Herbert Li. The effects of interdiffusion on the polarization insensitivity in a tensile-strained barrier GaAs/GaAsP quantum well. *Physica E*, 8(2):184 – 188, 2000.

[93] W.C.H. Choy, E.H. Li, and J. Micallef. Polarization-insensitive electroabsorptive modulation using interdiffused InGaAs(P)-InP quantum wells. *IEEE J. Quantum Electron.*, 33(8):1316–1322, 1997.

[94] N. Y. Jin-Phillipp, K. Du, F. Phillipp, M. Zundel, and K. Eberl. Thermal stability of stacked self-assembled InP quantum dots in GaInP. *J. Appl. Phys.*, 91(5):3255–3260, 2002.

[95] L. A. Coldren and S.W. Corzine. *Diode Lasers and Photonic Integrated Circuits.* Whiley-InterScience, 1995.

[96] K. S. Mobarhan. *Test and Characterization of Laser Diodes: Determination of Principal Parameters.* Newport Corporation, 1999.

[97] A. Yu. Egorov N. A. Maleev V. M. Ustinov, A. E. Zhukov. *Quantum dot lasers.* Oxford University Press, 2003. p. 113.

[98] Y. P. Varshni. Temperature dependence of the energy gap in semiconductors. *Physica*, 34(1):149 – 154, 1967.

[99] L.V. Asryan and R.A. Suris. Temperature dependence of the threshold current density of a quantum dot laser. *IEEE J. Quantum Electron.*, 34(5):841–850, 1998.

[100] P.N. Brunkov, S.G. Konnikov, V.M. Ustinov, A.E. Zhukov, A.Yu. Egorov, M.V. Maksimov, N.N. Ledentsov, and P.S. Kop'ev. Capacitance spectroscopy of electron energy levels in InAs quantum dots in a GaAs matrix. *Semiconductors*, 30(5):492–496, 1996.

[101] D. Bimberg and N. Ledentsov. Quantum dots: lasers and amplifiers. *J. Phys.: Condens. Matter*, 15(24):R1063–R1076, 2003.

[102] C. Nì. Allen, P. J. Poole, P. Marshall, J. Fraser, S. Raymond, and S. Fafard. InAs self-assembled quantum-dot lasers grown on (100) InP. *Appl. Phys. Lett.*, 80(19):3629–3631, 2002.

[103] M. Rattunde, J. Schmitz, R. Kiefer, and J. Wagner. Comprehensive analysis of the internal losses in 2.0 μm(AlGaIn)(AsSb) quantum-well diode lasers. *Appl. Phys. Lett.*, 84(23):4750–4752, 2004.

[104] J. Piprek, P. Abraham, and J.E. Bowers. Cavity length effects on internal loss and quantum efficiency of multiquantum-well lasers. *IEEE J. Sel. Top. Quantum Electron.*, 5(3):643–647, 1999.

[105] D. Garbuzov, L. Xu, S.R. Forrest, R. Menna, R. Martinelli, and J.C. Connolly. 1.5 μm wavelength, SCH-MQW InGaAsP/InP broadened-waveguide laser diodes with low internal loss and high output power. *Electron. Lett.*, 32(18):1717–, 1996.

[106] L.V. Asryan and S. Luryi. Tunneling-injection quantum-dot laser: ultrahigh temperature stability. *IEEE J. Quantum Electron.*, 37(7):905–910, 2001.

[107] H.C. Sun, L. Davis, S. Sethi, J. Singh, and P. Bhattacharya. Properties of a tunneling injection quantum-well laser: Recipe for 'cold' device with a large modulation bandwidth. *IEEE Photonics Technol. Lett.*, 5(8):870–872, 1993.

[108] S. Pradhan, S. Ghosh, and R. Bhattacharya. Temperature dependent steady-state characteristics of high-performance tunnel injection quantum dot lasers. *Electron. Lett.*, 38(23):1449–1450, 2002.

[109] K. Nishi, H. Saito, S. Sugou, and J.S. Lee. A narrow photoluminescence linewidth of 21 mev at 1.35 μm from strain-reduced InAs quantum dots covered by $In_{0.2}Ga_{0.8}As$ grown on GaAs substrates. *Appl. Phys. Lett.*, 74(8):1111–1113, 1999.

[110] G. Liu, A. Stintz, H. Li, K.J. Malloy, and L.F. Lester. Extremely low room-temperature threshold current density diode lasers using InAs dots in $In_{0.15}Ga_{0.85}As$ quantum well. *Electron. Lett.*, 35(14):1163–1165, 1999.

[111] R.H. Wang, A. Stintz, P.M. Varangis, T.C. Newell, H. Li, K.J. Malloy, and L.F. Lester. Room-temperature operation of InAs quantum-dash lasers on InP (001). *IEEE Photonics Technol. Lett.*, 13(8):767–769, 2001.

[112] A. F. Fercher, W. Drexler, C. K. Hitzenberger, and T. Lasser. Optical coherence tomography - principles and applications. *Rep. Prog. Phys.*, 66(2):239–303, 2003.

[113] E. Bouma Brett and J. Tearney Guillermo. *Handbook of optical coherence tomography.* Informa Health Care, 2002.

[114] P. H. Tomlins and R. K. Wang. Theory, developments and applications of optical coherence tomography. *J. Phys. D: Appl. Phys.*, 38(15):2519–2535, 2005.

[115] Y. Wang, J. Nelson, Z. Chen, B. Reiser, R. Chuck, and R. Windeler. Optimal wavelength for ultrahigh-resolution optical coherence tomography. *Opt. Express*, 11(12):1411–1417, 2003.

[116] S. Haffouz, S. Raymond, Z.G. Lu, P.J. Barrios, D. Roy-Guay, X. Wu, J.R. Liu, D. Poitras, and Z.R. Wasilewski. Growth and fabrication of quantum dots superluminescent diodes using the indium-flush technique: A new approach in controlling the bandwidth. *J. Cryst. Growth*, 311(7):1803 – 1806, 2009. International Conference on Molecular Beam Epitaxy (MBE-XV), The 15th International Conference on Molecular Beam Epitaxy (MBE-XV).

[117] A. Unterhuber, B. Považay, B. Hermann, H. Sattmann, W. Drexler, V. Yakovlev, G. Tempea, C. Schubert, E. M. Anger, P. K. Ahnelt, M. Stur, J. E. Morgan, A. Cowey, G. Jung, T. Le, and A. Stingl. Compact, low-cost Ti:Al_2O_3 laser for in

vivo ultrahigh-resolution optical coherence tomography. *Opt. Lett.*, 28(11):905–907, 2003.

[118] Z.Y. Zhang, Z.G. Wang, B. Xu, P. Jin, Z.Z. Sun, and F.Q. Liu. High-performance quantum-dot superluminescent diodes. *IEEE Photonics Technol. Lett.*, 16(1):27–29, 2004.

[119] I. Middlemast, J. Sarma, and S. Yunus. High power tapered superluminescent diodes using novel etched deflectors. *Electron. Lett.*, 33(10):903–904, 1997.

[120] G.A. Alphonse, D.B. Gilbert, M.G. Harvey, and M. Ettenberg. High-power superluminescent diodes. *IEEE J. Quantum Electron.*, 24(12):2454–2457, 1988.